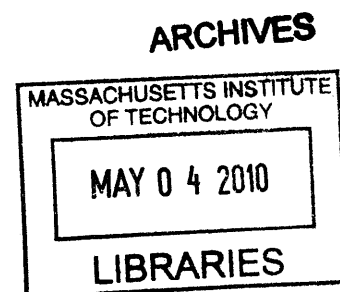


# A Novel Nanoscale Delivery System for Spatio-Temporal Delivery of Combination Chemotherapy

By

David A. Eavarone

S.M. Bioengineering  
Massachusetts Institute of Technology, 2004  
B.S. Biomedical Engineering  
Case Western Reserve University, 2000



SUBMITTED TO THE DEPARTMENT OF HEALTH SCIENCES AND TECHNOLOGY IN  
PARTIAL FULFILLMENT OF THE REQUIREMENTS FOR THE DEGREE OF  
DOCTOR OF PHILOSOPHY IN BIOMEDICAL ENGINEERING

AT THE

MASSACHUSETTS INSTITUTE OF TECHNOLOGY

JUNE 2009

©2009 Massachusetts Institute of Technology

The author hereby grants to MIT permission to reproduce and to distribute publicly paper and  
electronic copies of this thesis document in whole or in part in any medium now known or  
hereafter created.

Signature of Author: \_\_\_\_\_

Department of Health Sciences and Technology  
April 29<sup>th</sup>, 2009

Certified by: \_\_\_\_\_

Ram Sasisekharan, Ph.D.  
Director, Harvard-MIT Division of Health Sciences and Technology / Edward Hood Taplin  
Professor of Health Sciences & Technology and Biological Engineering, Thesis Supervisor

Accepted by: \_\_\_\_\_

Ram Sasisekharan, Ph.D.  
Director, Harvard-MIT Division of Health Sciences and Technology / Edward Hood Taplin  
Professor of Health Sciences & Technology and Biological Engineering



This thesis has been examined by a committee of the Health Sciences and Technology Department as follows:

Professor Elazer Edelman, M.D., Ph.D. \_\_\_\_\_  
Thomas D. and Virginia W. Cabot Professor of Health Sciences and Technology  
Thesis Committee Chairman

Professor Ram Sasisekharan, Ph.D. \_\_\_\_\_  
Director, Harvard-MIT Division of Health Sciences and Technology / Edward Hood Taplin  
Professor of Health Sciences & Technology and Biological Engineering  
Thesis Supervisor

Professor Robert S. Langer, Jr., Sc.D. \_\_\_\_\_  
Institute Professor, MIT



# A Novel Nanoscale Delivery System for Spatio-Temporal Delivery of Combination Chemotherapy

By

David A. Eavarone

SUBMITTED TO THE DEPARTMENT OF HEALTH SCIENCES AND TECHNOLOGY IN PARTIAL FULFILLMENT OF THE REQUIREMENTS FOR THE DEGREE OF DOCTOR OF PHILOSOPHY IN BIOMEDICAL ENGINEERING

## ABSTRACT

In the continuing search for effective treatments for cancer, the emerging model is the combination of traditional chemotherapy with anti-angiogenesis agents that inhibit blood vessel growth. However, the implementation of this strategy has faced two major obstacles. First, the long-term shutdown of tumor blood vessels by the anti-angiogenesis agent can prevent the tumor from receiving a therapeutic concentration of the chemotherapy agent. Second, inhibiting blood supply drives the formation of intra-tumoral hypoxia, or a lack of oxygen, which has been correlated with increased tumor invasiveness and resistance to chemotherapy.

In this thesis we report the disease-driven engineering of a drug delivery system, a 'nanocell', which overcomes these barriers unique to solid tumors. The nanocell comprises a nuclear nanoparticle encapsulated within a lipid membrane and is preferentially taken up by the tumor. The nanocell delivers a temporal release of two drugs within the tumor core: the outer lipid envelope first releases an anti-angiogenesis agent, causing a vascular shutdown; the inner nanoparticle, which is trapped inside the tumor, then releases a chemotherapy agent. This focal release within the tumor targets cells most at risk for hypoxia and results in improved therapeutic index with reduced toxicity. The technology can be extended to additional agents, so as to target multiple signaling pathways or distinct tumor compartments, enabling the model of an 'integrative' approach in cancer therapy.

In the second part of the thesis we report new tools for the optimization of nanocell formulations. We present a new, three-dimensional, voxel-based computational model for Monte Carlo simulations of nanoparticle delivery systems that enables direct investigation of the entire vehicle during particle degradation and drug release. Use of this model in combination with emerging mechanistic understandings of nanoparticle drug release will facilitate optimization of nanocell combination therapy release profiles. We additionally report the generation and characterization of a set of carbohydrate-based chemotherapeutic agents that have the potential for use in nanocells as reduced toxicity alternatives to traditional chemotherapy agents.

Thesis Supervisor: Ram Sasisekharan, Ph.D., Director, Harvard-MIT Division of Health Sciences and Technology / Edward Hood Taplin Professor of Health Sciences & Technology and Biological Engineering



## **Acknowledgements**

I would first and foremost like to express my gratitude to my advisor Ram Sasisekharan who has been an outstanding mentor throughout my thesis research. He has a skill for motivating his students to seek out the big problems and then inspiring in them the courage to believe they can help solve them. I also owe many thanks to my committee chair Elazer Edelman and committee member Robert Langer for their guidance and support in developing and focusing my work into the story presented here. I would also like to thank the Whitaker Foundation and the Toxicology Training Grant for my funding during the course of this thesis.

This research could not have succeeded without the assistance of so many of my colleagues and collaborators who gave generously of both their time and expertise. I would particularly like to thank Shiladitya Sengupta, Toomas Haller, Ishan Capila, Ganlin Zhao, Luke Robinson, Ido Bachelet, Venkataramanan Soundararajan, Tanyel Kiziltipe, Karunya Srinivasan, Nikki Watson, Aarthi Chandrasekaran, Pochi Shum, Giovanni Franzesi, Sujan Kabir, James Myette, and Kris Holley. While I could not list them all, I would also like to express my sincere gratitude to the many other members of the Sasisekharan lab both past and present who have contributed so much to my professional and personal growth. I also would like to thank the lab administrator Ada Ziolkowski for her extensive assistance with the many facets of being a graduate student throughout my time here.

I would especially like to thank my family, my parents Daniel and Diane and my brother Brian, for their unwavering support and for all I have learned from them throughout my life. I truly am where I am today because of them. Finally, I owe a tremendous debt of gratitude to my wife Lisa; the success of this thesis would never have been possible without all of her support and understanding.





## Table of Contents

|  |           |
|--|-----------|
| <b>Abstract.....</b>   | <b>5</b>  |
| <b>Acknowledgements.....</b>   | <b>6</b>  |
| <b>Table of Contents.....</b>  | <b>9</b>  |
| <b>1. Background.....</b>  | <b>11</b> |
| 1.1. Motivation.....   | 11        |
| 1.2. New Paradigm of Spatio-Temporal Delivery.....                                       | 16        |
| 1.2.1. The Nanocell.....   | 19        |
| 1.2.2. New Mechanistic Understandings of Nanoscale Drug Delivery.....                    | 20        |
| 1.2.3. Development of Reduced-toxicity Antitumor Agents.....                             | 22        |
| 1.3. References.....   | 24        |
| <b>2. Novel Nanoscale Delivery System for Combination Chemotherapy.....</b>              | <b>31</b> |
| 2.1. Spatio-Temporal Targeting of Tumor Cells and Neovasculature: The Nanocell.....      | 33        |
| 2.1.1. Introduction.....   | 33        |
| 2.1.2. Materials and Methods.....  | 34        |
| 2.1.3. Results and Discussion.....   | 38        |
| 2.1.4. Conclusion.....   | 48        |
| 2.1.5. References.....   | 60        |
| 2.2. Lipid-Encapsulated Quantum Dots Distinguish Tumor and Normal Vasculature.....       | 63        |
| 2.2.1. Introduction.....   | 63        |
| 2.2.2. Materials and Methods.....  | 64        |
| 2.2.3. Results and Discussion.....   | 65        |
| 2.2.4. Conclusion.....   | 67        |
| 2.2.5. References.....   | 72        |
| 2.3. A Voxel-Based Monte Carlo Model of Drug Release from Bulk Eroding Nanoparticles     |           |
| 2.3.1. Introduction.....   | 74        |
| 2.3.2. Results and Discussion.....   | 76        |
| 2.3.3. Conclusion.....   | 78        |
| 2.3.4. References.....   | 84        |
| 2.4. Structure-function Relationships of Novel Carbohydrate-Based Therapeutic Agents.... | 87        |
| 2.4.1. Introduction.....   | 87        |
| 2.4.2. Materials and Methods.....  | 89        |
| 2.4.3. Results and Discussion.....   | 94        |
| 2.4.4. Conclusion.....   | 101       |
| 2.4.5. References.....   | 102       |

**3. Conclusions and Future Directions.....105**  
3.1. Conclusions.....105  
3.2. Future Directions.....107  
    3.2.1. Extending the nanocell platform.....107  
    3.2.2. Extending structure-function analysis of carbohydrate-based therapies...110  
3.3. References.....115

**List of Figures and Tables.....118**

**List of Abbreviations.....120**

## **1.1. Background**

### **1.1.1. Motivation**

New therapies for cancer that initially show promise in animal models and early clinical trials are often a disappointment over the long term when drug resistance develops and the final outcome is not a success. Until recently, drug resistance has been defined almost exclusively in terms of cellular mechanisms through which tumor cells are resistant to treatment. Recent findings have shown that the tumor microenvironment may also contribute to drug resistance through non-cellular mechanisms<sup>1</sup>. One such mechanism results from the formation of isolated regions of hypoxia due to the heterogeneous vascularization of solid tumor<sup>1</sup>. Not only are hypoxic cells in these regions less accessible to blood-borne chemotherapeutic agents, these hypoxic cells also release factors responsible for the promotion of tumor growth, angiogenesis, and metastasis<sup>2, 3</sup>. Of particular concern for combination chemotherapy is the potential for increased microenvironment mediated drug resistance after treatment with anti-angiogenic agents.

The term angiogenesis describes the formation of new capillaries from existing vasculature (for review see<sup>4</sup>). While the adult vasculature is primarily quiescent, angiogenesis occurs physiologically during embryonic development, wound healing, and the menstrual cycle. Angiogenesis is also implicated in certain pathological conditions including cancer. As a tumor undergoes rapid growth, existing vasculature is co-opted to ensure that cells maintain an adequate nutrient supply and are able to efficiently remove waste<sup>5, 6</sup>. Vascular cooption is confined to the tumor periphery and gradual tumor expansion causes a progressive central hypoxia. In order for these hypoxic cells to survive they must switch to an angiogenic phenotype<sup>7, 8</sup>. Some tumor clones remain dormant for many months and are thus confined within

several millimeters in diameter until they activate an angiogenic pathway<sup>9</sup>. Hypoxia, through hypoxia inducible factor- $\alpha$ , induces the expression of pro-angiogenic factors and may result in an angiogenic phenotype if proangiogenic factors are in excess of antiangiogenic factors<sup>10</sup>. The balance between proangiogenic and antiangiogenic conditions is affected by a variety of factors including metabolic and mechanical stresses, hypoxia, and genetic mutations<sup>11</sup>.

Once initiated, tumor angiogenesis is characterized by a regulated series of sequential steps (for review see<sup>11</sup>). Angiogenic factors produced by tumor cells bind to endothelial cell receptors and initiate angiogenesis. Matrix metalloproteinases (MMPs), released by activated endothelial cells, degrade the basement membrane and extracellular matrix (ECM) surrounding already existing capillaries near the tumor site. The break-up of ECM releases additional pro-angiogenic factors further enabling the switch to an angiogenic phenotype<sup>12</sup>. Pro-angiogenic stimuli cause endothelial cell junctions to become altered with newly formed cell projections growing towards the source of the stimulus. Endothelial cells then migrate into the tumor ECM and proliferate. There, newly formed endothelial cells organize into hollow tubes in a process called canalization. The fusing of these newly formed vascular tubes with the creation of new basement membrane enables blood flow within the tumor.

The vascular density of tumors is highly heterogeneous, and tumor blood vessels exhibit many abnormalities when compared to normal vessels including a high percentage of proliferating endothelial cells, an increased tortuosity, and aberrant basement membrane formation<sup>13, 14</sup>. As a result, tumor blood vessels exhibit marked extravasation or vessel wall hyperpermeability. Molecular transport across tumor vessels may occur via a number of pathways including interendothelial junctions and transendothelial channels, vesicular vacuole

organelles, and fenestrations<sup>15</sup>. The pore cutoff size of the tumor vasculature varies depending upon tumor model, however it is most commonly reported to range between 400 and 800nm<sup>15, 16</sup>.

The first convincing evidence that tumor growth may be angiogenesis dependent came in 1968 with an experiment demonstrating that implanted tumor tissue in non-vascularized rabbit cornea did not grow until newly formed vessels from the limbus reached the implant<sup>17</sup>. Since then, a large body of work has gone into uncovering the factors responsible for promoting tumor angiogenesis as potential targets for new therapy. Such factors currently include vascular endothelial growth factor (VEGF), basic fibroblast growth factor (bFGF), platelet-derived endothelial growth factor (PDGF), fibronectin, scatter factor (SF), and others (for review see<sup>18</sup>). Currently explored anti-angiogenic agents are of at least three classes: agents that are directly cytotoxic or static against endothelial cells, agents that inhibit growth factor release, and agents that block growth factor signaling (for review see<sup>19</sup>).

Several angiogenic inhibitors are currently under study in Phase I, II, and III clinical trials (see <http://www.cancer.gov/clinicaltrials> for current trials). Contrary to a promising body of successful work using anti-angiogenics in animal tumor models, the best outcomes from these clinical studies have been, with few exceptions, stabilization of tumor growth over a defined period<sup>20</sup>. An explanation for these relatively disappointing findings has been offered on several rationales<sup>20</sup>. Most animal studies on which the success of anti-angiogenics are based are performed with ectopically growing subcutaneously implanted tumors. Due to the relative sparseness of vasculature within the subcutis, tumors in these studies are then expected to be more dependent on new vessel formation than tumors that grow orthotopically<sup>21</sup>. Also, tumor cells used in animal studies are highly selected compared to the heterogeneous mixture of cells found in patients. Tumor cells expressing specific genetic markers have demonstrated marked

susceptibility or resistance to anti-angiogenic treatments<sup>22</sup>. Further difficulty in analyzing the effect of anti-angiogenics comes from finding clinical parameters for measuring their success<sup>23</sup>. With current cytotoxic therapies, tumor reduction is the major parameter for measuring treatment success. With anti-angiogenics, however, the lack of tumor regression may not always indicate a failure, as the mechanism of action of anti-angiogenics is often cytostatic in nature<sup>19</sup>.

While there is compelling experimental evidence that at least certain types of tumors are angiogenesis dependent, recent clinical trials have demonstrated that purely anti-angiogenic treatments are not as effective for achieving tumor regression as was originally hoped. The growing consensus is towards combination therapy<sup>7, 19, 20</sup>, using anti-angiogenics as well as traditional chemotherapy for a synergistic effect. This, however, has been more difficult than was originally anticipated. While combination therapy has been shown in many cases to be beneficial<sup>24, 25</sup>, recent evidence has demonstrated that interactions between anti-angiogenic and cytotoxic agents may in fact be antagonistic in certain tumor models. Anti-angiogenics, by cutting off the tumor blood supply, may in turn induce new regions of tumor hypoxia<sup>3, 26</sup>. Tumor hypoxia not only contributes to the induction of angiogenesis through the release of hypoxia inducible factor- $\alpha$ , but it also has been correlated with an increase in tumor invasion and metastasis<sup>3</sup>. Of particular concern is the effect of hypoxia on the efficacy of traditional chemotherapeutic agents. While it can be expected that reduced blood flow within the tumor will reduce the access of an intravenously administered drug, hypoxia has also been shown to contribute directly to cytotoxic drug resistance over a range of tumor models<sup>27</sup>. While this resistance is likely due in part to reduced cell proliferation within hypoxia regions of tumor<sup>27</sup>, upregulation of hypoxia inducible factor- $\alpha$  has also been correlated with the upregulation of the anti-apoptotic protein Bcl-2 and the multi-drug resistance product P-glycoprotein<sup>28, 29</sup>.

Nanoscience has been described as one of the most important research and development frontiers in modern science<sup>30</sup>. Nanoscale particles have found use in medicine as vehicles for DNA transfection, enzyme encapsulation, biosensors, and drug delivery<sup>30</sup>. The use of these particles in drug delivery has offered considerable promise for the enhanced delivery of chemotherapeutic agents. Encapsulation within or binding to small colloidal particles enables drugs in many cases to circulate longer, accumulate preferentially within tumor tissue, have reduced systemic toxicity, undergo controlled release, and even bypass certain cellular mechanisms of drug resistance (for review see<sup>31</sup>). Our primary goal in this work is to combine leading nanoscience technology with new understandings of tumor pathophysiology, angiogenesis, and micro-environment mediated drug resistance to develop novel strategies for treatment that improve drug efficacy, reduce toxicity, and limit certain types of drug resistance to increase chances for therapeutic success over the long-term.

## **1.2. Introduction: New Paradigm of Spatio-Temporal Drug Delivery**

In light of the motivation described above, the specific objectives of this thesis are as follows:

1. To exploit the pathophysiology of solid tumors and enhance combination chemotherapy regimens by engineering novel nanoscale delivery vehicles termed ‘nanocells.’ (Chapter 2.1 and 2.2)
  - a. To assess the therapeutic benefit of this delivery platform.
  - b. To demonstrate that any increased therapeutic benefit is due to both the controlled spatial and temporal release of the encapsulated agents, as indicated by the tumor pathophysiology.
2. To develop new tools and strategies for optimizing nanocell formulations. (Chapter 2.3 and 2.4)
  - a. To develop a new computational model for drug release from nanoscale delivery systems. A better understanding of nanoscale drug release will facilitate the future optimization of nanocell spatio-temporal release profiles.
  - b. To generate and characterize a new set of carbohydrate-based anti-tumor agents with low systemic toxicity. Anti-tumor carbohydrates may be used in nanocells as reduced toxicity alternatives to traditional chemotherapeutic agents.

The thesis is written such that Chapter 1 presents an outline of the motivation for the entire body of work as well as an introduction to how each of the thesis objectives will be met. Chapter 2.1 presents the nanocell which is a nanoscale drug delivery vehicle for the controlled



spatio-temporal delivery of multiple anti-tumor agents. The nanocell comprises a nuclear polymeric nanoparticle encapsulated within a lipid envelope, and the entire vehicle is preferentially taken up by the tumor. The nanocell enables a temporal release of two drugs: the outer envelope first releases an anti-angiogenesis agent, causing a vascular shutdown; the inner nanoparticle, which is trapped inside the tumor, then releases a chemotherapy agent. This focal release within a tumor results in improved therapeutic index with reduced toxicity. The technology can be extended to additional agents, so as to target multiple signaling pathways or distinct tumor compartments, enabling the model of an 'integrative' approach in cancer therapy.

Chapter 2.2 presents a modified nanoscale delivery vehicle for imaging angiogenesis. As tumors undergo rapid growth, they must generate their own vascular network in order to provide the nutrients necessary for continued expansion and spread. In vivo imaging of tumor vascularization is now of paramount importance, as this is both a sign of increasing tumor malignancy and a potential target for new therapies. We demonstrate here a method for imaging and specifically identifying tumor-specific vasculature using quantum dots encapsulated within nanoscale lipid membranes, combining the fluorescent properties of quantum dots with the bioavailability and tumor-specific interstitial uptake of the lipid vehicle.

Chapter 2.3 presents a new computational model for drug release from nanoscale delivery vehicles. The use of polymeric nanoparticles as drug delivery devices is becoming increasingly prevalent in a variety of therapeutic applications. Despite their widespread clinical use, the factors influencing the release profiles of nanoparticle-encapsulated drugs are still not quantitatively understood. We present here a new, semi-empirical model of drug release from polymeric nanoparticles using a formulation of dexamethasone encapsulated within poly(lactic-co-glycolic acid) PLGA to set model parameters. We introduce a three-dimensional voxel-based

framework for Monte Carlo simulations that enables direct investigation of the entire spherical nanoparticle during particle degradation and drug release. Due to implementation of this model at the nanoscale, we utilize assumptions that simplify the model while still allowing multi-phase drug release to be simulated with good correlation to experimental results.

Chapter 2.4 presents the generation and characterization of new anti-tumor carbohydrate based agents. We demonstrate here an integrative approach for the standardization and structure-function analysis of a new class of anti-tumor modified pectins classified here as activated citrus pectin (ACP) generated from native citrus pectin (NCP) which is isolated directly from lemon. We incorporate complementary analytical techniques to link ACP structure with binding to tumor galectin targets. We further provide evidence for a mechanism of action by elucidating key constituents of an ACP-induced anti-tumor intracellular signaling cascade. A better understanding of ACP anti-tumor activity as it relates to its structural modification will allow the synthesis of more effective and more reliable anti-tumor pectin agents. The polymeric nature of this carbohydrate further facilitates its incorporation into future nanocell formulations.

Chapter 3 provides integrated conclusions for the body of work, and introduces applications that are being investigated as future directions. The remainder of Chapter 1 will introduce each of the topics covered throughout the thesis in additional detail.

### 1.2.1. The Nanocell

Current combination therapy regimens commonly consist of frequent dosing with anti-angiogenics interspersed with single large doses of anti-cancer agents<sup>24, 25, 32</sup>, however we propose that a delivery system enabling the focal build-up of a cytotoxic agent within vascularized regions of the tumor immediately prior to anti-angiogenic therapy would not only allow for greater bioavailability of the drug within the tumor but also target the cells most at risk for hypoxia, thus inhibiting the formation of new regions of hypoxia after therapy. Collapse of the tumor vasculature immediately after the focal loading of the cytotoxic agent would provide the added benefit of trapping the drug within the tumor, reducing systemic toxicity while promoting drug action.

Recently, the design of multichamber nanoparticle devices has been of benefit for improving the utility of nanotechnology in biomedical applications. The encapsulation of fluorescent semiconductor nanocrystals (quantum dots) within block-copolymer micelles has enabled enhanced biocompatibility for both *in vitro* and *in vivo* imaging<sup>33</sup>. Micellar nanocontainers consisting of a core containing an active therapeutic agent surrounded by a block-copolymer micelle has assisted in water dispersability of the agent and efficient delivery to specific cytoplasmic organelles<sup>34</sup>. Drug-loaded polymeric chitosan vesicles encapsulated within lipid have been demonstrated to enable controlled release of a single agent altered by the presence of the outer lipid chamber<sup>35</sup>. The advantages and disadvantages of current combination therapy discussed above have established a potential benefit for single vehicles able to deliver multiple drugs having different modes of action with controlled and distinct release properties. The use of multi-chambered nanodelivery vehicles has logical extensions to this application.

We demonstrate in this work a novel nanodelivery system for the spatio-temporal recruitment of anti-angiogenics and traditional cytotoxic agents at the site of tumor for a more optimal anti-tumor effect than standard co-administration of the two therapies. This delivery system consists of a small (<100nm) polymeric nanoparticle surrounded by a larger (~200nm) spherical lipid bilayer shell. Both the nanoparticle and the surrounding lipid shell are able to encapsulate separate chemotherapeutic agents with different release characteristics. In this case, the cytotoxic drug doxorubicin is covalently encapsulated within the nanoparticle, while the anti-angiogenic agent combretastatin A4 is preferentially partitioned within the lipid bilayer. These drug-loaded ‘nanocells’ are passively taken up by the tumor’s leaky vasculature through extravasation, though they may also be targeted to tumor by means of ligand or antibody binding. We demonstrate here that this spatio-temporal targeting of anti-angiogenics and cytotoxic agents enables a substantially greater anti-tumor effect than traditional co-administration of the two agents, as well as reduced systemic toxicity and tumor metastasis.

### **1.2.2. New Mechanistic Understandings of Nanoscale Drug Delivery**

Optimization of the nanocell release profiles for different drug combinations and different tumor models will benefit from new understandings of the mechanisms of drug release from nanoscale delivery vehicles. Numerous mathematical and computational models have been reported in the literature to describe drug release and particle breakdown for polymer-based delivery vehicles, though none have yet been able to quantitatively account for all factors relevant to drug release<sup>22, 36-43</sup>. Primarily governing drug release from bulk eroding polymers are the mass transport processes of drug diffusion and dissolution and the chemical processes of polymer degradation and erosion. These phenomena are typically modeled using one of two modeling approaches classified as diffusion-and-reaction and cellular automata models.

Diffusion and reaction models normally use a variant of Fick's second law of diffusion to model the events of diffusion and dissolution with the subsequent influence of polymer erosion. An early model developed by Harland et al was one of the first to take into account these processes for drug release from spherical microparticles.<sup>44, 45</sup> Later studies included the influence of polymer degradation on diffusion through erosion-dependent diffusivities<sup>46, 47</sup>, though it has been noted that this influence is not mechanistically modeled<sup>48</sup>. Cellular automata models are designed to simulate drug release by considering the process of matrix erosion as a random event. Since these models typically evaluate polymer degradation and erosion as the rate limiting steps, they are normally used for modeling drug release from surface-eroding polymers where the influence of mass transport phenomena on drug release is reduced<sup>22</sup>.

It is increasingly clear from existing models that the number of factors that influence the release of an agent from a polymer matrix is too unwieldy for a single model to incorporate. Such factors include water and drug diffusion, drug dissolution, polymer molecular weight, particle size and geometry, polymer degradation, micro-environment pH changes, autocatalysis, polymer swelling, and more<sup>44, 48, 49</sup>. Incorporation of all these factors is further complicated by a still incomplete understanding of the extent to which they influence the kinetics of drug release. Notably, very little has been reported regarding the modeling of drug release from polymeric nanoparticles, though these are becoming increasingly prominent in cancer therapeutics.

We present here a new, semi-empirical model of drug release from polymeric nanoparticles using a formulation of dexamethasone encapsulated within poly(lactic-co-glycolic acid) PLGA to set model parameters. We introduce a three-dimensional voxel-based framework for Monte Carlo simulations that enables direct investigation of the entire spherical nanoparticle during particle degradation and drug release. Due to implementation of this model at the

nanoscale, we utilize assumptions that simplify the model while still allowing multi-phase drug release to be simulated with good correlation to experimental results.

### 1.2.3. Development of Reduced-toxicity Antitumor Agents

It is our hope that the development of novel therapeutic compounds with reduced toxicity and utility both as structural and bioactive components will lead to more streamlined and efficient nanocells with rapid clinical application. One class of therapeutic agents that holds promise for this role is the carbohydrate pectin.

Pectin is a major component of all primary cell walls and consists of a complex carbohydrate network composed predominantly of galacturonic acid rich polysaccharides. In order to characterize this network, pectin has been divided into three major structural pectic-polysaccharides: homogalacturonan (HGA), rhamnogalacturonan-I (RG-I), and rhamnogalacturonan-II (RG-II).<sup>50</sup> HGA is a linear, unbranched polysaccharide consisting of (1→4)- $\alpha$ -linked-D-galacturonic acids containing 100-200 GalA residues. Methylesterification at the C-6 carboxyl occurs in 70-80% of the GalA residues. RG-I consists of as many as 100 repeats of the disaccharide (1→2)- $\alpha$ -L-rhamnose-(1→4)- $\alpha$ -D-galacturonic acid. Rhamnose residues in RG-I may be substituted at C-4 with predominantly neutral residue side chains which can vary in size from a single glycosyl residue to 50 or more, resulting in highly branched regions of pectin. In contrast to the first two pectin domains, RG-II appears to be a highly conserved and stable pectin domain. RG-II is not structurally related to RG-I, but instead is a branched pectic domain containing an HGA backbone. The RG-II backbone is substituted by 4 heteropolymeric side chains of consistent lengths containing eleven different sugars including apiose, aceric acid and 2-keto-3-deoxy-D-manno-octulosonic acid.

This complex pectin matrix may be fragmented via temperature, pH, or enzymatic modification into shorter, soluble oligosaccharide chains. One method of fractionating pectin has led to a subpopulation of pectin fragments with anti-tumor activity. These shorter pectin chains dissolve more readily in water and it is believed that they contain polysaccharides having affinity for cell-surface galectin-3<sup>51</sup>. Galectins are a family of animal lectins defined by their ability to recognize  $\beta$ -galactose and by conserved amino acid residues within the carbohydrate recognition domains. Currently 15 mammalian galectins have been identified, with several implicated in regulation of tumor apoptosis, inflammation, and immune escape<sup>52</sup>. Anti-tumor pectins have demonstrated therapeutic benefit for inhibiting tumor growth, adhesion, metastasis, and angiogenesis in several tumor models over the past decade including melanoma<sup>51, 53</sup>, breast cancer<sup>54</sup>, and colon cancer<sup>54</sup>, and one pilot phase II human clinical trial for prostate cancer<sup>55</sup>. The cheap, ready availability of pectin in combination with a virtual total lack of negative side effects has made understanding the mechanism of action of these intriguing new anticancer molecules of critical importance.

The proposed therapeutic mechanism is currently based upon evidence for the binding of pectin to galectin-3<sup>54</sup> and similarities between the activity of pectin and the activity of galectin-3 for inhibiting tumor function<sup>51</sup>. No direct mechanism has yet been elucidated, and this is probably due to multiple considerations. First, the temperature and pH modifications used to generate anti-tumor pectin are likely dependent upon the pectin starting source. Pectins obtained from major research laboratory vendors have considerable batch-to-batch variability in methods of isolation, and so can be expected to have substantial variations in starting structure. Despite this limitation, currently published anti-tumor pectin studies all use pre-processed pectins<sup>51, 53-57</sup>. The variability of pectin structures between studies also contributes to the challenge of

identifying structure-function relationships relating pectin structure and anti-tumor activity. Second, while galectin-3 appears to play a probable role in pectin mediated anti-tumor activity, the mechanism of action may not be entirely due to this galectin. Additional galectins, including galectin-1<sup>58, 59</sup>, have established roles in regulating tumor apoptosis, angiogenesis, and immune escape, and also have affinity for residues present within the complex polysaccharide environment of the pectin matrix<sup>60</sup>.

We demonstrate here an integrative approach for the standardization and structure-function analysis of a new class of anti-tumor modified pectins classified here as activated citrus pectin (ACP) obtained by a new methodology from a consistent source of native citrus pectin (NCP) isolated directly from lemon. We incorporate complementary analytical techniques to link ACP structure with binding to tumor galectin targets. We further establish a potential mechanism of action by elucidating key constituents of an ACP-induced anti-tumor intracellular signaling cascade. A better understanding of ACP anti-tumor activity as it relates to its structural modification will allow the synthesis of more effective and more reliable anti-tumor pectin agents. Further, pectin already has established use as a purely structural component in multiple modes of drug delivery formulations,<sup>61-63</sup> and ACP should incorporate well into future nanocell formulations.



### 1.3. References

1. Koch, S., Mayer, F., Honecker, F., Schittenhelm, M. & Bokemeyer, C. Efficacy of cytotoxic agents used in the treatment of testicular germ cell tumours under normoxic and hypoxic conditions in vitro. *Br J Cancer* 89, 2133-9 (2003).
2. Wouters, B. G. et al. Modulation of cell death in the tumor microenvironment. *Semin Radiat Oncol* 13, 31-41 (2003).
3. Pennacchietti, S. et al. Hypoxia promotes invasive growth by transcriptional activation of the met protooncogene. *Cancer Cell* 3, 347-61 (2003).
4. Folkman, J. Fundamental concepts of the angiogenic process. *Curr Mol Med* 3, 643-51 (2003).
5. Gimbrone, M. A., Jr., Leapman, S. B., Cotran, R. S. & Folkman, J. Tumor dormancy in vivo by prevention of neovascularization. *J Exp Med* 136, 261-76 (1972).
6. Folkman, J. What is the evidence that tumors are angiogenesis dependent? *J Natl Cancer Inst* 82, 4-6 (1990).
7. Folkman, J. Seminars in Medicine of the Beth Israel Hospital, Boston. Clinical applications of research on angiogenesis. *N Engl J Med* 333, 1757-63 (1995).
8. Hanahan, D. & Folkman, J. Patterns and emerging mechanisms of the angiogenic switch during tumorigenesis. *Cell* 86, 353-64 (1996).
9. Hori, A. et al. Suppression of solid tumor growth by immunoneutralizing monoclonal antibody against human basic fibroblast growth factor. *Cancer Res* 51, 6180-4 (1991).
10. Liotta, L. A. & Stetler-Stevenson, W. G. Tumor invasion and metastasis: an imbalance of positive and negative regulation. *Cancer Res* 51, 5054s-5059s (1991).
11. Tonini, T., Rossi, F. & Claudio, P. P. Molecular basis of angiogenesis and cancer. *Oncogene* 22, 6549-56 (2003).

12. Bhushan, M., Young, H. S., Brenchley, P. E. & Griffiths, C. E. Recent advances in cutaneous angiogenesis. *Br J Dermatol* 147, 418-25 (2002).
13. Seymour, L. W. Passive tumor targeting of soluble macromolecules and drug conjugates. *Crit Rev Ther Drug Carrier Syst* 9, 135-87 (1992).
14. Baban, D. F. & Seymour, L. W. Control of tumour vascular permeability. *Adv Drug Deliv Rev* 34, 109-119 (1998).
15. Hobbs, S. K. et al. Regulation of transport pathways in tumor vessels: role of tumor type and microenvironment. *Proc Natl Acad Sci U S A* 95, 4607-12 (1998).
16. Yuan, F. et al. Vascular permeability in a human tumor xenograft: molecular size dependence and cutoff size. *Cancer Res* 55, 3752-6 (1995).
17. Folkman, J., Winsey, S., Cole, P. & Hodes, R. Isolated perfusion of thymus. *Exp Cell Res* 53, 205-14 (1968).
18. Ribatti, D., Vacca, A. & Presta, M. The discovery of angiogenic factors: a historical review. *Gen Pharmacol* 35, 227-31 (2000).
19. Rosenbohm, C., Lundt, I., Christensen, T. I. & Young, N. G. Chemically methylated and reduced pectins: preparation, characterisation by <sup>1</sup>H NMR spectroscopy, enzymatic degradation, and gelling properties. *Carbohydr Res* 338, 637-49 (2003).
20. Verheul, H., Voest, E. & Schlingemann, R. Are tumours angiogenesis-dependent? *J Pathol* 202, 5-13 (2004).
21. Bergers, G., Javaherian, K., Lo, K. M., Folkman, J. & Hanahan, D. Effects of angiogenesis inhibitors on multistage carcinogenesis in mice. *Science* 284, 808-12 (1999).
22. Zygourakis, K. & Markenscoff, P. A. Computer-aided design of bioerodible devices with optimal release characteristics: a cellular automata approach. *Biomaterials* 17, 125-35 (1996).

23. Kerbel, R. S. Clinical trials of antiangiogenic drugs: opportunities, problems, and assessment of initial results. *J Clin Oncol* 19, 45S-51S (2001).
24. Panyam, J. & Labhasetwar, V. Biodegradable nanoparticles for drug and gene delivery to cells and tissue. *Advanced Drug Delivery Reviews* 55, 329-347 (2003).
25. Grosios, K., Loadman, P. M., Swaine, D. J., Pettit, G. R. & Bibby, M. C. Combination chemotherapy with combretastatin A-4 phosphate and 5-fluorouracil in an experimental murine colon adenocarcinoma. *Anticancer Res* 20, 229-33 (2000).
26. Steeg, P. S. Angiogenesis inhibitors: motivators of metastasis? *Nat Med* 9, 822-3 (2003).
27. Koch, S., Mayer, F., Honecker, F., Schittenhelm, M. & Bokemeyer, C. Efficacy of cytotoxic agents used in the treatment of testicular germ cell tumours under normoxic and hypoxic conditions in vitro. *Br J Cancer* 89, 2133-9 (2003).
28. Kinoshita, M., Johnson, D. L., Shatney, C. H., Lee, Y. L. & Mochizuki, H. Cancer cells surviving hypoxia obtain hypoxia resistance and maintain anti-apoptotic potential under reoxygenation. *Int J Cancer* 91, 322-6 (2001).
29. Comerford, K. M. et al. Hypoxia-inducible factor-1-dependent regulation of the multidrug resistance (MDR1) gene. *Cancer Res* 62, 3387-94 (2002).
30. Albini, A. et al. A rapid in vitro assay for quantitating the invasive potential of tumor cells. *Cancer Res* 47, 3239-45 (1987).
31. Brigger, I., Dubernet, C. & Couvreur, P. Nanoparticles in cancer therapy and diagnosis. *Adv Drug Deliv Rev* 54, 631-51 (2002).
32. te Velde, E. A. et al. Enhanced antitumour efficacy by combining conventional chemotherapy with angiostatin or endostatin in a liver metastasis model. *Br J Surg* 89, 1302-9 (2002).
33. Dubertret, B. et al. In vivo imaging of quantum dots encapsulated in phospholipid micelles. *Science* 298, 1759-62 (2002).

34. Savic, R., Luo, L., Eisenberg, A. & Maysinger, D. Micellar nanocontainers distribute to defined cytoplasmic organelles. *Science* 300, 615-8 (2003).
35. McPhail, D., Tetley, L., Dufes, C. & Uchegbu, I. F. Liposomes encapsulating polymeric chitosan based vesicles--a vesicle in vesicle system for drug delivery. *Int J Pharm* 200, 73-86 (2000).
36. Gopferich, A. & Langer, R. Modeling of polymer erosion. *Macromolecules* 26, 4105-4112 (1993).
37. Gopferich, A. Erosion of composite polymer matrices. *Biomaterials* 18, 397-403 (1997).
38. Faisant, N., Siepmann, J. & Benoit, J. P. PLGA-based microparticles: elucidation of mechanisms and a new, simple mathematical model quantifying drug release. *European Journal of Pharmaceutical Sciences* 15, 355-366 (2002).
39. Gopferich, A. & Langer, R. Modeling monomer release from bioerodible polymers. *Journal of Controlled Release* 33, 55-69 (1995).
40. Göpferich, A. & Langer, R. Modeling of polymer erosion in three dimensions: Rotationally symmetric devices. *AIChE Journal* 41, 2292-2299 (1995).
41. Siepmann, J., Faisant, N. & Benoit, J.-P. A New Mathematical Model Quantifying Drug Release from Bioerodible Microparticles Using Monte Carlo Simulations. *Pharmaceutical Research* 19, 1885-1893 (2002).
42. Polakovic, M., Gorner, T., Gref, R. & Dellacherie, E. Lidocaine loaded biodegradable nanospheres. II. Modelling of drug release. *J Control Release* 60, 169-77 (1999).
43. Zhang, M., Yang, Z., Chow, L. L. & Wang, C. H. Simulation of drug release from biodegradable polymeric microspheres with bulk and surface erosions. *J Pharm Sci* 92, 2040-56 (2003).
44. Siepmann, J. & Gopferich, A. Mathematical modeling of bioerodible, polymeric drug delivery systems. *Adv Drug Deliv Rev* 48, 229-47 (2001).

45. Siepman, J., Elkharraz, K., Siepman, F. & Klose, D. How autocatalysis accelerates drug release from PLGA-based microparticles: a quantitative treatment. *Biomacromolecules* 6, 2312-9 (2005).
46. He, J., Zhong, C. & Mi, J. Modeling of drug release from bioerodible polymer matrices. *Drug Deliv* 12, 251-9 (2005).
47. Raman, C., Berkland, C., Kim, K. & Pack, D. W. Modeling small-molecule release from PLG microspheres: effects of polymer degradation and nonuniform drug distribution. *J Control Release* 103, 149-58 (2005).
48. Arifin, D. Y., Lee, L. Y. & Wang, C. H. Mathematical modeling and simulation of drug release from microspheres: Implications to drug delivery systems. *Adv Drug Deliv Rev* 58, 1274-325 (2006).
49. Gopferich, A. Mechanisms of polymer degradation and erosion. *Biomaterials* 17, 103-114 (1996).
50. Willats, W. G., McCartney, L., Mackie, W. & Knox, J. P. Pectin: cell biology and prospects for functional analysis. *Plant Mol Biol* 47, 9-27 (2001).
51. Inohara, H. & Raz, A. Effects of natural complex carbohydrate (citrus pectin) on murine melanoma cell properties related to galectin-3 functions. *Glycoconj J* 11, 527-32 (1994).
52. Liu, F. T. & Rabinovich, G. A. Galectins as modulators of tumour progression. *Nat Rev Cancer* 5, 29-41 (2005).
53. Platt, D. & Raz, A. Modulation of the lung colonization of B16-F1 melanoma cells by citrus pectin. *J Natl Cancer Inst* 84, 438-42 (1992).
54. Nangia-Makker, P. et al. Inhibition of human cancer cell growth and metastasis in nude mice by oral intake of modified citrus pectin. *J Natl Cancer Inst* 94, 1854-62 (2002).
55. Guess, B. W. et al. Modified citrus pectin (MCP) increases the prostate-specific antigen doubling time in men with prostate cancer: a phase II pilot study. *Prostate Cancer Prostatic Dis* 6, 301-4 (2003).

56. Glinskii, O. V. et al. Mechanical entrapment is insufficient and intercellular adhesion is essential for metastatic cell arrest in distant organs. *Neoplasia* 7, 522-7 (2005).
57. Pienta, K. J. et al. Inhibition of spontaneous metastasis in a rat prostate cancer model by oral administration of modified citrus pectin. *J Natl Cancer Inst* 87, 348-53 (1995).
58. Camby, I., Le Mercier, M., Lefranc, F. & Kiss, R. Galectin-1: a small protein with major functions. *Glycobiology* 16, 137R-157R (2006).
59. Thijssen, V. L. et al. Galectin-1 is essential in tumor angiogenesis and is a target for antiangiogenesis therapy. *Proc Natl Acad Sci U S A* 103, 15975-80 (2006).
60. Hirabayashi, J. et al. Oligosaccharide specificity of galectins: a search by frontal affinity chromatography. *Biochim Biophys Acta* 1572, 232-54 (2002).
61. Esposito, E., Cortesi, R., Luca, G. & Nastruzzi, C. Pectin-based microspheres: a preformulatory study. *Ann N Y Acad Sci* 944, 160-79 (2001).
62. Muhiddinov, Z., Khalikov, D., Speaker, T. & Fassihi, R. Development and characterization of different low methoxy pectin microcapsules by an emulsion-interface reaction technique. *J Microencapsul* 21, 729-41 (2004).
63. Kosaraju, S. L. Colon targeted delivery systems: review of polysaccharides for encapsulation and delivery. *Crit Rev Food Sci Nutr* 45, 251-8 (2005).

## **2. Novel Nanoscale Delivery Systems for Combination Chemotherapy**

This chapter (2.1) presents the nanocell: a multi-compartmental nanoscale drug delivery vehicle for the controlled spatio-temporal delivery of combination chemotherapy. The nanocell comprises a nuclear nanoparticle within an extranuclear pegylated-lipid envelope, and is preferentially taken up by the tumor. The nanocell enables a temporal release of two drugs: the outer envelope first releases an anti-angiogenesis agent, causing a vascular shutdown; the inner nanoparticle, which is trapped inside the tumor, then releases a chemotherapy agent. This focal release within a tumor results in improved therapeutic index with reduced toxicity. The technology can be extended to additional agents, so as to target multiple signaling pathways or distinct tumor compartments, enabling the model of an 'integrative' approach in cancer therapy.

This chapter (2.2) also presents a modified nanoscale delivery vehicle for imaging angiogenesis. As tumors undergo rapid growth, they must generate their own vascular network in order to provide the nutrients necessary for continued expansion and spread. In vivo imaging of tumor vascularization is now of paramount importance, as this is both a sign of increasing tumor malignancy and a potential target for new therapies. We demonstrate here a method for imaging and specifically identifying tumor-specific vasculature using quantum dots encapsulated within nanoscale lipid membranes, combining the fluorescent properties of quantum dots with the bioavailability and tumor-specific interstitial uptake of the lipid vehicle.

This chapter (2.3) also presents a new computational model for drug release from nanoscale delivery vehicles. The use of polymeric nanoparticles as drug delivery devices is becoming increasingly prevalent in a variety of therapeutic applications. Despite their widespread clinical use, the factors influencing the release profiles of nanoparticle-encapsulated drugs are still not quantitatively understood. We present here a new, semi-empirical model of

drug release from polymeric nanoparticles using a formulation of dexamethasone encapsulated within poly(lactic-co-glycolic acid) PLGA to set model parameters. We introduce a three-dimensional voxel-based framework for Monte Carlo simulations that enables direct investigation of the entire spherical nanoparticle during particle degradation and drug release. Due to implementation of this model at the nanoscale, we utilize assumptions that simplify the model while still allowing multi-phase drug release to be simulated with good correlation to experimental results.

This chapter (2.4) also presents the generation and characterization of new carbohydrate-based anti-tumor carbohydrates. We demonstrate here an integrative approach for the standardization and structure-function analysis of a new class of anti-tumor modified pectins classified here as activated citrus pectin (ACP) obtained by a new methodology from a consistent source of native citrus pectin (NCP) isolated directly from lemon. We incorporate complementary analytical techniques to link ACP structure with binding to tumor galectin targets. We further provide evidence for a mechanism of action by elucidating key constituents of an ACP-induced anti-tumor intracellular signaling cascade. A better understanding of ACP anti-tumor activity as it relates to its structural modification will allow the synthesis of more effective and more reliable anti-tumor pectin agents. The polymeric nature of this carbohydrate further facilitates its incorporation into future nanocell formulations.



## 2.1. Spatio-temporal Targeting of Tumor Cells and Neovasculature: The Nanocell

### 2.1.1. Introduction

The material found in Chapter 2.1 has previously been published: Sengupta and Eavarone et al, Temporal targeting of tumor cells and neovasculature with a nanoscale delivery system. *Nature* 436, 568-72 (2005) and has been reprinted with permission. In the continuing search for effective treatments for cancer, the emerging model is the combination of traditional chemotherapy with anti-angiogenesis agents<sup>1</sup> that inhibit blood vessel growth. However, the implementation of this strategy has faced two major obstacles. First, the long-term shutdown of tumor blood vessels by the anti-angiogenesis agent can prevent the tumor from receiving a therapeutic concentration of the chemotherapy agent. Second, inhibiting blood supply drives the intra-tumoral accumulation of hypoxia-inducible factor-1 $\alpha$  (HIF1- $\alpha$ ); overexpression of HIF1- $\alpha$  is correlated with increased tumor invasiveness and resistance to chemotherapy.<sup>2,3,4,5</sup> Here we report the disease-driven engineering of a drug delivery system, a 'nanocell', which overcomes these barriers unique to solid tumors. The nanocell comprises a nuclear nanoparticle within an extranuclear pegylated-lipid envelope, and is preferentially taken up by the tumor. The nanocell enables a temporal release of two drugs: the outer envelope first releases an anti-angiogenesis agent, causing a vascular shutdown; the inner nanoparticle, which is trapped inside the tumor, then releases a chemotherapy agent. This focal release within a tumor results in improved therapeutic index with reduced toxicity. The technology can be extended to additional agents, so as to target multiple signaling pathways or distinct tumor compartments, enabling the model of an 'integrative' approach in cancer therapy.

Although the inhibition of angiogenesis is an elegant concept in cancer therapy<sup>1</sup>, there are concerns about its implementation. Anti-angiogenesis therapy-induced tumoral hypoxia

upregulates genes<sup>2</sup> that can significantly reduce the pro-apoptotic effect of chemotherapy<sup>3</sup> leading to 'reactive resistance'<sup>4,5</sup>. Furthermore, the activation of the hypoxic response can enhance the metastatic and invasive potential of tumor cells<sup>6,7</sup>, although this has not been resolved clinically<sup>8</sup>. We reasoned that the optimal strategy to overcome these limitations is to sequentially expose the tumor to cytotoxic agents after a vascular shutdown induced by anti-angiogenesis therapy. However, two issues complicate this approach. First, the suppression of tumor growth requires long-term administration of angiogenesis inhibitors, whereas chemotherapy is usually given in short treatment cycles<sup>9</sup>. Second, the chronic administration of an anti-angiogenesis agent impairs blood flow inside the tumor microenvironment, precluding the intra-tumoral build-up of a therapeutically effective concentration of the chemotherapeutic agent.

### **2.1.2. Materials and Methods**

#### **Synthesis and characterization of nanocells**

Activated PLGA was dissolved in dimethylformamide and reacted with doxorubicin and triethylamine at room temperature (20 °C) under a nitrogen atmosphere (stoichiometric molar ratio of activated PLGA:doxorubicin:triethylamine, 1:1:4)<sup>13</sup>. Nanoparticles were formulated from the PLGA copolymer–doxorubicin conjugates by using an emulsion–solvent evaporation technique. For scanning electron microscopy, dehydrated nanoparticles were coated with gold on a carbon grid. They were analysed using a Jeol electron microscope (magnification times 3,700). Nanoparticle size fractions were recovered by ultracentrifugation at 10,000 g, 25,000 g and 50,000 g, which also removed free doxorubicin from the PLGA–doxorubicin conjugates. The smallest fraction was extruded through a membrane (pore size 100 nm) to obtain

nanoparticles for encapsulation within nanocells. Phosphatidylcholine:cholesterol:PEG-DSPE (2:1:0.2 molar ratio) lipid membranes were prepared by dissolving the lipids in chloroform in a round-bottomed flask. Combretastatin A4 was added at a 0.9:1 drug:lipid molar ratio. To fabricate the nanocells, doxorubicin-conjugated nanoparticles were added to the aqueous lipid resuspension buffer, which was extruded through a membrane (pore size 200 nm). Sizing was performed by dynamic light scattering and transmission electron microscopy. For additional information see supplementary methods.

### **Cell culture studies**

B16/F10 cells were plated at a concentration of 5 times  $10^4$  cells per well and left to grow for 24 h in 5% fetal calf serum. The cells were exposed to increasing concentrations of free or nanoparticle-conjugated doxorubicin and incubated for 48 h, after which the cells were counted with the Trypan blue exclusion method. EC50 was calculated by curve-fitting. For additional information see supplementary methods.

### **Release kinetics characterization**

Drug-loaded nanocells were suspended in 1 ml of PBS buffer or hypoxic-cell lysate and sealed in a dialysis bag (molecular mass cut-off 10 kDa). The dialysis bag was incubated in 20 ml of PBS buffer at 37 °C with gentle shaking. Aliquots were extracted from the incubation medium at predetermined intervals, and released drug was quantified by reverse-phase HPLC with a C18 column, using a linear gradient of acetonitrile and water eluents. For additional information see supplementary methods.

### **In vitro tumor–endothelium co-culture studies**

The co-culture of GFP-positive B16/F10 melanoma with human umbilical vein endothelial cells on a three-dimensional Matrigel matrix was exposed to different treatments. The cells were fixed with 4% paraformaldehyde, incubated with propidium iodide and analysed with a confocal microscope. Quantification was performed with a planimetric point-count method using a 224-intersection point square reticulum. Data were expressed as the ratio of each component to the total area covered by cells. For additional information see supplementary methods.

### **In vivo tumor studies**

GFP-positive BL6/F10 melanoma cells (3 times  $10^5$ ) or Lewis lung carcinoma cells ( $2.5 \times 10^5$ ) were implanted in male C57/BL6 mice. Treatment was started when the tumors reached  $50 \text{ mm}^3$  in volume. Each formulation was prepared, quantified and diluted so that 100 microl (intravenous) was equivalent to  $50 \text{ mg kg}^{-1}$  combretastatin and  $500 \text{ microg kg}^{-1}$  doxorubicin. The animals were killed at defined time points, and the tumors were excised for histopathology. Simultaneously, 1 ml of blood was drawn through cardiac puncture and analysed for a toxicity profile of the treatment regimens. For additional information see supplementary methods.

### **Tissue distribution studies**

Nanocells were fabricated with fluorescein dye and injected into tumor-bearing mice. The animals were killed at 5, 10 and 24 h after injection. Serum, tumor, liver, lungs and spleen were collected during necropsy, and fluorescein was extracted from these tissues with methanol, detected with a fluorescence plate reader, and normalized to the tissue weight. In another study, nanocells were fabricated with Quantum Dots in the core, and injected intravenously into tumor-

bearing mice. The animals were killed at different time points, and the highly vascular organs were extracted during necropsy. The tissue sections (30 microm thick) were immunostained to delineate the blood vessels. Confocal images were captured at 512 pixels times 512 pixels resolution, with excitation using a 488-nm laser line and emissions at the fluorescein isothiocyanate (FITC)/rhodamine wavelengths. Depth-coding was performed with LSM510 software. For additional information see supplementary methods.

### **Immunohistology**

For analysis of tumor vasculature, permeabilized cryosections of the tumors were immunoprobed for vWF, an endothelial cell marker. For study of apoptosis, TUNEL staining was performed with Texas red-labeled nucleotide in accordance with the manufacturer's instructions (Roche). The same sections were also stained simultaneously for HIF1- $\alpha$ , using appropriate primary and FITC-labelled secondary antibodies. Images were captured with a Leica LSM510 confocal microscope at a 512 pixels times 512 pixels resolution. For quantifying metastatic nodes, the liver and lungs were harvested from the animals during necropsy, fixed in paraformaldehyde and embedded in paraffin. Thin sections were stained with haematoxylin/eosin and imaged with a Zeiss LSM510 confocal microscope with FITC/rhodamine filters. Metastatic nodes were quantified by counting the number of yellow foci in each section. For additional information see supplementary methods.

### **Western blotting**

Tissue samples were lysed in sample buffer and resolved on a 4–12% gradient SDS–polyacrylamide-gel electrophoresis gel. The proteins were transferred to a nitrocellulose membrane, blocked, and probed with the appropriate primary antibodies and secondary

horseradish peroxidase-labelled antibodies. Proteins were detected by chemiluminescence and quantified with a Kodak 2000 gel-imaging system. For additional information see supplementary methods.

### **2.1.3. Results and Discussion**

To address this challenge we designed a novel delivery system, termed a nanocell, comprising a nanoscale pegylated-phospholipid block-copolymer envelope coating a nuclear nanoparticle. A chemotherapeutic agent is conjugated to the nanoparticle and an anti-angiogenesis agent is trapped within the lipid envelope. We proposed that the disruption of this envelope inside a tumor would result in a rapid deployment of the anti-angiogenesis agent, leading to vascular collapse and the intra-tumoral trapping of the nanoparticles (Fig. 1). The subsequent slow release of the cytotoxic agent from the nanoparticle should then kill the tumor cells.

As a proof of concept, we selected doxorubicin and combretastatin-A4 as the cytotoxic agent and the anti-angiogenesis drug, respectively. Doxorubicin induces apoptosis by intercalating with the DNA, causing scission<sup>10</sup>. Combretastatin causes a rapid vascular shutdown inside a tumor by disrupting the cytoskeletal structures<sup>11</sup>. The nanoparticles were fabricated from the biodegradable and nonbioactive copolymer poly-(lactic-co-glycolic) acid (PLGA)<sup>12</sup>. Doxorubicin was conjugated to PLGA (Fig. 2a) to achieve a slow release profile, distinct from the characteristic 'burst' release associated with nanoparticles. In vitro cell culture studies revealed a shift in the concentration–effect curve of the doxorubicin–PLGA conjugate, for which the concentration giving half-maximal response (EC50) was about 10.59 microg, compared with free doxorubicin (EC50 approximately 5.93 microg; Fig. 3c). This shift in the concentration–

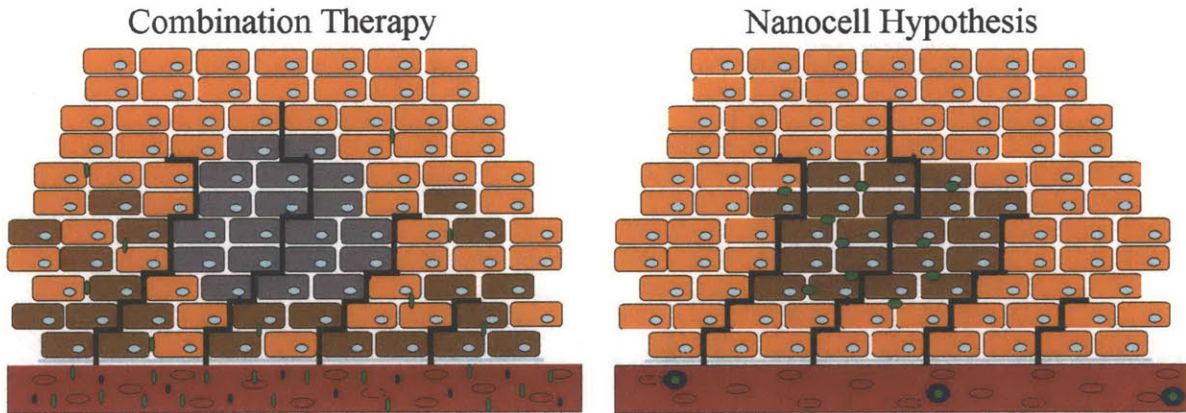


**Figure 1. Diagram of nanocell therapy.** Current combination therapy regimens commonly consist of frequent dosing with anti-angiogenics interspersed with single large doses of anti-cancer agents, however we propose that a delivery system enabling the focal build-up of a cytotoxic agent within vascularized regions of the tumor immediately prior to anti-angiogenic therapy would not only allow for greater bioavailability of the drug within the tumor but also target the cells most at risk for hypoxia, thus inhibiting the formation of new regions of hypoxia after therapy. Collapse of the tumor vasculature immediately after the focal loading of the cytotoxic agent would provide the added benefit of trapping the drug within the tumor, reducing systemic toxicity while promoting drug action. Gray shading: hypoxic tumor cells; brown shading: necrotic tumor cells.

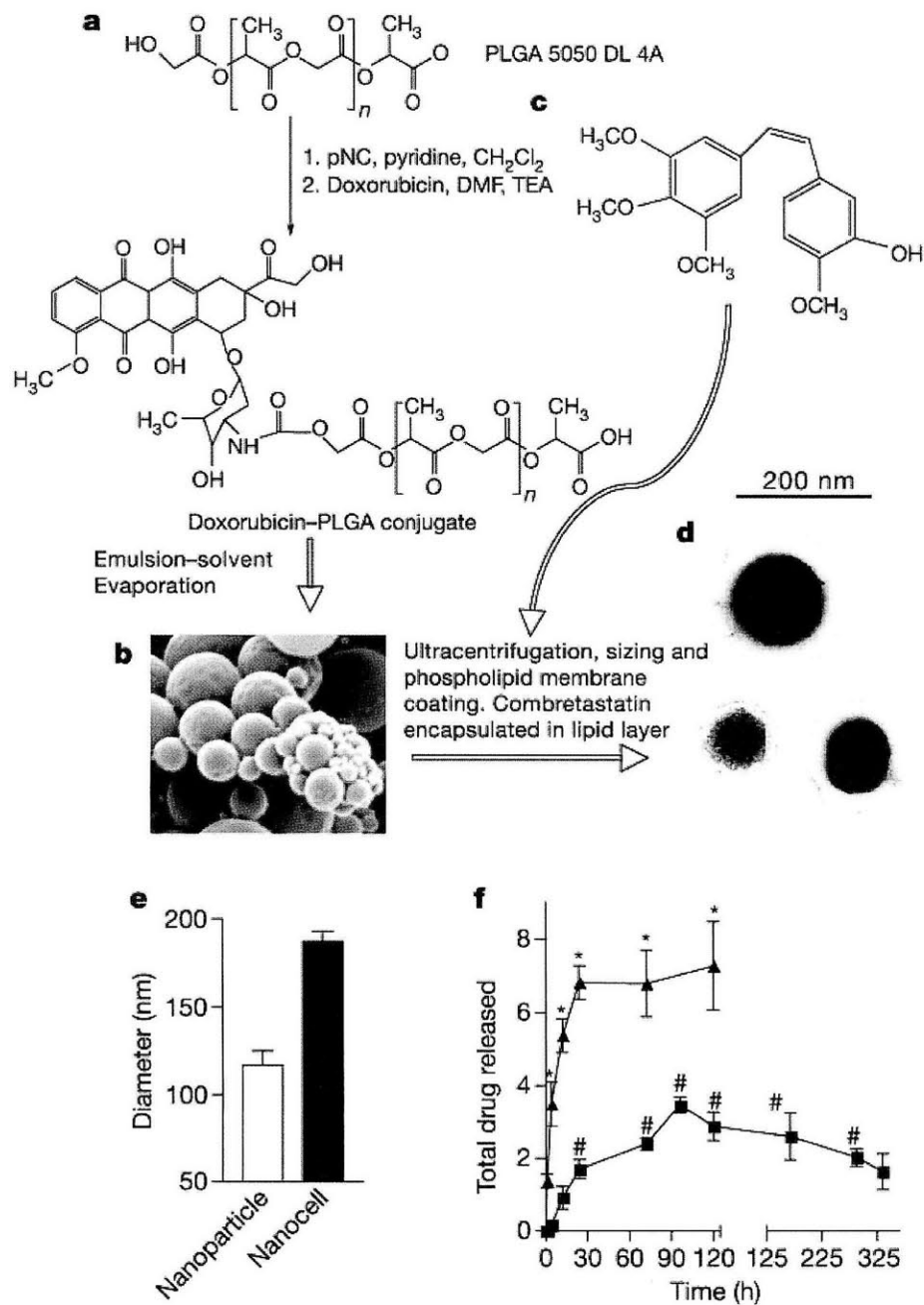


**Figure 2. Synthesis and characterization of a combretastatin–doxorubicin nanocell.** a, Diagram of conjugation reactions between doxorubicin and PLGA 5050.DMF, dimethylformamide; pNC, p-nitrophenyl-chloroformate; TEA, triethylamine. b, Scanning electron micrograph of heterogeneous nanoparticles. c, Combretastatin is encapsulated in the lipid envelope. d, Transmission electron micrograph of the cross-section of three nanocells shows the dark nuclear nanoparticle within the phospholipid block-copolymer envelope. e, Dynamic light scattering shows that nanoparticles of defined sizes were used for encapsulation within the envelope. f, Physicochemical release kinetics shows the temporal release of combretastatin (triangles, scale in 10<sup>2</sup> microg) and doxorubicin (squares, scale in microg). Results are means plus/minus s.e.m. (n = 4). Asterisk, P < 0.002; hash, P < 0.001.



effect curve indicates that the doxorubicin–PLGA oligomers are inactive and have to degrade further into bioactive doxorubicin–PLGA fragments and free drug, which is consistent with earlier reports<sup>13</sup>. Although there was heterogeneity in the sizes of nanoparticles synthesized (Fig. 2b), we isolated a homogeneous population of nanoparticles between 80–120 nm (Fig. 2e).

To synthesize the nanocell, these nanoparticles were nucleated inside a nanoscale phospholipid block-copolymer envelope composed of 2,000-Da poly-(ethylene glycol) distearoylphosphatidylethanolamine (PEG-DSPE), phosphatidylcholine and cholesterol, in an optimal ratio with combretastatin. The selection of combretastatin, a lipophilic cis-stilbene (Fig. 2c), allowed optimal loading by partitioning into the lipid bilayer. Transmission electron microscopy showed the ultrastructure as being similar to a biological cell—a nuclear core surrounded by a lighter lipid membrane—hence the metaphor 'nanocell' (Fig. 2d). The size of the nanocells ranged between 180 and 200 nm in diameter (Fig. 2e).

To evaluate the nanocell physicochemically, we quantified the release kinetics for each drug. We observed a rapid release of combretastatin, reaching significant levels within 12 h. In contrast, the doxorubicin–PLGA oligomer was found to degrade into smaller doxorubicin–PLGA fragments and free doxorubicin significantly more slowly (Fig. 2f), extending over 15 days. This slow release underlines the shift in the concentration–effect curves, the EC<sub>50</sub> being calculated at a time before the complete breakdown of the drug–polymer conjugate.

To correlate the temporal-release kinetics with the pathophysiology, we harnessed a tumor-endothelium co-culture bioassay<sup>14</sup>. The co-cultures were exposed to different treatments for defined periods, after which they were evaluated by dual-fluorescence confocal microscopy. As shown in Fig. 3, prolonged (30 h), but not short (12 h), incubation of the co-culture with

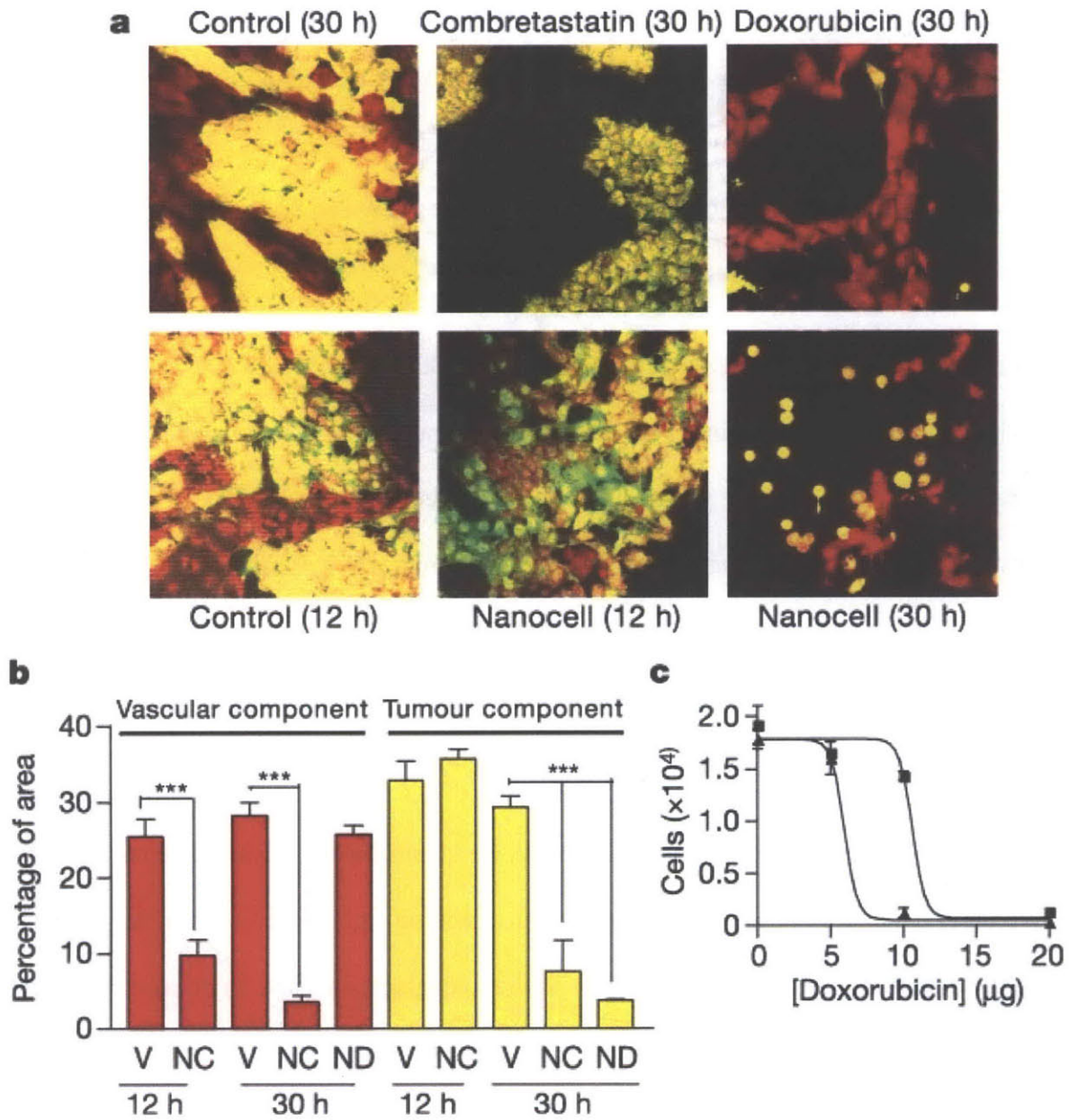


**Figure 3: Bioassay of the nanocell with a GFP-positive melanoma–endothelial cell three-dimensional co-culture system.** a, Micrographs showing the effect of treatments on melanoma (yellow) or endothelium (red). b, Stereological quantification of the result. Treatment with nanocells (NC) results in temporal ablation of vasculature followed by destruction of the tumor cells. Liposomal combretastatin ( $250 \text{ microg ml}^{-1}$ ) (L[C]) and doxorubicin-conjugated nanoparticles (ND) ( $20 \text{ microg ml}^{-1}$  doxorubicin) results in selective loss of vasculature and tumor respectively. Results are means plus/minus s.e.m. from three independent experiments. V, vehicle. Three asterisks,  $P < 0.001$  (analysis of variance with Bonferroni's post-hoc test). c, Concentration–effect curve of free doxorubicin (triangles) and PLGA-conjugated doxorubicin (squares) on B16/F10 cells. Results are means plus/minus s.e.m. for two independent experiments.

doxorubicin-conjugated nanoparticles, alone, resulted in a complete ablation of the tumor cells without affecting the endothelial cells. This was consistent with the results obtained with free doxorubicin<sup>14</sup>. In contrast, incubation with combretastatin-encapsulated liposomes resulted in a rapid collapse of the vascular network without affecting the tumor cells. In the nanocell-treated groups, collapse of the vasculature was evident as early as 12 h, at which time point the tumor cells remained unaffected. A complete ablation of the co-culture was achieved by 30 h, which is consistent with the kinetics profile of the drug release rate. Although this release profile may not mimic the *in vivo* state, the close similarity of *ex vitro* release profiles in hypoxic-tumor cell lysate and PBS, together with the bioassay results, emphasizes that a similar release pattern over time would be functional in the acidic microenvironment of the tumor.

To validate the therapeutic efficacy of this treatment, we randomly sorted mice bearing established (green fluorescent protein (GFP)-positive) B16/F10 melanomas or Lewis lung carcinoma into six groups and treated each group with one of the following: PBS (control); nanocells containing doxorubicin nanoparticles but lacking combretastatin (NC[D]); combretastatin-encapsulated liposomes (L[C]); co-administration of NC[D] + L[C]; nanocells containing both doxorubicin and combretastatin (NC); and a simple liposomal system encapsulating both doxorubicin and combretastatin (L[CD]). A separate melanoma-bearing group received half the dose of NC. The mice injected with PBS formed large tumors by day 17 (the day after the last injection), and consequently were killed. The animals in the other groups were also killed at the same time point to evaluate the effect of the treatments on tumor pathology. In a separate experiment, another group of animals was given seven cycles of treatment with NC to evaluate the effect over a longer period.

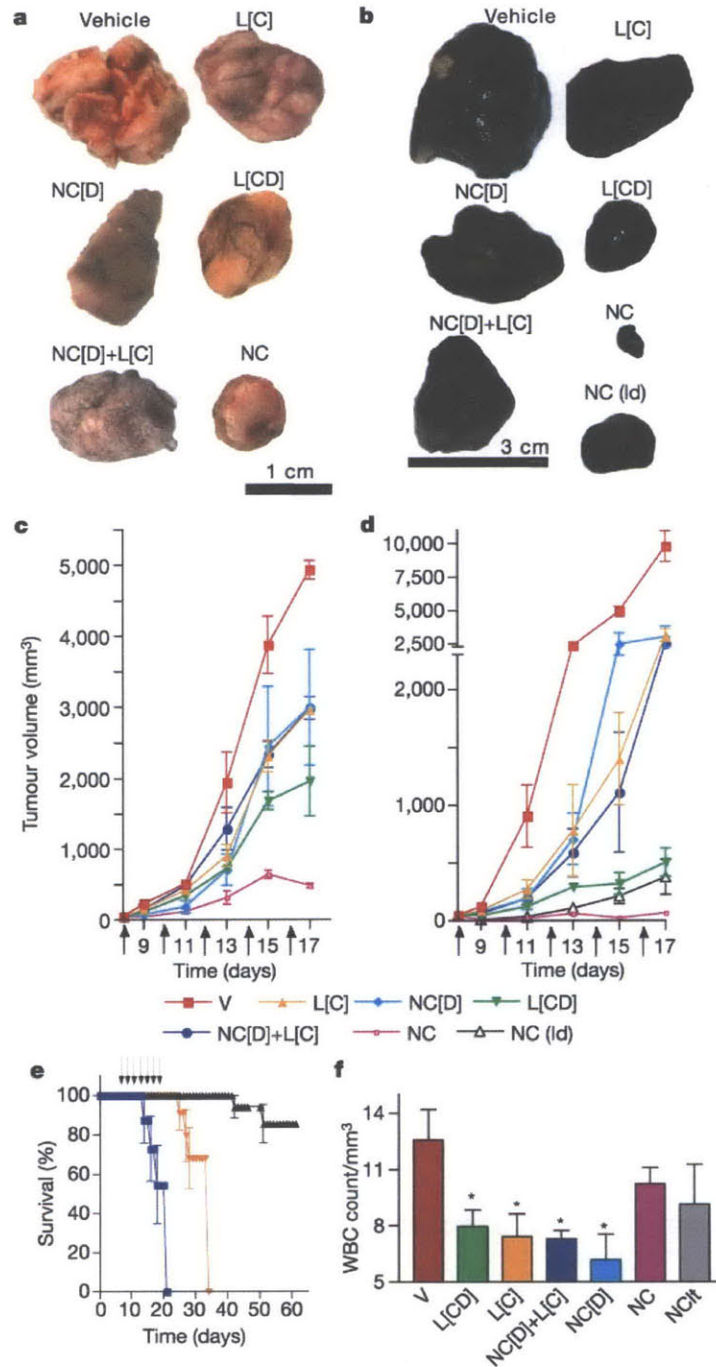


**Figure 4: Nanocell therapy inhibits B16/F10 melanoma and Lewis lung carcinoma growth.** a, b, Excised Lewis lung carcinoma (a) and B16/F10 melanoma (b) comparing the effects of NC and the effects of nanocells with NC[D], L[C], co-injection of NC[D] + L[C], L[CD] and a lower dose (ld) of NC. Control groups received saline. c, d, Tumor volume in different treatment groups for Lewis lung carcinoma (c) and B16/F10 carcinoma (d). Results are means plusminus s.e.m. V, vehicle. e, Kaplan–Meier survival graph showing that treatment with NC significantly increases the lifespan: blue squares, vehicle; black triangles, NC; orange triangles, L[CD]. f, The effect of different treatments on the white blood cell (WBC) counts. Results are means plusminus s.e.m. Arrows represent drug administration. \*P < 0.05 vs. vehicle (V).

As shown in Fig. 4, both the L[C] and NC[D] groups showed tumor inhibition compared with the PBS-treated group. The NC[D] + L[C] treatment group had only a negligible improvement over either of the treatments alone, which could arise from the preclusion of NC[D] after chronic administration of the anti-angiogenic agent. In contrast, L[CD] treatment induced a greater inhibition than NC[D] + L[C], possibly from the simultaneous release of free doxorubicin and combretastatin. A greater exposure to the cytotoxic agent at the acute phases of the therapy, resulting from the normalization of the tortuosity of tumor vessels<sup>15</sup>, has been reported to underlie such an outcome. Another explanation could be that low-dose (that is, 'metronomic') chemotherapy can also exert an anti-angiogenic effect<sup>16</sup>. However, the NC-treated groups, when compared directly with the equivalent doses of the NC[D], L[C], NC[D] + L[C] and L[CD] groups, had a distinctly superior outcome. NC treatment-induced inhibition of tumor growth was dose-dependent, although melanoma was more susceptible than lung carcinoma. Furthermore, there was a significant increase in the lifespan of the NC-treated animals (Fig. 4e).

These observations bring out two issues. First, it is well known that tumor cell response to chemotherapy is a function of the chemotherapeutic agent. As observed here, the greater susceptibility of melanoma than the Lewis lung carcinoma to this current drug combination is consistent with this view. Second, the effectiveness of a chemotherapeutic agent is likely to be a function of signaling pathways and the responses to extracellular signaling from the heterotypic environment that impinge on the tumor cells. This underscores the need to develop chemotherapeutic approaches while keeping in perspective the different compartments of distinct tumors.

To dissect the mechanism of action, we immunostained tumor cross-sections for an angiogenesis marker, von Willebrand factor (vWF). As shown in Fig. 5a, c, the L[C] group

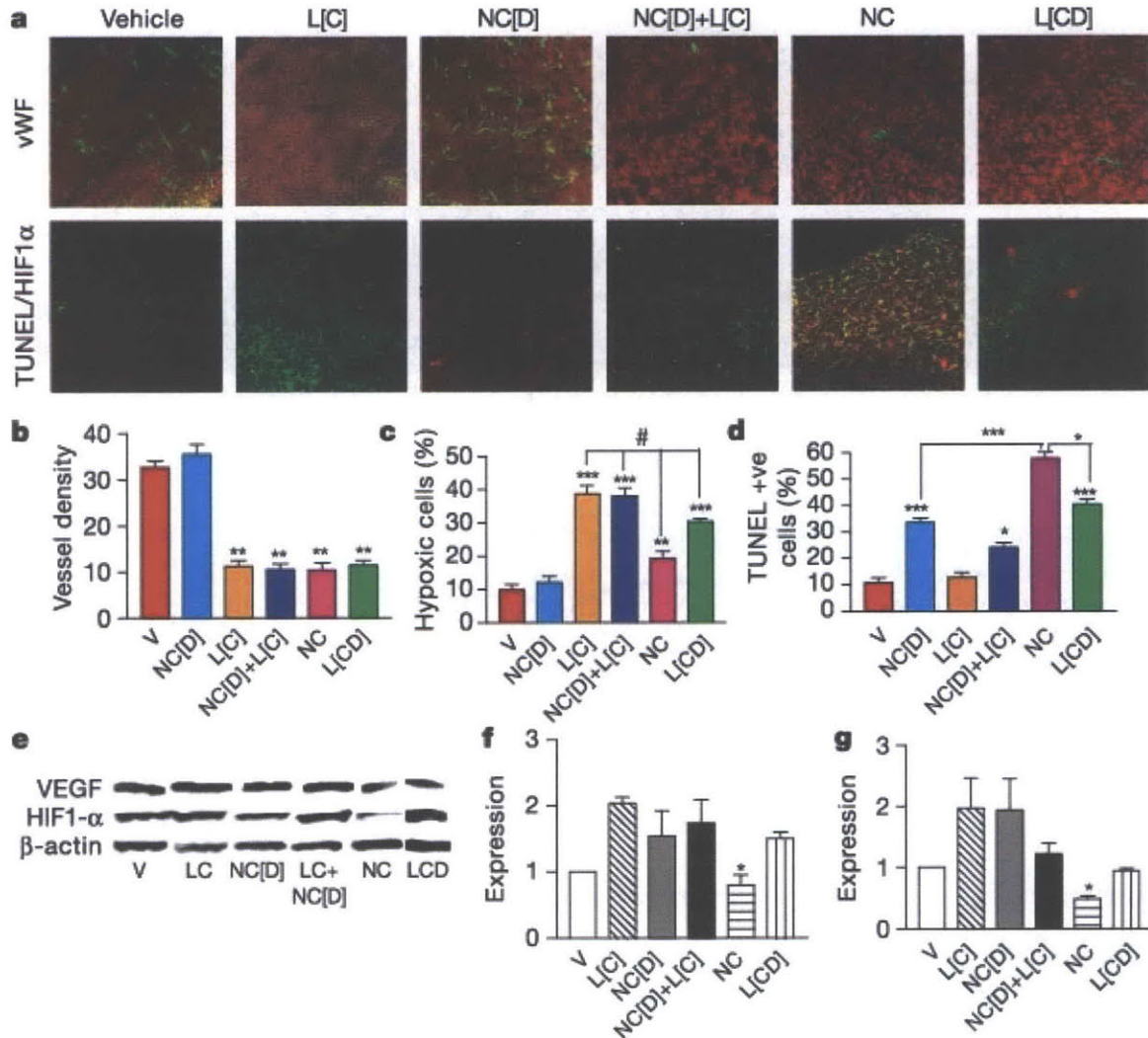


**Figure 5: Effect of nanocell treatment on tumor vasculature and apoptosis.** a, Top: cross-section of tumors immunostained for vWF, an endothelial marker. Bottom: tumors TUNEL-labelled for apoptosis with the use of Texas red-labelled nucleotide, and co-stained with an anti-HIF1-alpha antibody labelled by FITC. b–d, Graphs showing tumor vessel density (b), hypoxia (c) and apoptosis (d). Results are means plusminus s.e.m. (n = 3). Asterisk, P < 0.05; two asterisks, P < 0.01; three asterisks, P < 0.001; all compared with controls (analysis of variance with Newman–Keul's post-hoc test). e, Western blots showing the effect of different treatments on the levels of HIF1-alpha and VEGF; f, g, Graphs of levels of HIF1-alpha (f) and VEGF (g), normalized to beta-actin; expression is shown relative to vehicle, normalized to 1. Results are means plusminus s.e.m. Asterisk, P < 0.05 compared with other combretastatin-treated groups.

induced a more than 50% loss in vasculature compared with PBS-treated controls. There was no difference in the vessel density between the groups treated with L[C], L[CD], NC and the NC[D] + L[C]. NC[D] had no effect on the tumor vasculature, indicating that 'metronomic' dose anti-angiogenesis was not the underlying cause for the enhanced efficacy observed with nanocells.

We next evaluated the tumors for apoptosis by using TdT-mediated dUTP nick end labeling (TUNEL) staining, staining the same sections simultaneously for HIF1- $\alpha$  expression. As shown in Fig. 5a, d, e, NC[D] treatment induced significant apoptosis in the tumor without any increase in the expression of HIF1- $\alpha$ . L[C] treatment did not induce apoptosis, nor did it potentiate the effect of NC[D] when both were injected together. A possible explanation for this observation could be attributed to the accumulation of HIF1- $\alpha$ , which can upregulate pro-survival growth factors<sup>7</sup>. In contrast, administration of NC significantly increased the percentage of TUNEL-positive cells in the tumor in comparison with NC[D] alone, and also disconnected the expressions of HIF1- $\alpha$  and vascular endothelial growth factor (VEGF) in comparison with other anti-angiogenesis-treated groups (Fig. 5e–g), possibly arising from a focal build-up of doxorubicin inside the tumor, leading to increased apoptosis.

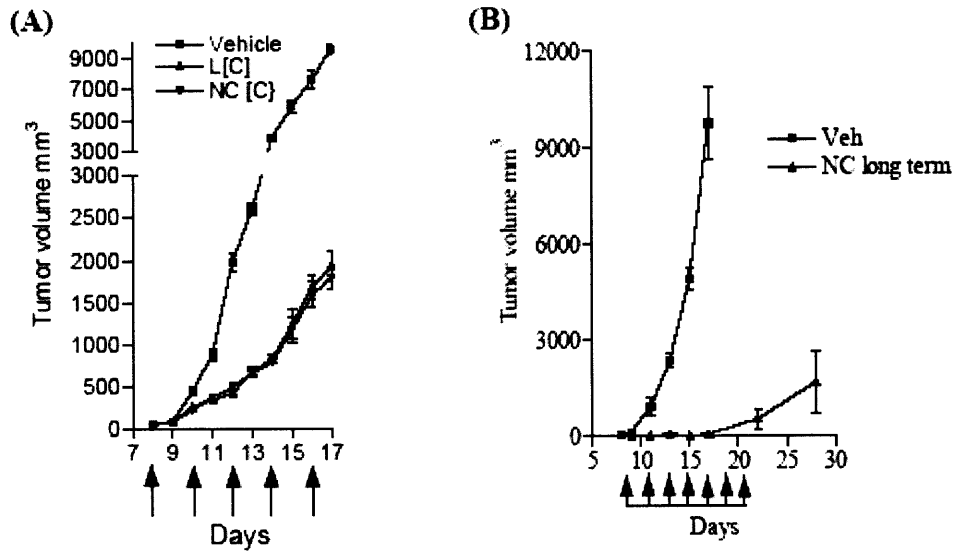
Analysis of the white blood cell count, which is highly susceptible to cytotoxic agents, showed that treatment with NC resulted in the least systemic toxicity (Fig. 4f), consistent with the intra-tumorally restricted release of the cytotoxic agent arising from the vascular shut-down. To confirm the enhanced uptake into the tumor, we fabricated nanocells with fluorescein and monitored the level of the dye in the tumor and other highly vascular organs. The nanocells were detected within 5 h in all the vascularized tissues in equilibrium with the levels in the blood, and preferential accumulation of the nanocells in the tumors was evident at 24 h, with a concomitant fall in the serum level (Supplementary Fig. 2). This selective uptake into the tumor could arise

from increased residence time in the circulation as a result of pegylation-induced reduction in immunogenicity<sup>17</sup>. Furthermore, the unique 'leakiness' of the tumor vessels, which, unlike physiological vasculature, have pores that are 400–600 nm in diameter<sup>18</sup>, enhances the permeability and retention of the nanocells fabricated in this study. Additionally, the anti-angiogenesis agent-induced decrease in hydrostatic pressure gradient across the vascular wall could explain the increased accumulation at 24 h compared with earlier time points<sup>19</sup>. Although further studies are needed to dissect out these effects, the reduced toxicity and enhanced anti-tumor anti-metastatic effects (Supplementary Fig. 3) emphasizes the advantages of the mechanism-based design of the system.

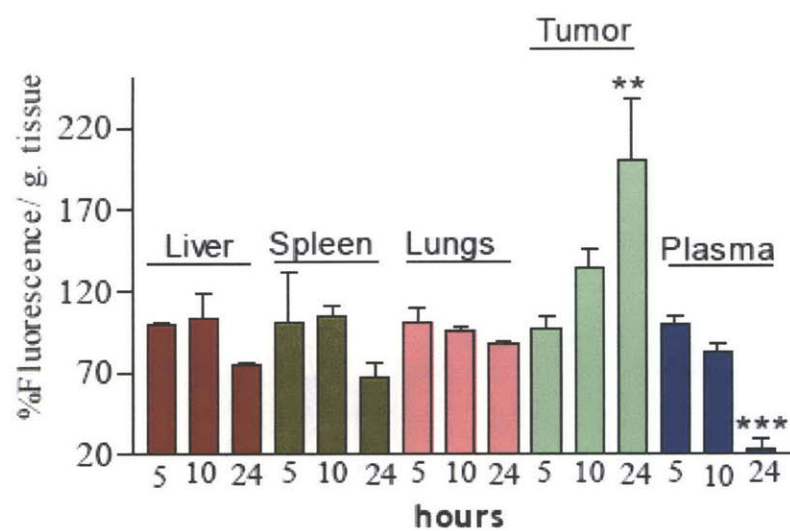
#### **2.1.4. Conclusions**

Several components of the nanocell approach can facilitate future therapy in humans. First, the nuclear arrangement of cytotoxic agent-conjugated nanoparticle and the encapsulation of the anti-angiogenesis agent in the surrounding phospholipid block-copolymer envelope enables temporal targeting of the tumor vasculature, resulting in the intra-tumoral trapping of the nanoparticles. Second, the resultant slow release and focal build-up of the cytotoxic agent within the tumor allows a prolonged exposure and an increase in the apoptotic potential, which can overcome hypoxia-induced reactive resistance. Third, although we show here a selective tumor uptake, we recognize that these vehicles can be further specifically targeted to tumor vasculature by using probes that recognize specific molecular signatures on the vasculature<sup>20</sup>. Thus, the nanocell concept enables a significant advance in cancer therapy over current approaches. This platform technology supports the paradigm shift from a 'reductive' to an 'integrative' approach in cancer therapy<sup>21</sup>.

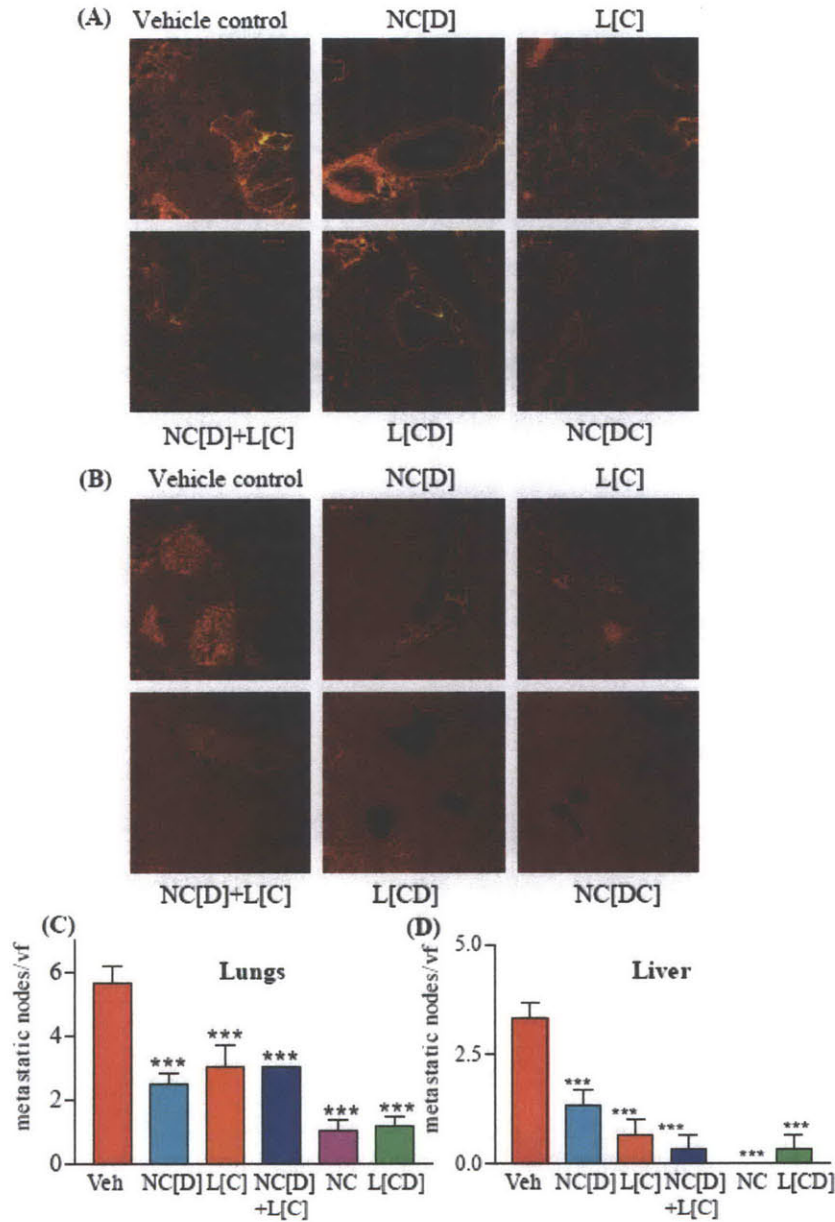




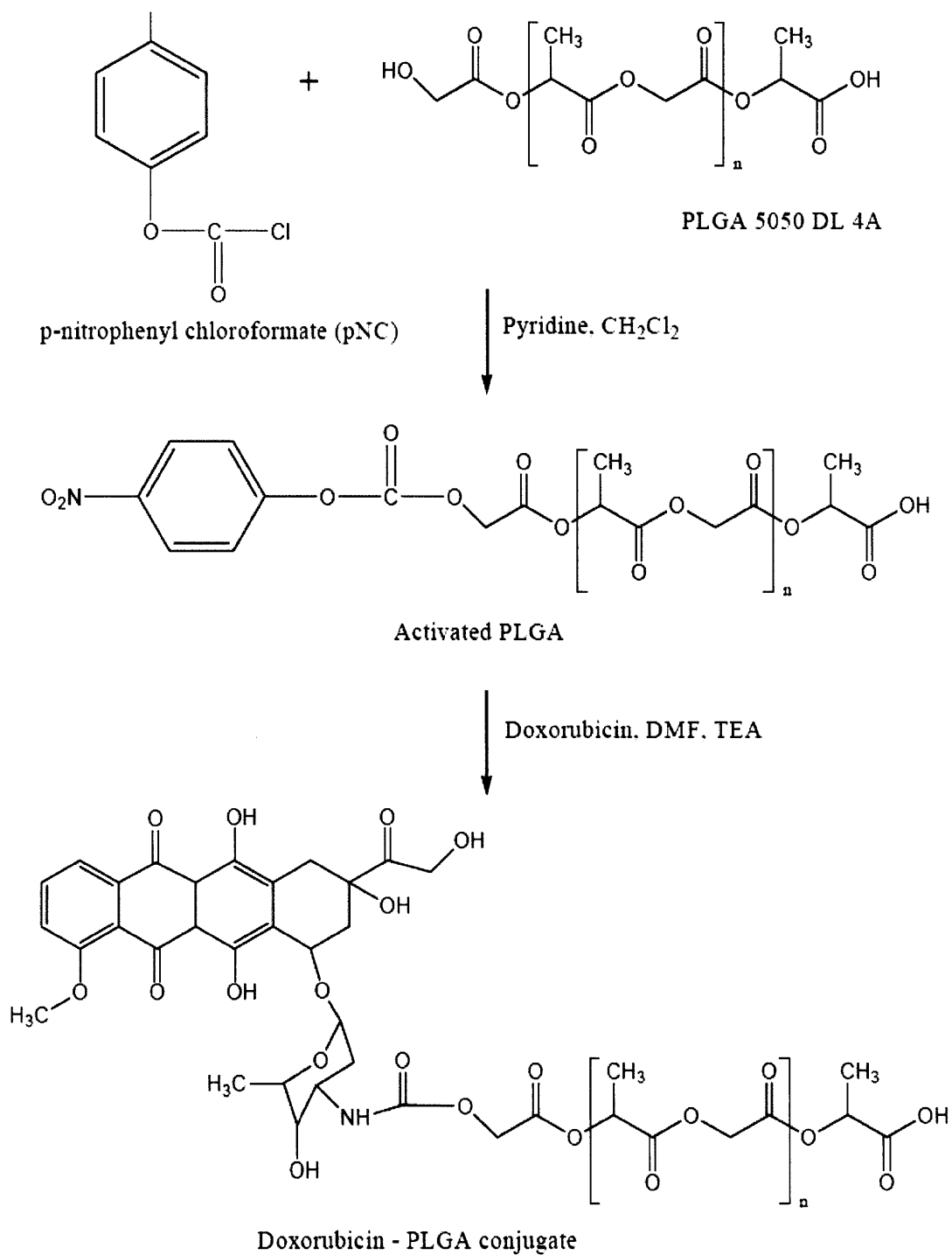
**Suppl. Figure 1. Effect of liposomal and nanocell combretastatin and long-term nanocell therapy on tumor growth.** (A) Graph shows the effect of liposomal combretastatin and nanocells (fabricated encapsulating only combretastatin and PLGA core) were administered to melanomabearing mice. Treatment was started when the tumors reached 50mm<sup>3</sup> in volume and continued every alternate day for five rounds of administration. The total combretastatin administered per injection in either formulation was 50 mg/kg. In another experiment, melanoma-bearin animals were treated with seven cycles of NC therapy once the tumors reached 50 mm<sup>3</sup> in volume. Control animals were treated with PBS vehicle, and were sacrificed on day 17 as the tumors became too big in size. In the long-term treated group, 50% of the animals showed almost complete regression of tumor over 28 days, and as shown in graph (B) the remaining animals had significantly smaller tumor volume as compared to the untreated animals.



**Suppl. Figure 2. Nanocell Biodistribution.** The graph shows the bio-distribution of nanocells fabricated with fluorescein dye, quantified over time by measuring the levels of the dye at 5, 10 and 24 hours. At 24 hours, a preferential accumulation of the nanocells in the carcinoma was evident in comparison to other vascularised tissues, with a concomitant fall of the levels in blood. All data are mean  $\pm$  SEM with n=3-5 per group.



**Suppl. Figure 3. Effect of nanocell therapy on metastasis of primary GFP+ melanoma to lungs and liver.** (A) Upper panel depicts a cross-section of same-level lung tissues from different treatment groups. (B) Panel shows the same level cross-sections of livers from different treatment groups. The organs were excised from animals treated with nanocells (NC), doxorubicin-conjugated nanoparticles NC[D], liposomal-combretastatin (L[C]), or co-injected with NC[D]+L[C], or doxorubicin and combretastatin encapsulated liposomes (L[CD]). Control groups were treated with saline. The tissues were fixed in 4% paraformaldehyde on ice, and stained with standard H&E. The images were captured using a Zeiss LSM510 confocal microscope. The fluorochromes were excited with 488 nm and 543 nm laser lines, and the images were captured using 505-530 BP and 565-615 BP filters at a 512×512 pixel resolution. The merge images shown here demonstrate distinct metastatic nodes, which appear yellow. The graph depicts the quantification of metastatic nodes in each view field. Data expressed are mean ± SEM from n=3. \*\*\*P<0.001 vs controls (ANOVA with Newman-Keul's Post Hoc test).



**Suppl. Figure 4. Doxorubicin to PLGA 5050 conjugation schematic.** Schematic showing the detailed synthetic steps involved in the conjugation of Doxorubicin to PLGA 5050.

## Supplementary Methods

### Conjugation of doxorubicin to PLGA.

Poly(lactic glycolic acid) (PLGA) (Medisorb® 5050 DL 4A), having a lactide / glycolide molar ratio of 50/50, was obtained from Alkermes (Wilmington, OH). The average molecular weight of this polymer is reported to be 61 kDa and it has free hydroxyl and carboxylic groups at its terminal ends. Doxorubicin hydrochloride, p-nitrophenyl chloroformate and triethylamine were obtained from Sigma-Aldrich (St. Louis, MO). Briefly, 1.5 g of PLGA 5050 DL 4A was dissolved in 15 ml of methylene chloride and activated by the addition of 14 mg of p-nitrophenyl chloroformate and 9.4 mg (~ 9.6  $\mu$ L) of pyridine to the solution, kept in an ice bath at 0 °C (stoichiometric molar ratio of PLGA: p-nitrophenyl chloroformate: pyridine = 1:2.8:4.7). The reaction was carried out for 3 hours at room temperature under nitrogen atmosphere. The resulting solution was diluted with methylene chloride and washed with 0.1 % HCl and brine solution. The organic phase was separated, dried on anhydrous magnesium sulfate, filtered, and then rotary-evaporated to yield activated PLGA polymer. Activated PLGA (0.4g) was dissolved in 3 mL of dimethylformamide (DMF) and reacted with 4 mg of doxorubicin and 2.7 mg (~ 4  $\mu$ L) of triethylamine for 24 hours at room temperature under nitrogen atmosphere (stoichiometric molar ratio of activated PLGA: doxorubicin: triethylamine = 1:1:4). The final conjugated product was precipitated by the addition of cold ether, washed with ether, filtered, and dried under vacuum. The detailed schematic of the synthetic process is elucidated in Supplementary Figure 4. The conjugation of doxorubicin to PLGA increased the loading efficiency from less than 1% (non-conjugated) to over 70%.

### **Synthesis and scanning electron microscopic analysis of the nanoparticles.**

Nanoparticles were formulated using an emulsion-solvent evaporation technique as described. Briefly, 50mg PLGA-DOX was allowed to dissolve completely in 2.5mL acetone for one hour at room temperature. At this time, 0.5mL methanol was added and the entire solution was emulsified into an aqueous solution of PVA (0.5 g / 25 mL) by slow injection with constant homogenization using a tissue homogenizer followed by one minute of sonication (Misonix, Farmingdale, NY). The emulsion was added to a dilute aqueous solution of PVA (0.2 g / 100 mL) with rapid mixing for 3 hours at room temperature to evaporate any residual acetone or methanol. Nanoparticle size fractions were recovered by ultracentrifugation at 10000, 25000 and 50000 ×g. Nanoparticles from the smallest size fractions were extruded through a 100nm membrane using a hand-held extruder (Avestin, Ottawa, ONT) to obtain nanoparticles for encapsulation within nanocells. The nanoparticles were sized by dynamic light scattering (Brookhaven Instruments Corp, Holtsville, NY) as well as by scanning electron microscopy (SEM). For SEM, the nanoparticles were dried for 72 hours, following which a small quantity was dusted onto a carbon grid and coated with gold. They were analyzed using a Jeol JSM5600 EM at a magnification of 3700X.

### **Synthesis of nanocells**

To prepare the lipid envelope of the nanocell, cholesterol (CHOL), eggphosphatidylcholine (PC), and distearoylphosphatidylethanolamine – polyethylene glycol (m.w. 2000) (DSPE-PEG) were obtained from Avanti Polar Lipids (Birmingham, AL). Combretastatin A4 was obtained from Tocris Cookson (Ellisville, MO). All other reagents and solvents were of analytical grade. PC:CHOL:DSPE-PEG (2:1:0.2 molar) lipid membranes were

prepared by dissolving 27.5mg lipid in 2 mL chloroform in a round bottom flask. Combretastatin A4 (12.5 mg) was co-dissolved in the chloroform mixture at a 0.9:1 drug:lipid molar ratio. Chloroform was evaporated using a rotoevaporator to create a monolayer lipid/drug film. This film was resuspended in 1 mL H<sub>2</sub>O after one hour of shaking at 65 °C to enable preferential encapsulation of combretastatin A4 within the lipid bilayer. When synthesizing nanocells, nanoparticles containing 250µg doxorubicin were added to the aqueous lipid resuspension buffer. The resulting suspension was extruded through a 200 nm membrane at 65 °C using a hand held extruder (Avestin, Ottawa, ONT) to create the lipid vesicles. The average vesicle size was determined by dynamic light scattering (Brookhaven Instruments Corp, Holtsville, NY).

### **Transmission electron micrographs**

The nanocells were fixed in 2.5% gluteraldehyde, 3% paraformaldehyde with 5% sucrose in 0.1M sodium cacodylate buffer (pH 7.4), embedded in low temperature agarose and post fixed in 1% OsO<sub>4</sub> in veronal-acetate buffer. The sample was stained in block overnight with 0.5% uranyl acetate in veronal-acetate buffer (pH6.0); then dehydrated and embedded in epon-812 resin. Sections were cut on a Leica ultra cut UCT at a thickness of 70nm using a diamond knife, stained with 2.0% uranyl acetate followed by 0.1% lead citrate and examined using a Philips EM410.

### **Physicochemical release kinetics studies**

Concentrated drug-loaded nanocells were suspended in 1 ml of PBS or hypoxic cell lysate buffer, and sealed in a dialysis bag (M.W. cutoff: 10,000, Spectrapor). The dialysis bag was incubated in 20 ml of PBS buffer at 37C with gentle shaking. 200 ul aliquots were taken from the incubation medium at predetermined time intervals and stored frozen for analysis.

Released drug was quantified by reverse phase HPLC using a C18 column (4.5 mm X 150 mm, Waters) with acetonitrile (A) and water (B) as eluents. Starting conditions were 80% A and 20% B with a linear gradient over 15 min to 10% A and 90% B, a linear gradient over five minutes to 0% A and 100% B, and a linear gradient over 5 min returning to the start conditions with a flow rate of 1 ml/min. A standardized amount of dexamethasone was added as an internal control for absolute quantification of combretastatin A4 and doxorubicin. Combretastatin A4 and dexamethasone were detected by wavelength monitoring at 295 nm and doxorubicin was detected by wavelength monitoring at 480 nm. The amount of free doxorubicin released is small as compared to the doxorubicin-PLGA fragments, emphasizing that free doxorubicin and the active doxorubicin-PLGA fragments, and not doxorubicin-PLGA oligomers, contribute to the cytotoxic effect.

### **In vitro co-culture assay**

To dissect out the anti-angiogenesis actions from the anti-tumor activity, we developed a co-culture assay mimicking the tumor milieu. B16/F10 melanoma cells were transfected to express green fluorescent protein (GFP), and selected under puromycin pressure. Colonies (GFP-BL6/F10) were confirmed to express GFP using epifluorescence microscope and fluorescence activated cell sorting, and cultured in MEM-a medium supplemented with 10% fetal bovine serum. Since isolating primary tumor endothelial cells entails practical difficulties, we used human umbilical vein endothelial cells, which are widely used in angiogenesis studies. Human umbilical vein endothelial cells (Cambrex, pooled cells from 3 donors) were cultured in EBM media (Clonetics) supplemented with bullet kit (Clonetics) and 20 % FBS. For the co-culture assay, growth factor reduced Matrigel (extracellular matrix from EHS carcinoma) was plated on glass coverslips, and allowed to gel at 37 degree Celsius. HUVECs were trypsinised and plated



on the Matrigel at a density of 30000 cells per coverslip/well of a 12 well plate, and allowed to form tube-like structures over a period of 24 hours. At this time point, GFP-BL6/F10 cells were added to each well at a density of 10,000 cells/well. The co-culture was allowed to develop for a further 24 hours, following which the appropriate treatments were started. At the end of defined periods of incubation, the cells were fixed with 4% paraformaldehyde on ice, and incubated with propidium iodide to label the nuclei. The coverslips were washed with phosphate buffer saline, and analysed using a Leica LSM510 confocal microscope. Images were captured randomly from four sectors. The fluorochromes were excited with 488 nm and 543 nm laser lines, and the images were captured using 505-530 BP and 565-615 BP filters at a 512×512 pixel resolution. Merge images were created by combining images from both the filters, where the melanoma cells fluoresced yellow while the endothelial cells were red. Quantification of the area covered by endothelial cells or GFP-BL6/F10 cells was carried out using a planimetric point-count method using a 224-intersection point square reticulum. Data were expressed as the ratio of each component to the total area covered by cells.

### **In vivo tumor model**

Male C57/BL6 mice (20 g) were injected with  $3 \times 10^5$  GFP-BL6/F10 or  $2.5 \times 10^5$  Lewis lung carcinoma cells into the flanks. The growth of the tumors was monitored regularly. The mice were randomized into different treatment groups when the tumor reached 50mm<sup>3</sup> in volume. Each formulation, nanocell or simple liposomes, was prepared, quantified, and diluted such that 100µl of administration was equivalent to 50 mg/kg and 500µg/kg of combretastatin and doxorubicin respectively. The rationale to encapsulate the doxorubicin-nanoparticle within the lipids to generate the NC[D] group was to remove any sizing bias, and also to maintain the uniformity in pegylation between groups, such that the pharmacokinetic profile remained

unaltered. We used L[C] as a control group as a simple liposomal formulation of combretastatin could later be translated into clinical applications. Furthermore, a comparison of the liposomal combretastatin (L[C]) and nanocells with only combretastatin (NC[C]) demonstrated that both the treatment groups exerted similar effects on tumor inhibition (Supplementary Figure 1A), indicating that alone the PLGA-core of the nanocell was inactive. The animals were injected every alternate day after the tumors reached the desired size. The animals were sacrificed on day 17, and the tumors were excised for histopathology. Simultaneously, 1 ml of blood was drawn through cardiac puncture, and analyzed for toxicity profile of the treatment regimens.

### **Immunohistochemistry for tumor vasculature**

Tumor samples were embedded in TissueTek and snap frozen on dry ice. Thin cryosections (10  $\mu\text{m}$ ) were made using a Reichart cryostat, and fixed in methanol. The sections were then permeabilised in Tris buffer saline with Triton X and Tween, and blocked with 1% goat serum. The sections were probed overnight with a rabbit primary antibody against vonWillebrand factor (Dako, 1 in 2000 dilution), an endothelial cell marker. The staining for vWF was found to be consistent with the expression of other endothelial markers such as VE-cadherin and Tie-2 (data not shown). The sections were washed and re-probed with a goat secondary antibody coupled to Texas Red. The sections were coated with slowfade (Molecular probes), and imaged using a Leica LSM510 confocal microscope. Images were captured randomly from three areas per section. The fluorochromes were excited with 488 nm and 543 nm laser lines, and the images were captured using 505-530 BP and 565-615 BP filters at a 512 $\times$ 512 pixel resolution. Vessel density was quantified using stereological approaches, using a planimetric point-count method using a 224-intersection point square reticulum.

### **Quantifying apoptosis and HIF1 $\alpha$ in the tumor sections**

Tumor cryosections were prepared as described above. The sections were processed for TUNEL staining using Texas red labeled nucleotide as per the manufacturer's instruction (Roche). The sections were then permeabilised in Tris buffer saline with Triton X and Tween, and blocked with 1% goat serum. The sections were probed overnight with a primary antibody against HIF1 $\alpha$ . The sections were washed and re-probed with a goat secondary antibody coupled to FITC. The sections were coated with slowfade (Molecular probes), and imaged using a Leica LSM510 confocal microscope. The sections were coated with slowfade (Molecular probes), and imaged using a Leica LSM510 confocal microscope. Images were captured randomly from three areas per section. The fluorochromes were excited with 488 nm and 543 nm laser lines, and the images were captured using 505-530 BP and 565-615 BP filters at a 512 $\times$ 512 pixel resolution. Apoptosis and hypoxia was quantified using stereological approaches, using a planimetric point-count method using a 224-intersection point square reticulum.

### **Analysis of metastatic nodes**

Since melanoma has the potential to metastasize to the lungs and the liver, we evaluated the effect of different treatments on pulmonary and hepatic metastatic potential of the primary tumor. In contrast to control mice, treatment with nanocells displayed little or no visible tumor metastasis, achieving a significantly superior outcome than other treatment group (Supplementary Figure 3). A possible explanation for this behavior is that the prolonged exposure to the cytotoxic agent following the vascular collapse resulted in an overall decrease in the expression of HIF1 $\alpha$  and related growth factors (Figure. 4) These organs were harvested from the animals during necropsy, and fixed in 10% formaldehyde. The tissues were then

paraffin embedded, and thin section slides were prepared for H&E staining. The slides were imaged with a Leica LSM510 confocal microscope. The fluorochromes were excited with 488 nm and 543 nm laser lines, and the images were captured using 505-530 BP and 565-615 BP filters at a 512×512 pixel resolution. Metastatic nodes were quantified by counting the number of yellow foci per section in the merged image.

### **2.1.5. References**

1. Kerbel, R. S. & Kamen, B. A. The anti-angiogenic basis of metronomic chemotherapy. *Nature Rev. Cancer* 4, 423–436 (2004)
2. Semenza, G. L. Surviving ischemia: adaptive responses mediated by hypoxia-inducible factor 1. *J. Clin. Invest.* 106, 809–812 (2000)
3. Tran, J. et al. A role for survivin in chemoresistance of endothelial cells mediated by VEGF. *Proc. Natl Acad. Sci. USA* 99, 4349–4354 (2002)
4. Yu, J. L., Rak, J. W., Coomber, B. L., Hicklin, D. J. & Kerbel, R. S. Effect of p53 status on tumor response to antiangiogenic therapy. *Science* 295, 1526–1528 (2002)
5. Blagosklonny, M. V. Antiangiogenic therapy and tumor progression. *Cancer Cell* 5, 13–17 (2004)
6. Pennacchietti, S. et al. Hypoxia promotes invasive growth by transcriptional activation of the met protooncogene. *Cancer Cell* 3, 347–361 (2003)
7. Rofstad, E. K. et al. Hypoxia promotes lymph node metastasis in human melanoma xenografts by up-regulating the urokinase-type plasminogen activator receptor. *Cancer Res.* 62, 1847–1853 (2002)
8. Kieran, M. W., Folkman, J. & Heymach, J. Angiogenesis inhibitors and hypoxia. *Nature Med.* 9, 1104 (2003)

9. Kerbel, R. & Folkman, J. Clinical translation of angiogenesis inhibitors. *Nature Rev. Cancer* 2, 727–739 (2002)
10. Chabner, B. A., et al. Goodman and Gilman's *The Pharmacological Basis of Therapeutics* 9th edn (McGraw-Hill, 1996)
11. Tozer, G. M., Kanthou, C., Parkins, C. S. & Hill, S. A. The biology of the combretastatins as tumor vascular targeting agents. *Int. J. Exp. Pathol.* 83, 21–38 (2002)
12. Miklos, A. G., Lyman, M. D., Freed, L. E. & Langer, R. Wetting of poly(L-lactic acid) and poly(D-lactic-co-glycolic acid) foams for tissue culture. *Biomaterials* 15, 55–58 (1994)
13. Yoo, H. S., Oh, J. E., Lee, K. H. & Park, T. G. Biodegradable nanoparticles containing doxorubicin-PLGA conjugate for sustained release. *Pharm. Res.* 16, 1114–1118 (1999)
14. Sengupta, S., Kiziltepe, T. & Sasisekharan, R. A dual-colour fluorescence imaging-based system for the dissection of antiangiogenic and chemotherapeutic activity of molecules. *FASEB J.* 18, 1565–1567 (2004)
15. Jain, R. K. Normalizing tumor vasculature with anti-angiogenic therapy: a new paradigm for combination therapy. *Nature Med.* 7, 987–989 (2001)
16. Hanahan, D., Bergers, G. & Bergsland, E. Less is more, regularly: metronomic dosing of cytotoxic drugs can target tumor angiogenesis in mice. *J. Clin. Invest.* 105, 1045–1047 (2000)
17. Allen, T. M. Ligand-targeted therapeutics in anticancer therapy. *Nature Rev. Drug Discov.* 2, 750–763 (2002)
18. Yuan, F. et al. Vascular permeability in a human tumor xenograft: molecular size dependence and cutoff size. *Cancer Res.* 55, 3752–3756 (1995)
19. Tong, R. T. et al. Vascular normalization by vascular endothelial growth factor receptor-2 blockade induces a pressure gradient across the vasculature and improves drug penetration in tumors. *Cancer Res.* 64, 3731–3736 (2004)
20. Arap, W. et al. Steps toward mapping the human vasculature by phage display. *Nature Med.* 8, 121–127 (2002)

21. Hanahan, D. & Weinberg, R. A. The hallmarks of cancer. *Cell* 100, 57–70 (2000)

## 2.2. Lipid-Encapsulated Quantum Dots Distinguish Tumor and Normal Vasculature

### 2.2.1. Introduction

As tumors undergo rapid growth, they must generate their own vascular network in order to provide the nutrients necessary for continued expansion and spread. *In vivo* imaging of tumor vascularization is now of paramount importance, as this is both a sign of increasing tumor malignancy and a potential target for new therapies. We demonstrate here a method for imaging and specifically identifying tumor-specific vasculature using quantum dots encapsulated within sterically stabilized liposomes, combining the fluorescent properties of quantum dots with the bioavailability and tumor-specific interstitial uptake of the liposomal vehicle.

Quantum dots have emerged as a powerful alternative tool for fluorescence imaging due to a unique set of physiochemical properties that surpass those of fluorescent dyes in many biomedical applications. These include a narrow fluorescent emission under a broad set of absorption spectra (thus allowing the detection of multiple quantum dots with a single absorption wavelength), improved resistance to photobleaching and chemical degradation, and the availability of quantum dots to a multitude of chemical conjugation and capping strategies<sup>1</sup>.

Fluorescent labeling with quantum dots has successfully enabled measuring the ability of particles to access the tumor microenvironment<sup>2</sup>, tracking of cancer cells undergoing metastasis<sup>3</sup>, *in vivo* imaging of capillary structures hundreds of micrometers beneath the skin<sup>4</sup>, as well as a multitude of additional successful biomedical applications. Quantum dots are particularly well suited for *in vivo* applications as they may remain fluorescent in tissue structures for at least four months<sup>5</sup>, and their large two-photon cross-sectional efficiency allows high resolution intravital microscopy of deep tissue structures at the subcellular level<sup>6</sup>.

## **2.2.2. Materials and Methods**

### **Liposome preparation**

1,2-Distearoyl-sn-Glycero-3-Phosphocholine (DSPC), 1,2-Distearoyl-sn-Glycero-3-Phosphoethanolamine-N-[Methoxy(Polyethylene glycol)-2000] (DSPE-PEG2000) and Cholesterol (CHOL) were obtained from Avanti Polar Lipids (Alabaster, Al). A lipid mixture consisting of DSPC:CHOL:PEG-DSPE (2:1:0.2 molar ratio) was prepared by dissolving the lipids in chloroform in a round-bottomed flask (10  $\mu$ mol total lipid). The solution was frozen in liquid nitrogen for 3 min and lyophilized overnight. Quantum dot loaded liposomes were prepared by hydrating the lyophilized lipid mixtures with 0.3  $\mu$ M Amino-PEGylated, derivatized-polyacrylic acid coated cadmium selenide/zinc sulfide core/shell quantum dots (Quantum Dot Corporation, Hayward CA) and 1 ml of buffer solution 10 mM Tris-HCl with 150 mM NaCl at pH 7.4 via five freeze-thaw vortex cycles. These multilamellar liposomes were then extruded 10 times through 0.1  $\mu$ m polycarbonate membranes filters at 50  $^{\circ}$ C to produce large unilamellar liposomes. Untrapped quantum dots were removed from the liposome suspension by passing it through a Sephadex G-50 column equilibrated with a 150 mM NaCl solution.

### **Electron microscopy**

Sample was negatively stained by absorbing material on a formvar/ carbon coated nickel grid. Grid was washed with 2% Uranyl Acetate and dried. Images were taken on a Philips EM410 transmission electron microscope.



### **Localization of quantum dots in vivo.**

Male C57/BL6 mice (20g) were injected with  $2.5 \times 10^5$  Lewis lung carcinoma cells into the flanks. The growth of tumors was monitored regularly. Encapsulated quantum dots were injected into Lewis lung carcinoma-bearing mice. Cross sections of tissues (30 mm) harvested at 10 and 24 h post-treatment were immunostained for vWF to delineate the blood vessels. Images were captured using a LSM510 confocal microscope, with excitation at 488 nm and emission for FITC (vWF) and Rhodamine (Qdots). 3D reconstruction of the tissue sections was also performed to show depth-coding intensity for vWF and quantum dots.

### **2.2.3. Results and Discussion**

Quantum dots have previously been employed as labels for normal and neoplastic blood vessels utilizing synthesis and targeting protocols designed for efficient internalization within the vascular structures<sup>2, 4</sup>. We explored here an alternate approach to targeting tumor vasculature, using a macromolecular liposome-based carrier in order to reach the appropriate size that maximizes extravasation through porous tumor vasculature and restricts nonspecific passage through healthy vasculature or significant uptake by non-tumor bearing tissue<sup>7, 8</sup>. We investigated whether the “leakage” of quantum dot fluorescence into the tumor interstitium would provide an effective platform for not only imaging angiogenic vessels, but also for readily distinguishing tumor-specific and normal vasculature *in vivo*.

Tumor-specific vasculature exhibits marked structural abnormalities compared to normal vasculature including increased tortuosity, excessive branching, and aberrant basement membrane formation. Tumor vasculature also has a high vascular permeability, or porosity. This porosity is a result of the presence of numerous ‘openings’ as large as 600 nm (including

endothelial fenestrae and transcellular holes) in the vascular wall which permit the passage of nanoscale particles from the bloodstream into the tumor interstitium. This porosity in combination with decreased tumor lymphatic drainage enables significantly increased tumor uptake and retention (the EPR effect) of agents associated with macromolecular delivery vehicles<sup>9</sup>.

The extent of tumor vascularization is further correlated with metastatic potential, tumor drug efficacy, and overall patient survival<sup>10</sup>, making an effective means of identifying and imaging angiogenic vessels critical both as a diagnostic and therapeutic tool. A number of different modalities are currently being assessed for imaging angiogenic vessels, including magnetic resonance imaging, computed tomography, ultrasound, and positive emission tomography based protocols<sup>11</sup>. Additionally there are a number of fluorescence-microscopy based techniques for imaging angiogenesis including the use of fluorescent liposomes, dextrans, nanospheres, and viral nanoparticles<sup>12</sup>. These fluorescent approaches are particularly advantageous as they do not rely on the use of specialized medical imaging equipment not readily accessible in many research laboratories.

We encapsulated hydrophilic quantum dots within large unilamellar sterically stabilized liposomes (Fig.1). The utility of this delivery system was tested in Lewis lung carcinoma bearing mice. Spleen, lung, liver, and tumor samples were harvested from these animals at various time posts post intravenous injection of the quantum dot formulations(Fig.2D). Confocal imaging of the tissue sections indicates that quantum dots were spatially restricted within the vasculature in physiologically normal tissues (lungs, liver and spleen) at 24 hours. In contrast significant extravasation into the tumor interstitium was observed at the same time point, which was confirmed with 3D confocal-reconstruction of the tissue sections (Figure 2).

Previous methods for delivering quantum dots *in vivo* have included surface functionalization with water soluble ligands or silanization<sup>13</sup>. Block-copolymer micelles and lipid nanoparticles have also been successfully used as delivery vehicles for *in vivo* imaging<sup>14, 15</sup>. A recent study explored tumor uptake of quantum dots entrapped in a ~100nm lipid nanoparticle after i.p. administration<sup>16</sup>. In contrast to these studies, here we capitalized on the size and the propensity of sterically-stabilized liposomes to use the EPR effect for homing specifically to the tumor after i.v. administration. This is consistent with extensive reports that have demonstrated that sterically stabilized liposomes greater than 100 nm in size preferentially accumulate within the tumor interstitium. Delivering quantum dots *in vivo* via liposomal encapsulation is particularly advantageous as these vehicles are well suited for delivering both hydrophilic and hydrophobic particles<sup>7, 17</sup>. Further, we have shown previously that the delivery of multiple agents from multi-compartmental lipid vesicles in a spatial-temporal manner can result in a significantly enhanced therapeutic effect<sup>18</sup>. These vehicles may then be suitable for delivering a combination of fluorescent quantum dots for imaging tumor angiogenesis with anti-cancer therapeutic agents for treating the neoplasm.

#### **2.2.4. Conclusion**

The cytotoxicity of quantum dots in clinical practice is still under investigation, and conclusions are complicated by the variety of published synthesis and functionalization protocols<sup>13</sup>. Most studies thus far do not report adverse effects on cell function or development over the short term, though long-term cytotoxic studies are needed before definitive conclusions can be drawn. Liposomal delivery vehicles prevent the need for additional potentially cytotoxic quantum dot synthesis regimens necessary for bioavailability or targeting. The ability to load

multiple quantum dots per targeting vehicle also enables better control over the concentration of quantum dots at the target site.

In conclusion, we present here the first study demonstrating the use of sterically stabilized liposome- encapsulated fluorescent quantum dots for distinguishing normal and neoplastic vasculature. The clear delineation between the spatial distribution of these formulations between tumor and normal vasculature creates the exciting opportunity to harness this approach in detection of solid tumors.

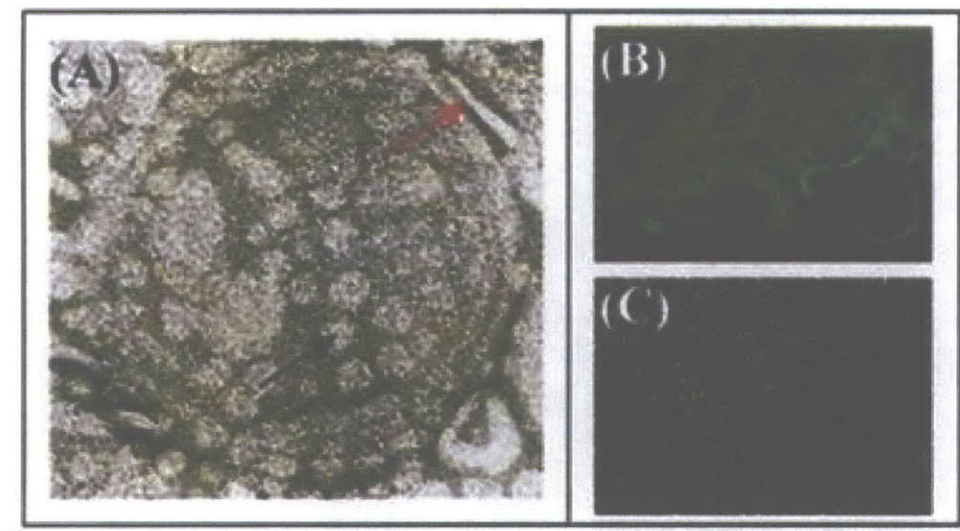


**Figure 1. Imaging of Angiogenic Vasculature.** A. A Transmission electron micrograph depicting a nanoscale (~100 nm) sterically-stabilized liposome entrapping quantum dots. The red arrow outlines the lipid coat. Sample was negatively stained by absorbing material on a formvar/carbon coated nickel grid, stained with uranyl acetate, and imaged using a Philips EM410. B and C. Confocal images of cross sections of lungs and liver respectively from mouse that were injected with pegylated quantum dots without the liposomal entrapment, which clearly shows that the fluorescence signal from the QDs are widely distributed in both the tissues.

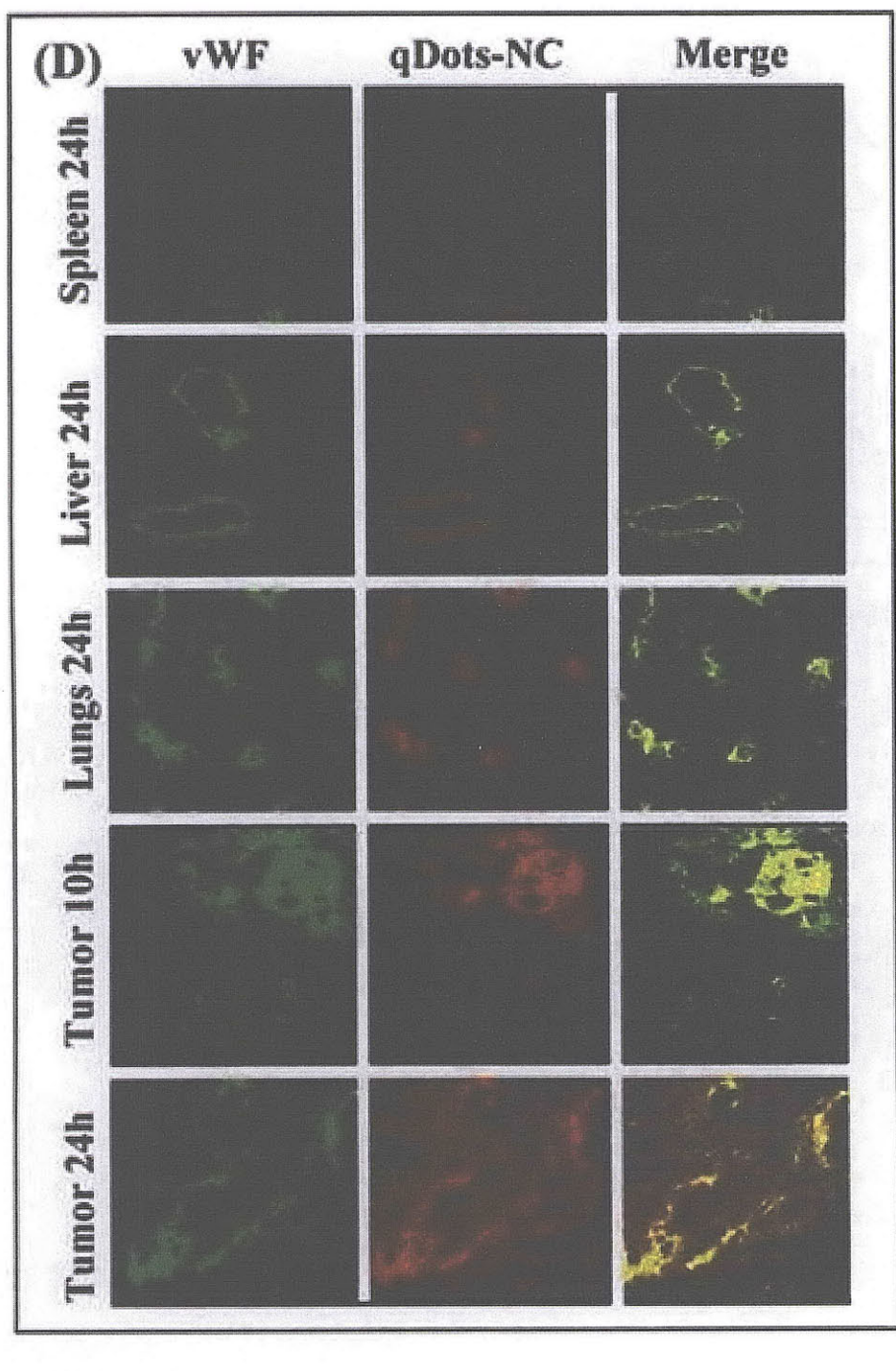


**Figure 1. Imaging of Angiogenic Vasculature.** D. Confocal micrographs of tissue cross sections harvested from tumor-bearing mice at 10 and 24 h post-injection with liposome-entrapped QDs. The sections were immunostained for von Willebrand Factor (vWF) to delineate vasculature. Images were captured using a Zeiss LSM510 Confocal microscope at 512×512 pixel resolution. The sections were excited with a 488nm laser, and emission was absorbed at FITC (vWF) and Rhodamine (QD) wavelengths. The signals from the vasculature and the QDs were merged to study the spatial distribution of the quantum dots with respect to normal and tumor vasculature.

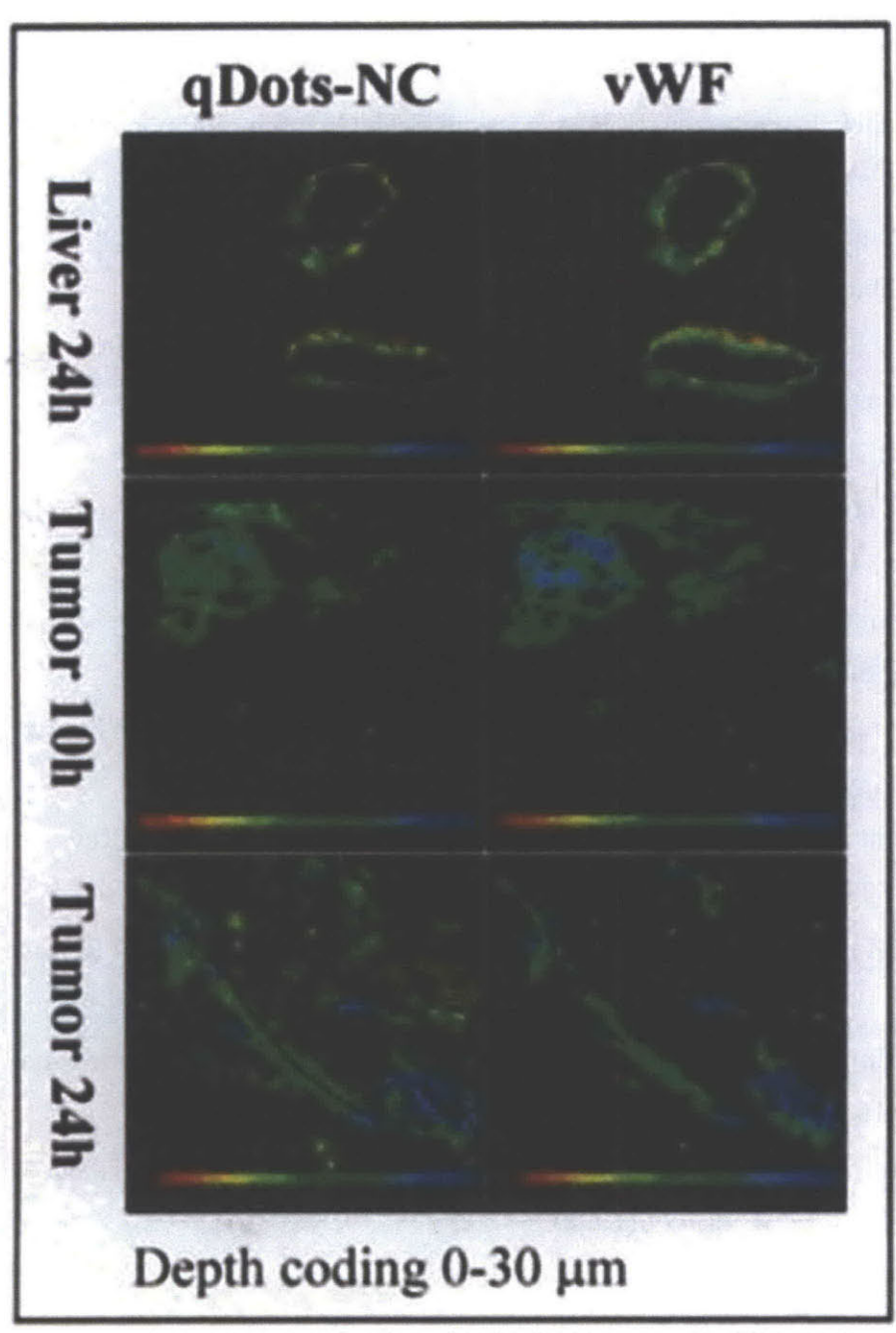


**Figure 2. 3-D Depth Coding.** The confocal sections through the liver and tumor tissues were merged in a 3D reconstruction to create depth-coding of intensity for vWF and quantum dots within the excised tissue sections. The liposome-entrapped QDs were found to be spatially restricted within normal vasculature but extravasate out from the tumor vasculature at 24h.

### 2.2.5. References

1. Medintz, I. L., Uyeda, H. T., Goldman, E. R. & Mattoussi, H. Quantum dot bioconjugates for imaging, labelling and sensing. *Nat Mater* 4, 435-46 (2005).
2. Stroh, M. et al. Quantum dots spectrally distinguish multiple species within the tumor milieu in vivo. *Nat Med* 11, 678-82 (2005).
3. Voura, E. B., Jaiswal, J. K., Mattoussi, H. & Simon, S. M. Tracking metastatic tumor cell extravasation with quantum dot nanocrystals and fluorescence emission-scanning microscopy. *Nat Med* 10, 993-8 (2004).
4. Larson, D. R. et al. Water-soluble quantum dots for multiphoton fluorescence imaging in vivo. *Science* 300, 1434-6 (2003).
5. Ballou, B., Lagerholm, B. C., Ernst, L. A., Bruchez, M. P. & Waggoner, A. S. Noninvasive imaging of quantum dots in mice. *Bioconjug Chem* 15, 79-86 (2004).
6. Levene, M. J., Dombeck, D. A., Kasischke, K. A., Molloy, R. P. & Webb, W. W. In vivo multiphoton microscopy of deep brain tissue. *J Neurophysiol* 91, 1908-12 (2004).
7. Torchilin, V. P. Recent advances with liposomes as pharmaceutical carriers. *Nat Rev Drug Discov* 4, 145-60 (2005).
8. Jain, R. K. Delivery of molecular and cellular medicine to solid tumors. *J Control Release* 53, 49-67 (1998).
9. Cuenca, A. G. et al. Emerging implications of nanotechnology on cancer diagnostics and therapeutics. *Cancer* 107, 459-66 (2006).
10. Weidner, N. Tumoural vascularity as a prognostic factor in cancer patients: the evidence continues to grow. *J Pathol* 184, 119-22 (1998).
11. Atri, M. New technologies and directed agents for applications of cancer imaging. *J Clin Oncol* 24, 3299-308 (2006).
12. Lewis, J. D. et al. Viral nanoparticles as tools for intravital vascular imaging. *Nat Med* 12, 354-60 (2006).
13. Michalet, X. et al. Quantum dots for live cells, in vivo imaging, and diagnostics. *Science* 307, 538-44 (2005).
14. Dubertret, B. et al. In vivo imaging of quantum dots encapsulated in phospholipid micelles. *Science* 298, 1759-62 (2002).



15. Liu, W. et al. Preparation and characterization of novel fluorescent nanocomposite particles: CdSe/ZnS core-shell quantum dots loaded solid lipid nanoparticles. *J Biomed Mater Res A* (2007).
16. Schroeder, J. E., Shweky, I., Shmeeda, H., Banin, U. & Gabizon, A. Folate-mediated tumor cell uptake of quantum dots entrapped in lipid nanoparticles. *J Control Release* 124, 28-34 (2007).
17. Gopalakrishnan, G. et al. Multifunctional lipid/quantum dot hybrid nanocontainers for controlled targeting of live cells. *Angew Chem Int Ed Engl* 45, 5478-83 (2006).
18. Sengupta, S. et al. Temporal targeting of tumour cells and neovasculature with a nanoscale delivery system. *Nature* 436, 568-72 (2005).
19. Cascone, M. G., Pot, P. M., Lazzeri, L. & Zhu, Z. Release of dexamethasone from PLGA nanoparticles entrapped into dextran/poly(vinyl alcohol) hydrogels. *J Mater Sci Mater Med* 13, 265-9 (2002).
20. Panyam, J., Williams, D., Dash, A., Leslie-Pelecky, D. & Labhasetwar, V. Solid-state solubility influences encapsulation and release of hydrophobic drugs from PLGA/PLA nanoparticles. *J Pharm Sci* 93, 1804-14 (2004).

## **2.3. A voxel-based Monte Carlo Model of Drug Release From Bulk Eroding Nanoparticles**

### **2.3.1. Introduction**

The use of polymeric nanoparticles as drug delivery devices is becoming increasingly prevalent in a variety of therapeutic applications. Despite their widespread clinical use, the factors influencing the release profiles of nanoparticle-encapsulated drugs are still not quantitatively understood. We present here a new, semi-empirical model of drug release from polymeric nanoparticles using a formulation of dexamethasone encapsulated within poly(lactic-co-glycolic acid) PLGA to set model parameters. We introduce a three-dimensional voxel-based framework for Monte Carlo simulations that enables direct investigation of the entire spherical nanoparticle during particle degradation and drug release. Due to implementation of this model at the nanoscale, we utilize assumptions that simplify the model while still allowing multi-phase drug release to be simulated with good correlation to experimental results. In the future, emerging mechanistic understandings of nanoparticle drug release may be integrated into this simulation framework to increase predictive power.

The shift from micro- to nano- scale drug delivery systems in recent decades has been driven by improvements in polymer formulation technology and evidence that medical applications such as chemotherapy are significantly enhanced by the use of nanoscale delivery vehicles<sup>1,2,3,4</sup>. Because drug release profiles differ based on the polymer, drug, and design parameters, the availability of computational models to understand and predict drug release is valuable for the extension and optimization of existing drug delivery technologies.

Several models have been reported in the literature to describe drug release and particle breakdown for polymer-based delivery vehicles<sup>5,6,7,8</sup>. It is clear from these studies that the

number of factors influencing drug release is too unwieldy for a single model to incorporate. Such factors include water and drug diffusion, drug dissolution, polymer molecular weight, particle size and geometry, polymer degradation, micro-environment pH changes, autocatalysis, polymer swelling, and more<sup>9,10,11</sup>. Incorporation of these factors is further complicated by a still incomplete understanding of the extent to which they each influence the kinetics of drug release. Previous modeling approaches have been limited by necessity to incorporating the factors most influential to drug release or polymer breakdown for a particular delivery system<sup>10</sup>. Despite this limitation, computational models have still successfully simulated complex multi-phase drug release profiles from polymeric microparticles<sup>12,13,14,15</sup>. Few studies have extended these models to polymeric nanoparticles, though these are becoming prominent in therapeutic applications<sup>16</sup>.

The mechanism of drug release from nanoparticles may differ from that of microparticles even when both vehicles have the same polymer composition. Drug diffusion through the polymer matrix has been shown to be slower in nanoparticles than in microparticles, and this may be due to more dense internal structures as a result of fabrication techniques or the neutralization of autocatalysis-enhanced diffusion phenomenon at the smaller length scales<sup>8,9,17</sup>. For the purposes of our model, we postulate that the reduced drug diffusivity in nanoparticles limits the influence of diffusion in the model to the interface between polymer and the external aqueous environment. That is, we assume that drug release occurs only after degradation of surrounding polymer and the formation of an erosion channel to the particle surface. Once the drug diffuses into the exposed erosion channel, the drug is considered to be released due to the small distances necessary to travel to the particle surface at the nanoscale. Using this framework, we model drug release from bulk eroding nanoparticles based upon a three dimensional Monte Carlo simulation of polymer erosion.

### 2.3.2. Results and Discussion

For the Monte Carlo simulation presented here, entire spherical nanoparticles are represented using voxels. A voxel is the volume element which represents data on a regular grid in three dimensional space and is analogous to a pixel which is the area element representing data in two dimensions<sup>18</sup>. Previous two dimensional models have depicted drug release from a pixel as dependent upon the state of the pixel's immediate 8 neighbors<sup>12,14</sup>. In this three dimensional voxel-based model, we assess the influence of the 18 neighbors most immediately surrounding the voxel in order to give the best representation of a sphere (Fig. 1). The State Diagram (Fig. 2) describes the simulation algorithm governing voxel dynamic state transitions ( $x_{i,j,k}$ ) and voxel drug release. Assuming a homogeneous mixture of drug and polymer, each voxel begins with a voxel dynamic state ( $x_{i,j,k}$ ) of 1. The lifetime of individual voxels follows a Poisson's distribution given by:

$$T_{i,j,k}^L(t) = -\ln(\varepsilon/\lambda) \quad [1]$$

where  $\varepsilon$  is a random number and  $1/\lambda$  is the half life of the polymer system. Expiration of this lifetime changes the voxel dynamic state ( $x_{i,j,k}$ ) to zero and the polymer is considered degraded. In order for the polymer to be considered eroded, access to the aqueous environment via an erosion channel from the surface of the nanoparticle is required. Such a channel is formed when at least one of the 18 immediate neighboring voxels is eroded, i.e. any of the neighbor's dynamic voxel state ( $x_{i,j,k}$ ) becomes -1.

We formulated PLGA nanoparticles encapsulating the hydrophobic agent dexamethasone as described in Fig. 3. Hydrolysable polymers such as PLGA are often used in the formulation of nanoparticles as they combine sustained drug release with complete biodegradability<sup>19</sup>. The

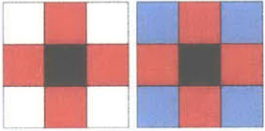
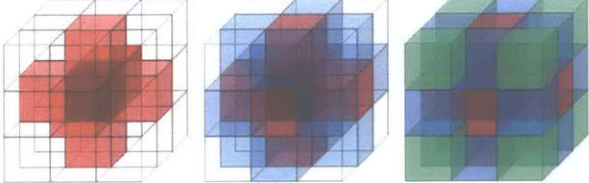
polymer half life ( $1/\lambda$ ) is approximated at 0.121 days from previous measurements in the literature<sup>20</sup>. In order to run the model simulation, we used the drug release data from this formulation to fit values for two parameters: the number of voxels (N) that compose each nanoparticle and a parameter ( $\kappa$ ) that integrates the influence of mass transport phenomenon into the simulation. The parameter  $\kappa$  (value between 0 and 1) measures the likelihood of drug release from an intact voxel into an aqueous erosion channel upon exposure, and represents the combined contributions of drug diffusion and dissolution on drug release at this interface. The parameter N is related to the physical size of the particle and also controls the surface area to volume ratio. Polymeric nanoparticles have a higher surface area to volume ratio than microparticles which may lead to a more pronounced relative initial burst of drug release.

The experimental release profile of dexamethasone from PLGA nanoparticles shows an initial burst release of 40% over the first ~25 hours. A more sustained phase of drug release occurs over the next ~120 hours resulting in complete release of encapsulated drug by 150 hours. The model simulation was a good match to experimental drug release with a coefficient of determination ( $R^2$ ) value of 0.98 (Fig. 3). We are also able to use our model simulation to investigate physical properties of the voxelated nanosphere during erosion by exploring the fragment size distribution and average size of the nanoparticles over time (Fig. 4a). Percolation-driven particle breakdown due to bulk erosion is shown to occur after 150 hours, and so does not appear to play a dominant role in drug release. A plot of nanoparticle surface area / volume with respect to time (Fig. 4b) indicates an initial lag prior to the formation of erosion channels. This corresponds well with the lag before the change in phase of experimental drug release from initial burst to sustained release (Fig. 3).

The potential of extending this model to additional drug formulations is explored through variation in the parameter  $\kappa$  (Fig. 5). The influence of  $\kappa$  is restricted to drug release at the interface of polymer and the external aqueous environment. A  $\kappa$  value of 1 corresponds to immediate drug release from an exposed intact voxel into an erosion channel, and the resultant rapid drug release profile is consistent with that of a highly hydrophilic drug<sup>21</sup>. A  $\kappa$  value of 0 indicates that drug release from an exposed intact voxel does not occur until the voxel is degraded, and the resultant sustained drug release profile is consistent with that of a polymer-conjugated drug<sup>22</sup>. Values of  $\kappa$  between 0 and 1 correspond with intermediate capacities for drug release from an exposed intact voxel, and the resultant multi-phase drug release profiles are consistent with that of a hydrophobic drug as presented here.

#### **2.3.4. Conclusion**

Because all processes that influence drug release are not yet quantitatively understood, there is value to the use of semi-empirical computational models able to simulate multi-phase drug release profiles. Use of the model presented here does not require knowledge of physical parameters such as polymer porosity, drug solubility, and drug diffusivity which are often not available or can be difficult to measure. Voxellation of the entire nanoparticle facilitates the extension of this platform to non-symmetrical vehicle formulations as well as non-uniform drug and polymer distributions. Variation of the parameter  $\kappa$  demonstrates the versatility of this model for simulating release of hydrophilic, hydrophobic, and polymer-conjugated drugs. This model was intended as a proof of principle, however in the future emerging mechanistic understandings of phenomenon influencing nanoparticle drug release may be incorporated to further increase accuracy and strengthen predictive power.

|  | PIXEL MODELS (2D)   |       | VOXEL MODELS (3D)  |             |        |
|--|---|-------|--|-------------|--------|
|  | n = 4   | n = 8 | n = 6  | n = 18      | n = 26 |
| $d = \sqrt{1}$   | 4   | 4     | 6  | 6           | 6      |
| $d = \sqrt{2}$   | 0   | 4     | 0  | 12          | 12     |
| $d = \sqrt{3}$   | 0   | 0     | 0  | 0           | 8      |
| $\text{CCDF} = \frac{\sum_{i=1}^3 d \times n(d = \sqrt{i})}{Z}, Z \begin{cases} 8 \vee 2\text{D} \\ 26 \vee 3\text{D} \end{cases}$ | 0.50  | 1.21  | 0.23   | <b>0.88</b> | 1.42   |
| $\text{SVR} = \frac{1 + \sum_{i=1}^3 n(d = \sqrt{i})}{\frac{4}{3} \pi (1.5)^3}$  | -   | -     | 0.42   | <b>1.27</b> | 1.84   |
| <b>Pictorial Depiction</b>   |  |       |  |             |        |

**Figure 1: Geometric implications of pixel and voxel neighborhoods.** The distance ( $d$ ) between the center of a pixel (in 2D) or voxel (in 3D) and the center of its immediate neighbors is  $\sqrt{1}$  or  $\sqrt{2}$  or  $\sqrt{3}$  units. The center to center distance factor (CCDF) and spherical volume ratio (SVR) are used to calculate the neighborhood ( $n$ ) that best approximates a circle (or a sphere) enclosed within the 2D pixel (or 3D voxel) grid. A schematic representation of the neighborhoods is depicted with the pixels/voxels colored black (center), red ( $d = \sqrt{1}$ ), blue ( $d = \sqrt{2}$ ) and green ( $d = \sqrt{3}$ ).

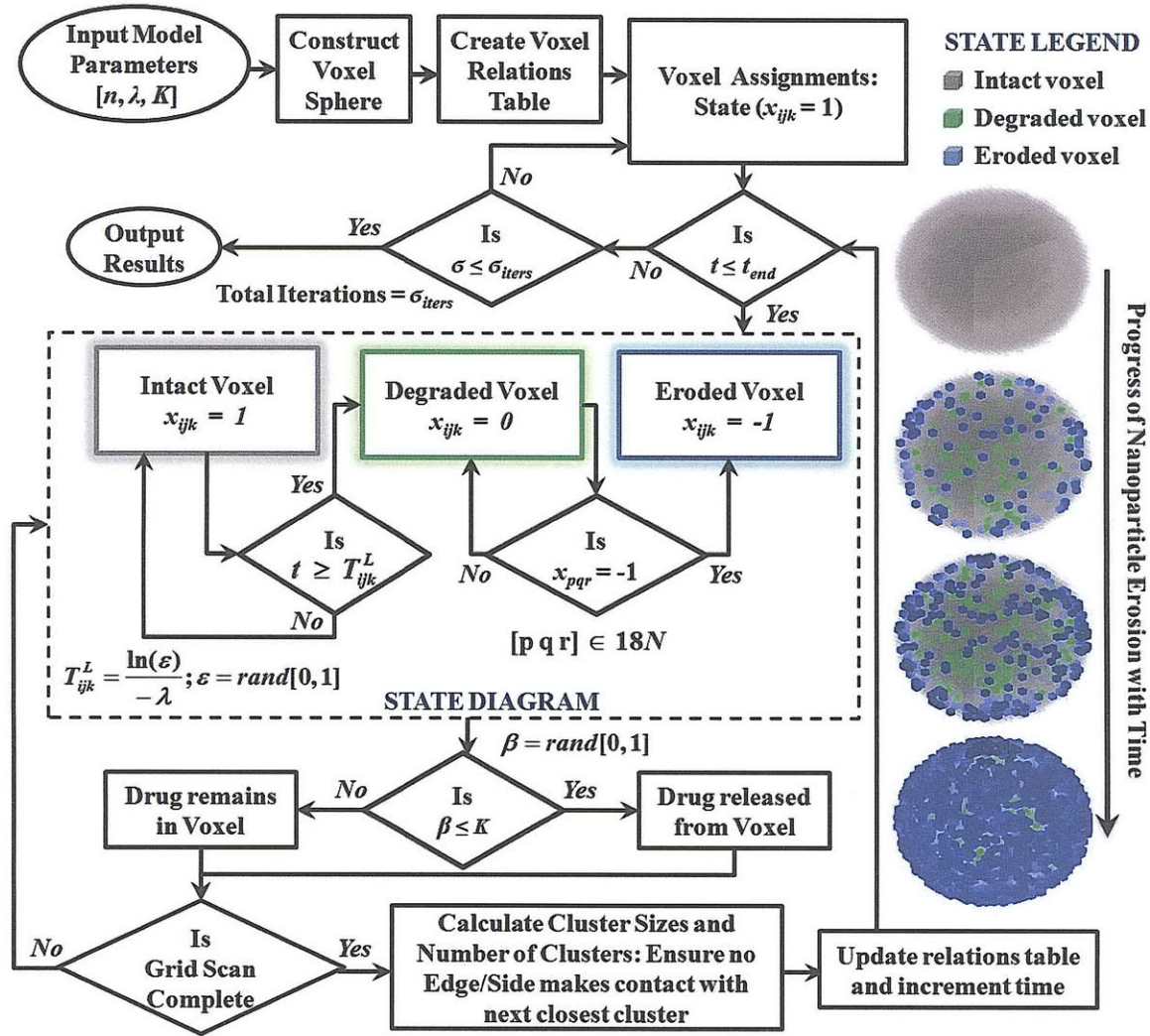


**Figure 2: Flowchart and state diagram governing the voxel-based model.** An illustration of the principles involved in estimation of voxel state transitions, nanoparticle fragmentation and drug release. A visualization of polymeric nanoparticle bulk erosion is also depicted.



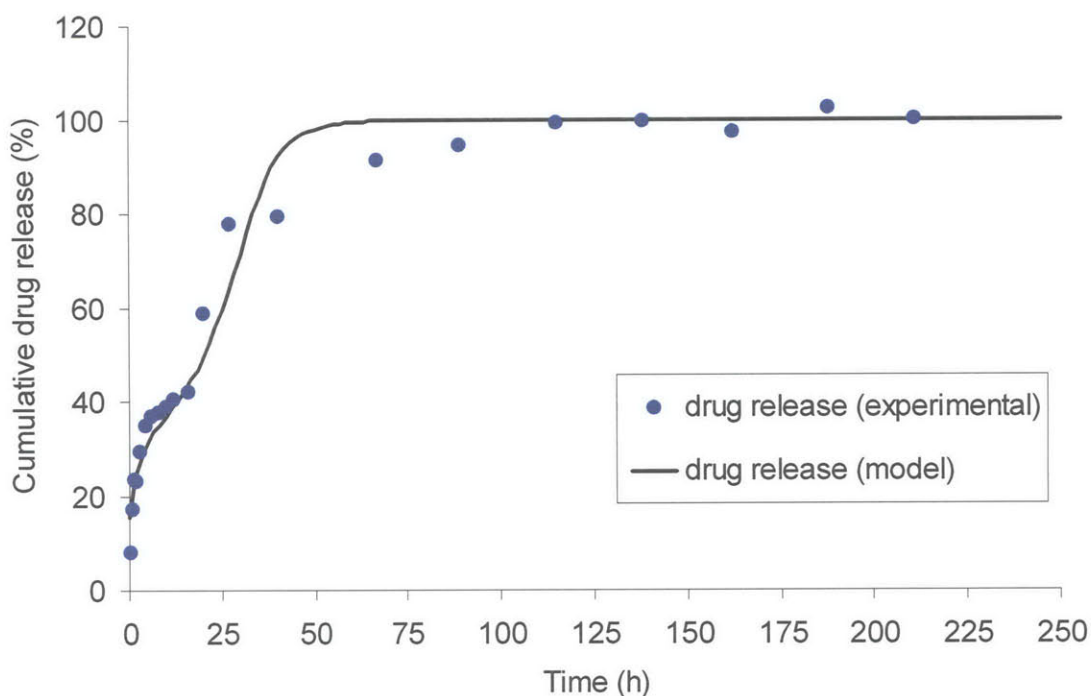


**Figure 3: Dexamethasone release from PLGA nanoparticles *in vitro*.** Nanoparticles were formulated using a modified emulsion-solvent evaporation technique<sup>23,24</sup>. Briefly, 25 mg of dexamethasone and 50 mg of PLGA were allowed to dissolve completely in 2.5 mL acetone before addition of 0.5 mL methanol and emulsification into an aqueous 2% PVA solution with sonication. Nanoparticles were separated from free drug by ultracentrifugation and were demonstrated to have a mean particle diameter of 115 nm by dynamic light scattering. Drug release was quantified by HPLC after dialysis against PBS at 37 °C with gentle shaking. Simulations of drug release were coded using the C programming language and were performed 100 times with mean values shown. The Monte Carlo simulation demonstrates good correlation with experimental data with  $R^2 = 0.98$ . Parameters:  $N = 5497$  voxels,  $\kappa = 0.5$ .

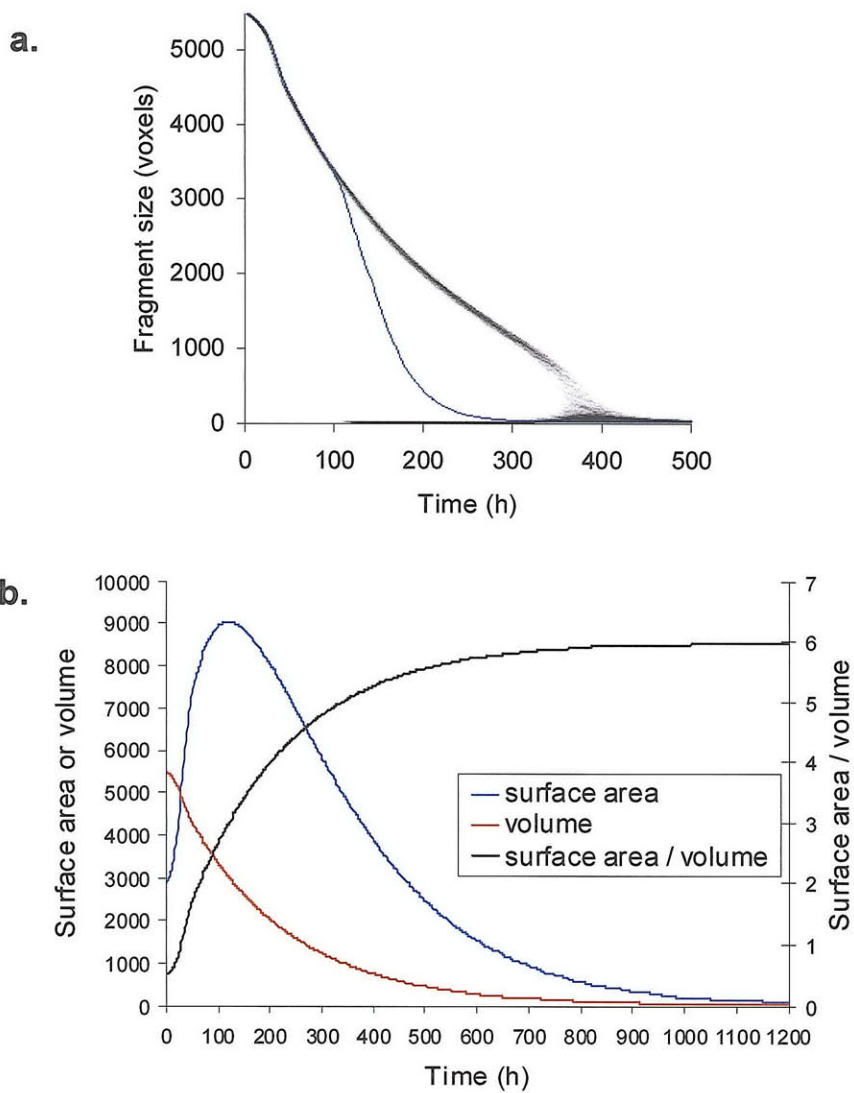


**Figure 4: Simulation of drug release and nanoparticle fragmentation.** **a.** Model representation of nanoparticle fragmentation: black scatter represents variability between different simulations, blue line represents average fragment size. **b.** Simulation results for surface area (exposed voxel area) and volume (voxel count) during nanoparticle fragmentation.

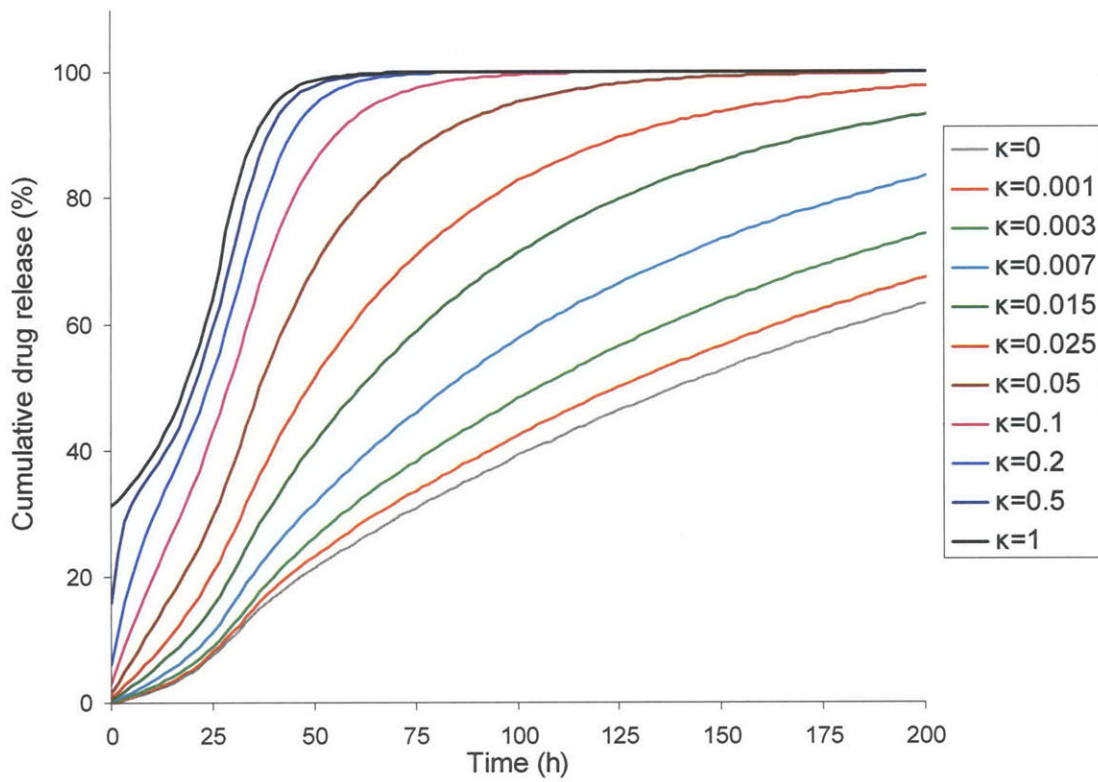


**Figure 5: Influence of the model parameter  $\kappa$  on drug release.** Simulation results for  $\kappa$  values between 0 and 1 demonstrate the capacity of the model for simulating the release of drugs with distinct diffusion and dissolution characteristics. Model parameters:  $N = 5497$  voxels, iterations = 100.

### 2.3.5. References

1. LaVan, D. A., McGuire, T. and Langer, R. (2003) Small-scale systems for in vivo drug delivery. *Nat Biotech* 21, 1184-1191.
2. Sengupta, S., Eavarone, D., Capila, I., Zhao, G., Watson, N., Kiziltepe, T. and Sasisekharan, R. (2005) Temporal targeting of tumor cells and neovasculature with a nanoscale delivery system. *Nature* 436, 568-572.
3. Gref, R., Minamitake, Y., Peracchia, M. T., Trubetsky V., Torchilin, V. and Langer, R. (1994) Biodegradable long-circulating polymeric nanospheres. *Science* 263, 1600-1603.
4. Panyam, J. and Labhasetwar, V. (2003) Biodegradable nanoparticles for drug and gene delivery to cells and tissue. *Adv Drug Deliv Rev* 55, 329-347.
5. Gopferich, A. (1997) Erosion of composite polymer matrices. *Biomaterials* 18, 397-403.
6. Zygourakis, K. and Markenscoff, P.A. (1996) Computer-aided design of bioerodible devices with optimal release characteristics: a cellular automata approach. *Biomaterials* 17, 125-135.
7. Gopferich, A., and Langer, R. (1995) Modeling of polymer erosion in three dimensions: Rotationally symmetric devices. *AIChE Journal* 41, 2292-2299.
8. Polakovic, M., Gorner, T., Gref, R. and Dellacherie, E. (1999) Lidocaine loaded biodegradable nanospheres. II. Modelling of drug release. *J Control Release* 60, 169-177.
9. Arifin, D. Y., Lee, L. Y. and Wang, C. H. (2006) Mathematical modeling and simulation of drug release from microspheres: Implications to drug delivery systems. *Adv Drug Deliv Rev* 58, 1274-1325.
10. Siepmann, J. and Gopferich, A. (2001) Mathematical modeling of bioerodible, polymeric drug delivery systems. *Adv Drug Deliv Rev* 48, 229-247.
11. Gopferich, A. (1996) Mechanisms of polymer degradation and erosion. *Biomaterials* 17, 103-114.

12. Gopferich, A., and Langer, R. (1993) Modeling of polymer erosion. *Macromolecules* 26, 4105-4112.
13. Faisant, N., Siepmann, J. and Benoit, J. P. (2002) PLGA-based microparticles: elucidation of mechanisms and a new, simple mathematical model quantifying drug release. *Eur J Pharm Sci* 15, 355-366.
14. Siepmann, J., Faisant, N. and Benoit, J.P. (2002) A New Mathematical Model Quantifying Drug Release from Bioerodible Microparticles Using Monte Carlo Simulations. *Pharmaceutical Research* 19, 1885-1893.
15. Zhang, M., Yang, Z., Chow, L.L. and Wang, C.H. (2003) Simulation of drug release from biodegradable polymeric microspheres with bulk and surface erosions. *J Pharm Sci* 92, 2040-2056.
16. de la Zerda, A. and Gambhir, S. S. (2007) Drug delivery: Keeping tabs on nanocarriers. *Nat Nano* 2, 745-746.
17. Liggins, R. T. and Burt, H. M. (2001) Paclitaxel loaded poly(L-lactic acid) microspheres: properties of microspheres made with low molecular weight polymers. *Int J Pharm* 222, 19-33.
18. Arie, E. K. (1996) Volume visualization. *ACM Comput Surv* 28, 165-167.
19. Siepmann, J., Elkharraz, K., Siepmann, F. and Klose, D. (2005) How autocatalysis accelerates drug release from PLGA-based microparticles: a quantitative treatment. *Biomacromolecules* 6, 2312-2319.
20. Birnbaum, D. T. and Brannon-Peppas., L. (2003) Molecular weight distribution changes during degradation and release of PLGA nanoparticles containing epirubicin HCl. *J Biomater Sci Polym Ed* 14, 87-102.
21. Yoo, H. S., Lee, K. H., Oh, J. E. and Park, T.G. (2000) In vitro and in vivo anti-tumor activities of nanoparticles based on doxorubicin-PLGA conjugates. *Journal of Controlled Release* 68, 419-431.

22. Yoo, H. S., Oh, J. E., Lee, K. H. and Park, T. G. (1999) Biodegradable Nanoparticles Containing Doxorubicin-PLGA Conjugate for Sustained Release. *Pharmaceutical Research* 16, 1114-1118.
23. Cascone, M. G., Pot, P. M., Lazzeri, L. and Zhu., Z. (2002) Release of dexamethasone from PLGA nanoparticles entrapped into dextran/poly(vinyl alcohol) hydrogels. *J Mater Sci Mater Med* 13, 265-269.
24. Panyam, J., Williams, D., Dash, A., Leslie-Pelecky, D. and Labhasetwar, V. (2004) Solid-state solubility influences encapsulation and release of hydrophobic drugs from PLGA/PLA nanoparticles. *J Pharm Sci* 93, 1804-1814.

## **2.4. Structure-function Relationships of Novel Carbohydrate-Based Therapeutic Agents**

### **2.4.1. Introduction**

It is our hope that the development of novel therapeutic compounds with utility both as structural and bioactive components will lead to more efficient nanocells with rapid clinical application. One class of therapeutic agents that holds promise for this role is modified pectin. Pectin is a major component of all primary cell walls and consists of a complex carbohydrate network composed predominantly of galacturonic acid rich polysaccharides.

This complex pectin matrix may be fragmented via temperature, pH, or enzymatic modification into shorter, soluble oligosaccharide chains. One method of fractionating pectin has led to a subpopulation of pectin fragments with anti-tumor activity. These shorter pectin chains dissolve more readily in water and it is believed that they contain polysaccharides having affinity for cell-surface galectin-3<sup>1</sup>. Galectins are a family of animal lectins defined by their ability to recognize  $\beta$ -galactose and by conserved amino acid residues within the carbohydrate recognition domains. Currently 15 mammalian galectins have been identified, with several implicated in regulation of tumor apoptosis, inflammation, and immune escape<sup>2</sup>. Modified pectins have demonstrated therapeutic benefit for inhibiting tumor growth, adhesion, metastasis, and angiogenesis in several tumor models over the past decade including melanoma<sup>3,4</sup>, breast cancer<sup>5</sup>, and colon cancer<sup>6</sup>, and one pilot phase II human clinical trial for prostate cancer<sup>7</sup>. The cheap, ready availability of pectin in combination with a virtual total lack of negative side effects has made understanding the mechanism of action of these intriguing new anticancer molecules of critical importance.

The proposed therapeutic mechanism is currently that pectin inhibits tumors through its binding to galectin-3<sup>8</sup>. No direct mechanism has yet been elucidated, and this is probably due to multiple considerations. First, the temperature and pH modifications used to generate anti-tumor pectin are likely dependent upon the pectin starting source. Pectins obtained from major research laboratory vendors have considerable batch-to-batch variability in methods of isolation, and so can be expected to have substantial variations in starting structure. Because pectin is so diverse in terms of structure both within and between samples, it has so far been a substantial challenge to identify structure-function relationships relating pectin structure and anti-tumor activity. Second, while galectin-3 appears to play a probable role in pectin mediated anti-tumor activity, the mechanism of action may not be entirely due to this galectin. Additional galectins, including galectin-1<sup>9,10</sup>, have established roles in regulating tumor apoptosis, angiogenesis, and immune escape, and also have affinity for residues present within the complex polysaccharide environment of the pectin matrix<sup>11</sup>.

We demonstrate here an integrative approach for the standardization and structure-function analysis of a new class of anti-tumor modified pectins classified here as activated citrus pectin (ACP) obtained by a new methodology from a consistent source of native citrus pectin (NCP) isolated directly from lemon. We incorporate complementary analytical techniques to link ACP structure with binding to tumor galectin targets. We further provide evidence for a mechanism of action by elucidating key constituents of an ACP-induced anti-tumor intracellular signaling cascade. A better understanding of ACP anti-tumor activity as it relates to its structural modification will allow the synthesis of more effective and more reliable anti-tumor pectin agents.



## 2.4.2. Materials and Methods

### Preparation of pectins

NCP was isolated from lemon peels by a modification of a published procedure<sup>20</sup>. Briefly, albedo was separated from fresh lemon peels and pectin was isolated under conditions of high heat and pressure. After cooling, pectin was filtered and precipitated. The pectin pellet was dissolved in distilled water and lyophilized. Pectin extract (NCP) was incubated with base at high temperature. The resulting pectin contained low molecular weight pectic epitopes classified here as ACP. For use in sterile biological assays, the pH of pectin samples was increased to 6.5 and samples were filter sterilized.

### Capillary electrophoresis

Pectins (40  $\mu$ L, 20  $\mu$ g) were partially depolymerized by incubation with 200 mM TFA at 80 °C for 72 h. The resulting hydrolysates were lyophilized and resuspended in 30  $\mu$ L of 60 mM sodium acetate (pH 5) containing 3 mM  $\text{CaCl}_2$ . Two  $\mu$ L of dialyzed pectinase mixture (Sigma, 0.3 U / mL) were added and sample was incubated for 48 hours at 45 °C to achieve full depolymerization<sup>21</sup>. The pectinase reaction products were lyophilized and labeled with 8-aminopyrene-1,3,6-trisulfonic acid trisodium salt (APTS) according to a modified procedure<sup>22</sup>. Briefly, 15  $\mu$ L of 25 mM APTS in 15 % acetic acid and 5  $\mu$ L of 1 M  $\text{NaBH}_3\text{CN}$  were added to dry pectin powder. The mixture was incubated at 55 °C for 90 min before stopping the reaction by adding 500  $\mu$ L of distilled water. Monomeric carbohydrate standards representing the composition of pectin were also labeled with APTS as described. Capillary electrophoresis analysis of APTS-labeled pectin components was performed with a ProteomeLab PA 800

(Beckman-Coulter Inc.) with a 40 cm bare-fused silica capillary (Polymicro Technologies) running 42 mM sodiumtetraborate (pH 10.2) with Ar laser detection.

## **<sup>1</sup>H-NMR**

<sup>1</sup>H-NMR was performed at 80 °C using a Bruker 400 MHz instrument with an average of 256 measurements. Sodium 3-(trimethylsilyl)propionate-2,2,3,3-d<sub>4</sub> (TMSP) (Cambridge Isotope Laboratories Inc.) was used as a reference. Pectin was prepared for NMR by lyophilization and resuspension in D<sub>2</sub>O. Pectin concentrations were 10 mg / mL, pD of the solution was 4. Methodology for calculating pectin methylation and relative amount of 4,5-dehydrogalacturonic acid have been previously described<sup>23,24</sup>.

## **In vivo tumor studies**

For primary tumor growth studies, B16F10 melanoma cells ( $2.5 \times 10^5$ ) were implanted in the left flank of male C57/BL6 mice on day 0. ACP (0.5 mg/mouse) or NCP (0.5 mg/mouse) were diluted in 100  $\mu$ L PBS and injected s.c. in the left flank every third day starting on day 7 when the tumors had reached 100 mm<sup>3</sup> in volume on day 7. Mice were sacrificed as required by control tumor burden as on day 17. For experimental metastasis studies, B16F10 melanoma cells were treated with 0.5% NCP (1 mg/mouse), 0.5% ACP (1 mg/mouse) or PBS for 30 minutes and injected into the tail vein of C57/BL6 mice on day 0 similarly to previously described<sup>2</sup>. On day 10, mice were sacrificed and lungs were excised and fixed in Bouin's solution. Metastatic nodules were counted with the aid of a dissecting microscope.

## **Cell Viability**

Cell viability was measured using the WST-1 reagent (Roche) according to manufacturer's instructions. Briefly, B16F10 cells were plated in a 96 well plate so that they would be ~50% confluent after 24 h. Cells were then treated with 1 mg/mL NCP, 1 mg/mL ACP, or PBS control. After an additional 24 hours, cells were incubated with 10% WST-1 reagent and cell viability was quantified by absorbance at 450 nm.

## **Chemoinvasion through matrigel**

A measure of chemoinvasion was performed similarly to that described previously.<sup>25</sup> Briefly, Transwell inserts (Corning Inc., Corning, NY; 8  $\mu$ m pore size, 6.5 mm diameter) were coated with 15  $\mu$ g of Matrigel (Becton Dickinson) and allowed to dry overnight in a sterile laminar flow hood. Serum-deprived (0.1% FBS, overnight) B16F10 cells ( $2 \times 10^5$ ) were treated with APC or NPC and were added to the top of inserts contained within growth medium (500  $\mu$ l) supplemented with growth factor (40 ng/mL HGF) as a chemoattractant. After 40 h incubation, non-invaded cells were removed using cotton swabs, and invaded cells were fixed using 2.5% gluteraldehyde in PBS. Invaded cells were stained with crystal violet and counted with a Zeiss Axiovert 200M microscope using 9 fields of view per insert.

## **Western blotting**

Tissue samples were lysed in sample buffer and resolved on a 4–12% gradient SDS–polyacrylamide-gel electrophoresis gel. The proteins were transferred to a nitrocellulose membrane, blocked, and probed with primary antibodies to phospho-Akt (Ser473), phospho-Akt(Thr308), phospho-PTEN(Ser380), and PTEN (Cell Signaling) as well as actin as a loading control (Santa Cruz Biotechnology). Proteins were detected by chemiluminescence after

incubation with the appropriate secondary horseradish peroxidase-labeled antibodies and visualized with a Kodak 2000 gel-imaging system.

### **Cloning of human Gal-1 and Gal-3**

Gal-1 and Gal-3 were cloned using cDNA isolated from HUVECs. Cloning primers containing NheI (5' end of the gene) and Sall (3' end of the gene) restriction sites are shown below.

#### **GAL-1**

5'-ATATTGCTAGCATGGCTTGTGGTCTGGTCGCCAGCAACCTG-3'

5'-ATATTGTCGACTTAGTCAAAGGCCACACATTTGATCTTGAAGTC-3'

#### **GAL-3**

5'-ATATTGCTAGCATGGCAGACAATTTTTTCGCTCCATGATGCG-3'

5'-ATATTGTCGACTTATATCATGGTATATGAAGCACTGGTGAG-3'

The vector (pET-28a(+)) was prepared with NheI and Sall followed by treatment with CIP Alkaline Phosphatase (NEB) and purification with gel electrophoresis and gel extraction (Qiagen). Ligation was performed with T4 DNA ligase (NEB) at 16 °C for 16 h. The galectin-vector constructs were transformed into *E. coli* JM109. The pET-28a(+) constructs were transformed into *E. coli* Rosetta2 (DE3) (Novagen) to overcome the unfavorable codon bias. The cultures were grown in LB media containing kanamycin (100 µg/mL) and chloramphenicol (40 µg/mL) at 37 °C. In mid-log phase protein expression was induced with 1 mM IPTG for 18 h. Induced *E. coli* Rosetta2 (DE3) cells were disrupted with sonication and the crude extract was rid

of debris by centrifugation (20000 rpm, 10 min, 4 °C) and purified with a Pharmacia 5 mL HiTrap Chelating HP column using FPLC according to manufacturer's instructions. Proteins were dialyzed through a 2000 MWCO membrane (Spectrum Laboratories Inc.) against magnesium and calcium-free PBS and concentrated with 3000 MWCO Centriplus Centrifugal Filter Devices (Millipore) at 4 °C. Histidine tags were removed with thrombin (Sigma) treatment. Galectins were labeled with 5-(and6)carboxyfluorescein succinimidyl ester (CFSE) from Fluka. Proteins at 0.5 mg /mL in 50% PBS buffer were incubated with 1.5 mg/mL CFSE (in DMSO) in 9:1 ratio (v/v) for 2 h at RT. Proteins were dialyzed against 50% PBS through a 10000 MWCO membrane (Spectrum Laboratoris Inc.).

### **Gal-1 and Gal-3 interaction with pectin**

Colorless polystyrene microspheres (3 µm diameter, Polysciences) were stably adsorbed with either of the following: 50 µg lactose, 50 µg sucrose, 50 µg ACP, 50 µg NCP, 5 µg anti-Gal-1 antibody or 5 µg anti-Gal-3 antibody. Adsorption of lactose, sucrose or pectin was carried out by incubation with approximately  $10^9$  microspheres in 50 mM carbonate/bicarbonate buffer (Sigma), pH 9.6, 37 °C for 3 h. Adsorption of antibodies was carried out by incubation with approximately  $10^9$  microspheres in 0.1 M boric acid, pH 8.5, 37 °C for 2 h. Microspheres were washed with water after either procedure. The treated microspheres were incubated with FITC-labeled recombinant Gal-1 and Gal-3 for 30 minutes on ice, and analyzed by flow cytometry in the presence of increasing concentrations of lactose. Buffer-treated microspheres were used as negative controls whereas anti-Gal-1 and anti-Gal-3 treated microspheres were used as positive controls for Gal-1 and Gal-3 binding, respectively.

## FACS

Intracellular quantification of protein phosphorylation by flow cytometry was performed similarly to previously described<sup>26,27</sup>. Cells were treated with ACP (1 mg/mL), NCP (1 mg/mL), or PBS control for 30 minutes in the presence of PBS, anti-Gal-1, or anti-Gal-3. Cells were gently detached from the culture plate with 0.02% EDTA in PBS and immediately fixed with 2.5% v/v formaldehyde in PBS for 5 minutes on ice, washed once and permeabilized in PB buffer (5% w/v BSA, 1% v/v rabbit serum, 0.1% w/v saponin, 10mM HEPES, 0.05% w/v NaN<sub>3</sub> in PBS, pH 7.4) for 10 minutes on ice. The following primary antibodies were used (at 5 µg/mL or diluted 1:100 in PBS containing 0.1% w/v BSA, 0.1% w/v saponin, 10 mM HEPES and 0.05% w/v NaN<sub>3</sub>, pH 7.4, 25 minutes on ice): phospho-Akt (Ser473), phospho-Akt(Thr308), phospho-PDK1(Ser241), phospho-PTEN(Ser380), PTEN (Cell Signaling), phospho-PI3K(Tyr508) (Santa Cruz Biotechnology), and rabbit IgG (Sigma, 5 µg/mL) as an isotype control. Cells were washed and stained with fluorescein-conjugated anti-rabbit or anti-goat antibodies (Invitrogen), 5 µg/mL in PBS containing 0.1% w/v BSA, 0.1% w/v saponin, 10 mM HEPES and 0.05% w/v NaN<sub>3</sub>, pH 7.4, 20 minutes on ice, followed by data acquisition on a Beckman-Coulter Cell Lab Quanta SC MPL-enhanced flow cytometer. Means and coefficients of variance produced by the Quanta Analysis™ software were used for statistical evaluations.

## PTEN knockdown

PTEN expression was knocked down using the SignalSilence PTEN siRNA kit (Cell Signaling) according to manufacturer's instructions. Briefly, B16F10 cells were plated in a 96 well plate such that they would reach ~50% confluence after 24 hours. At this time, PTEN expression was knocked down using targeted siRNA constructs with the supplied transfection

reagent overnight. Media was replaced and cells were treated with NCP (1 mg/mL), ACP (1 mg/mL) or PBS control for 30 minutes before harvesting for protein analysis. Intracellular flow cytometry quantification of protein phosphorylation analysis was performed as described above.

### **2.4.3. Results and Discussion**

Treatment of pectin with high pH or high temperature favors demethylation or beta-elimination (fragmentation) of the pectin backbone, respectively. Beta-elimination, which also leads to formation of 4,5-dehydro-galacturonic acid (dGalA), requires methylation of carboxyl groups so is inhibited by a high pH/temperature ratio. The ratio of these two parameters can be selected to achieve the desired amounts of methylation and defragmentation.<sup>11,12</sup> We employed a combination of high heat and base in a ratio to promote the formation of demethylated, soluble pectin epitopes.

To quantify structural differences between NCP and ACP, we used capillary electrophoresis (CE) and <sup>1</sup>H-NMR to analyze oligomeric composition as well as esterification of GalA residues. CE analysis demonstrates that ACP contains proportionally reduced amounts of neutral monosaccharides and increased amounts of GalA compared to NCP (Fig. 1a). <sup>1</sup>H-NMR spectrum of ACP indicates that ~8% of GalA were converted to dGalA and that GalA was

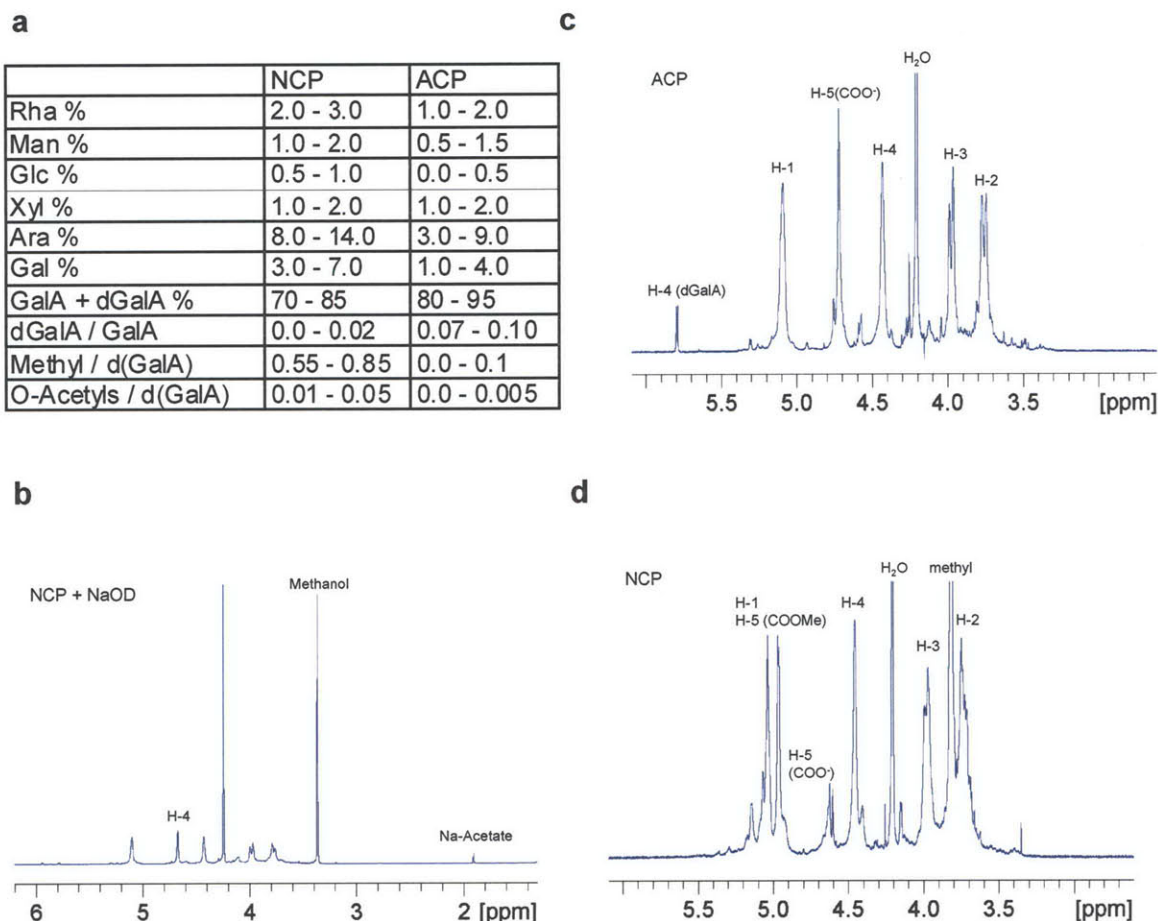


**Figure 1: Capillary electrophoresis and NMR analysis.** (a) Composition of NCP and ACP as determined by CE and  $^1\text{H-NMR}$ . [Representative range] (b) Measurement of acetylation and methylation of NCP. The 400 MHz  $^1\text{H-NMR}$  spectra of NCP at 80 °C after addition of 0.1 M NaOD (final conc.) shows formation of methanol and Na-acetate. Amounts of methylation and acetylation were calculated by comparing ratios of H-4 of GalA (4.44 ppm) and H-4 of dGalA (5.78 ppm) with those of methanol (3.3 ppm) and Na-acetate (1.9 ppm)<sup>23</sup>. (c), (d): 400 MHz  $^1\text{H-NMR}$  spectra of ACP and NCP demonstrating differences in amounts of dGalA and methylation state. H-4 of GalA (4.44 ppm) and H-4 of dGalA (5.78 ppm) were used to determine the relative amount of dGalA present.



free of methylation and acetylation (Fig. 1a,c). In contrast, NCP contained ~70% methylated GalA residues and dGalA was not present (Fig. 1a,b,d). These results collectively indicate that deesterification, fragmentation, and enrichment for the galacturonic-acid containing polysaccharide backbone are all major structural differences between ACP and NCP.

To determine the anti-tumor efficacy of ACP, we tested this compound *in vitro* and *in vivo* using the well characterized, metastatic B16F10 mouse melanoma cell line. To assess the role of ACP on primary tumor growth, B16F10 cells were implanted *s.c.* into C57/BL6 mouse flanks. Treatment every third day with ACP inhibited tumor growth by ~50% over the course of our study compared to control and NCP treatment (Fig. 2a,b). In a separate experiment, ACP-treated B16F10 cells were injected *i.v.* into C57/BL6 mice to assess the role of ACP on tumor metastasis. ACP treatment inhibited the formation of lung metastatic nodules by ~30% compared to control and NCP treatment (Fig. 2c,d). ACP had no measurable effect on cell viability under *in vitro* culture conditions (Fig. 2e), indicating a mechanism of activity independent of direct tumor cell cytotoxicity. The *in vivo* anti-metastatic effect was corroborated by *in vitro* experiments, with ACP exhibiting a dose-dependant inhibition of B16F10 chemoinvasion through matrigel (Fig. 2f).

To identify potential therapeutic tumor targets for pectin, we assessed the relative binding affinities of galectin-1 (Gal-1) and galectin-3 (Gal-3) for ACP and NCP. Gal-3 has previously been implicated as a primary tumor target for modified pectins,<sup>13</sup> however a recent study demonstrated that modified pectins could still be effective against tumor cell lines lacking Gal-3 expression.<sup>7</sup> This indicates the presence of as yet unknown pectin targets, so we also included in our binding assays Gal-1, an additional galectin with an established role in tumor progression and the potential to bind pectin residues.<sup>14</sup> To measure binding, ACP and NCP were adsorbed to

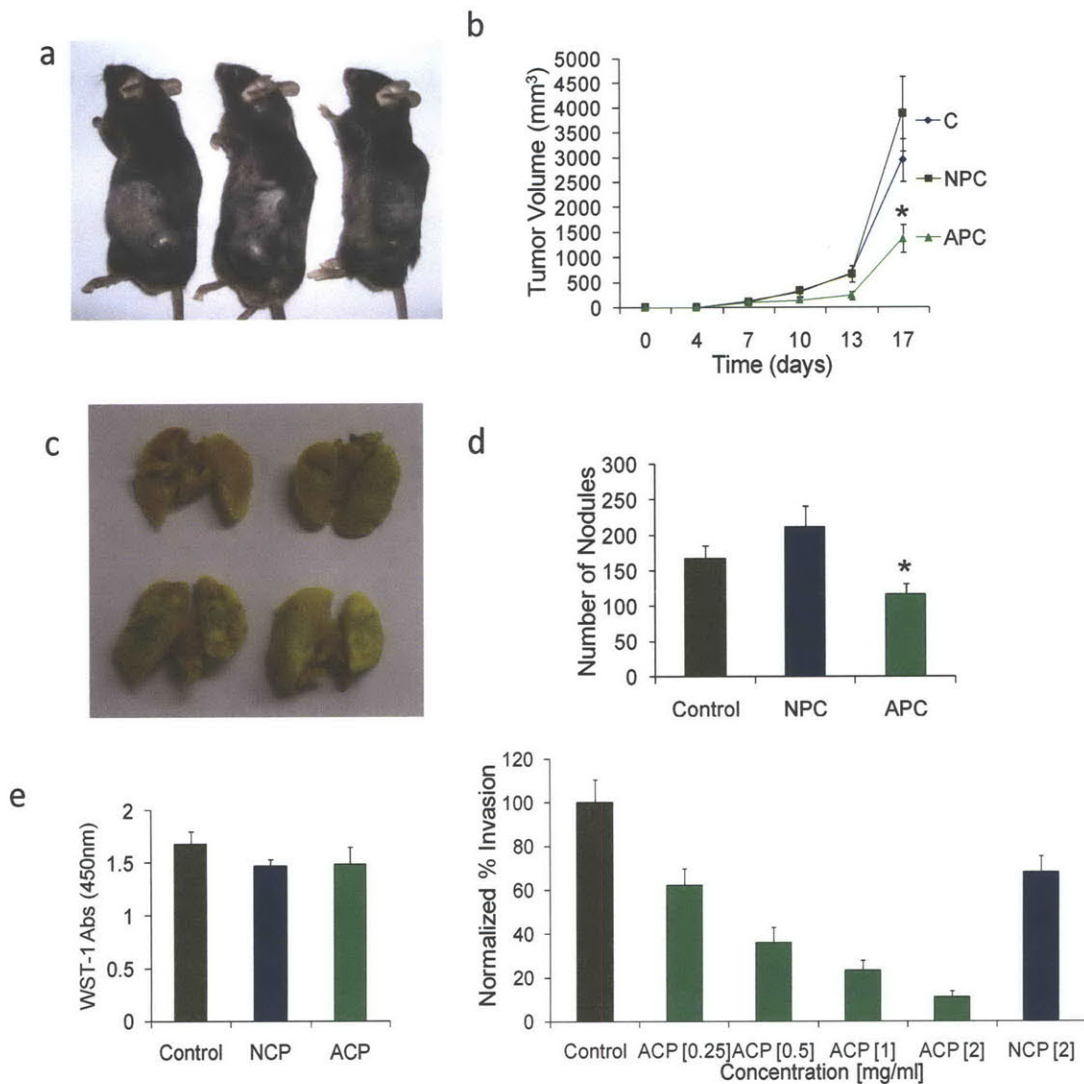


**Figure 2: Anti-tumor efficacy *in vivo* and *in vitro*.** (a),(b) Comparing the effects of treatment with NCP, ACP, and PBS control every third day on the growth of a B16F10 primary site implant. (c),(d) Comparing the effects of treatment with ACP, NCP, and PBS control on the number of B16F10 metastatic nodules on the lung in an experimental metastasis model. (e) Measure of cell viability after treatment with NCP, ACP, and PBS control using WST-1 and quantification by absorbance at 450 nm. (f) The effect of NCP, ACP, and PBS control on B16F10 chemoinvasion through matrigel in response to HGF. Only the highest concentration of NCP is pictured for comparison. Results are presented as means  $\pm$  s.e.m. \*P < 0.05 vs. control.

polymer beads and the adhesion of fluorescently labeled Gal-1 and Gal-3 was quantified by FACS. Binding measurements were taken in the presence of increasing amounts of a lactose inhibitor to distinguish relative binding affinity and the specificity of binding for the bioactive carbohydrate recognition domains (CRDs) of the galectins. Binding to the CRDs of both Gal-1 and Gal-3 was significantly greater for ACP than for NCP (Fig. 3a), indicating that the ACP activation protocol promotes the formation of galectin-binding structures.

To identify a potential mechanism of anti-tumor activity, we evaluated changes to the intracellular AKT signaling pathway after treatment. Treatment of B16F10 cells with ACP reduced AKT phosphorylation at both the Thr308 and Ser472 residues in contrast to treatment with NCP and control (Fig. 3b). Reduced phosphorylation of AKT is known to promote a diverse anti-tumor response, since AKT is a central regulator of a multitude of tumor processes including growth, survival, and metabolism.<sup>15,16</sup> We explored whether AKT dephosphorylation is mediated by ACP binding to galectins. Tumor cells were treated with ACP in combination with antibodies to Gal-1 or Gal-3 to competitively inhibit ACP-galectin binding. Inhibited binding to either galectin partially inhibited the dephosphorylation of AKT after ACP treatment, indicating that binding to both galectins is involved in promoting an anti-tumor AKT-mediated signaling cascade.

To further elucidate the anti-tumor mechanism, we investigated the involvement of two regulators of AKT phosphorylation: PI3K and PTEN. PI3K is a classic therapeutic target that promotes the phosphorylation of PIP2 to PIP3 which in turn acts to phosphorylate AKT.<sup>16</sup> In contrast PTEN, a recently identified therapeutic target, promotes the dephosphorylation of PIP3 to PIP2 which in turn acts to dephosphorylate AKT.<sup>8,17</sup> Western blotting demonstrated that phosphorylation of PTEN at Ser385 was increased after ACP treatment, and this change was not

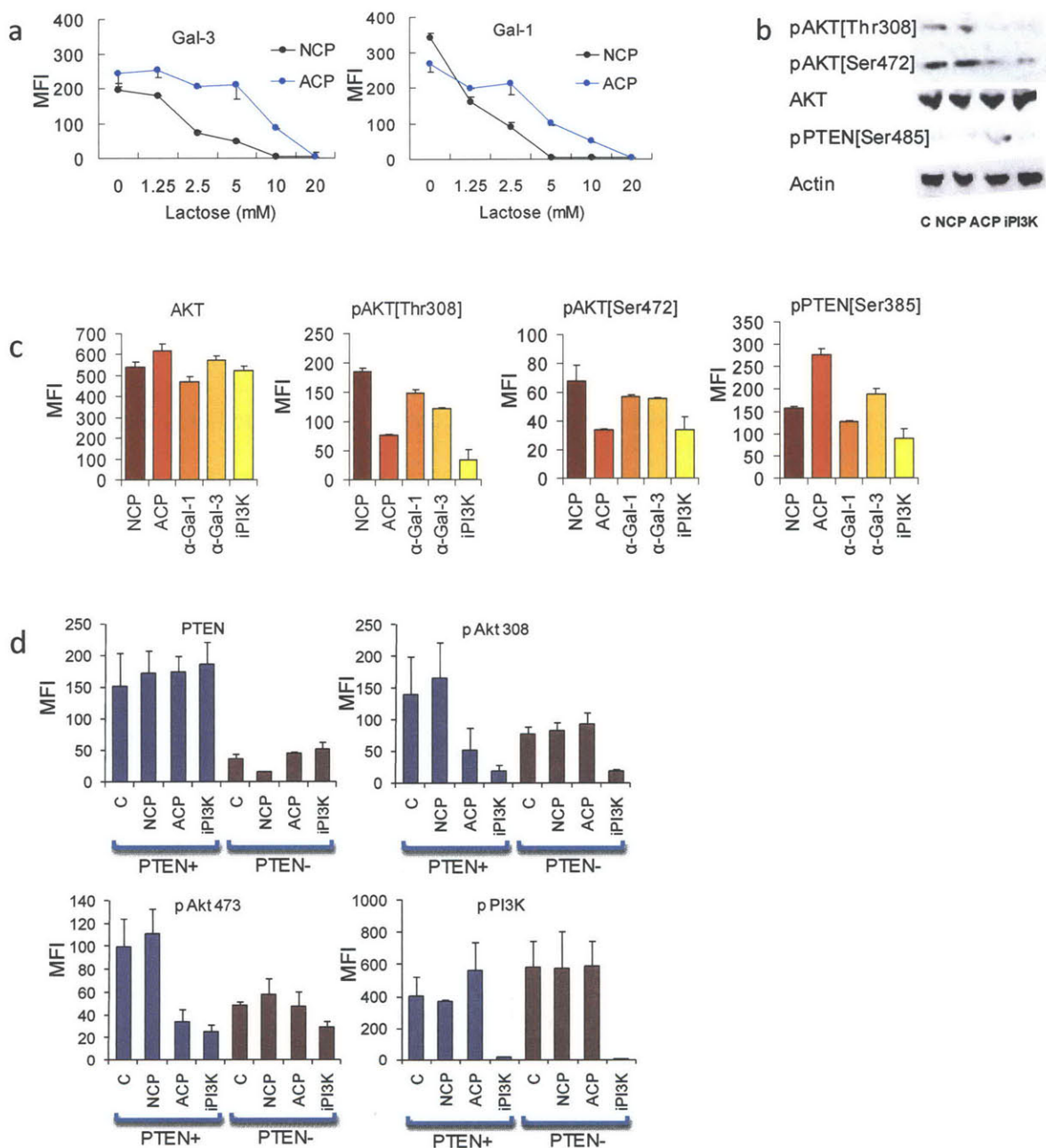


**Figure 3: Pathway analysis of anti-tumor activity.** (a) Interaction of fluorescently labeled galectin-1 and galectin-3 with NCP and ACP adsorbed to polystyrene beads. Sucrose and anti-galectin antibodies were used as negative and positive controls, respectively. (b) Western blot of the AKT signaling pathway after treatment with NCP, ACP, and PBS control. (c) Flow cytometry analysis of phosphoprotein levels after inhibition of pectin treatment with anti-galectin-1 and anti-galectin-3 antibodies. (d) Flow cytometry analysis of phosphoprotein levels after NCP, ACP, iPI3K, and PBS control treatment of B16F10 cells that have had PTEN knocked down by siRNA inhibition. Results are presented means and coefficients of variance produced by the Quanta Analysis™ software. MFI: Mean Fluorescence Intensity.

present after treatment of cells with a PI3K inhibitor (Fig. 3a). We next evaluated whether PTEN was the initiator of AKT dephosphorylation after ACP treatment using siRNA silencing of PTEN. ACP treatment no longer resulted in AKT dephosphorylation after PTEN silencing, though the effect of the PI3K inhibitor on the AKT pathway was unchanged (Fig. 3d). PI3K phosphorylation was also found to be inhibited by the PI3K inhibitor and not by ACP treatment (Fig. 3d). These results collectively demonstrate that PTEN activity is necessary for AKT dephosphorylation after ACP treatment and that PI3K is not a target for ACP.

#### **2.4.4 Conclusion**

We present here a standardized methodology for generating ACP using activation and isolation conditions that promote the formation of soluble, bioactive pectin epitopes. We provide an integrative approach to link pectin structure with anti-tumor efficacy and intracellular mechanism of action. We demonstrate the first structure-function link that Gal-1 and Gal-3 binding promotes an anti-tumor intracellular signaling cascade mediated by the dephosphorylation of AKT. The identification of PTEN as an essential mediator of ACP's effect on this pathway has direct implications for the potential translation of pectin as a clinical therapy. Recent evidence has demonstrated that PTEN is also an essential mediator of activity for the anti-tumor agent trastuzumab.<sup>9</sup> Trastuzumab, an antibody to the erbB2 receptor, is a clinically successful adjunct therapy for breast cancer that acts by disrupting AKT signaling.<sup>19</sup> In fact, tumor expression of PTEN may be more indicative of therapeutic efficacy than over-expression of the erbB2 receptor.<sup>9</sup> Our results collectively suggest that ACP acts through a similar mechanism, and may therefore have the potential to provide a safe, readily available alternative adjunct therapy for patients with PTEN mediated pathology.

#### 2.4.5. References

1. Mohnen, D. Pectin structure and biosynthesis. *Curr Opin Plant Biol* 11, 266-277 (2008).
2. Platt, D. & Raz, A. Modulation of the lung colonization of B16-F1 melanoma cells by citrus pectin. *J Natl Cancer Inst* 84, 438-442 (1992).
3. Pienta, K.J., et al. Inhibition of spontaneous metastasis in a rat prostate cancer model by oral administration of modified citrus pectin. *J Natl Cancer Inst* 87, 348-353 (1995).
4. Nangia-Makker, P., et al. Inhibition of human cancer cell growth and metastasis in nude mice by oral intake of modified citrus pectin. *J Natl Cancer Inst* 94, 1854-1862 (2002).
5. Guess, B.W., et al. Modified citrus pectin (MCP) increases the prostate-specific antigen doubling time in men with prostate cancer: a phase II pilot study. *Prostate Cancer Prostatic Dis* 6, 301-304 (2003).
6. Chauhan, D., et al. A novel carbohydrate-based therapeutic GCS-100 overcomes bortezomib resistance and enhances dexamethasone-induced apoptosis in multiple myeloma cells. *Cancer Res* 65, 8350-8358 (2005).
7. Jackson, C.L., et al. Pectin induces apoptosis in human prostate cancer cells: correlation of apoptotic function with pectin structure. *Glycobiology* 17, 805-819 (2007).
8. Gonzalez, J. & de Groot, J. Combination therapy for malignant glioma based on PTEN status. *Expert Rev Anticancer Ther* 8, 1767-1779 (2008).
9. Park, B.H. & Davidson, N.E. PI3 kinase activation and response to Trastuzumab Therapy: what's neu with herceptin resistance? *Cancer Cell* 12, 297-299 (2007).
10. Ridley, B.L., O'Neill, M.A. & Mohnen, D. Pectins: structure, biosynthesis, and oligogalacturonide-related signaling. *Phytochemistry* 57, 929-967 (2001).
11. Kravtchenko, T.P., Arnould, I., Voragen, A.G.J. & Pilnik, W. Improvement of the selective depolymerization of pectic substances by chemical  $\beta$ -elimination in aqueous solution. *Carbohydrate Polymers* 19, 237-242 (1992).

12. Renard, C.M.G.C. & Thibault, J.-F. Degradation of pectins in alkaline condition: kinetics of demethylation. *Carbohydr Res* 286, 139-150 (1996).
13. Inohara, H. & Raz, A. Effects of natural complex carbohydrate (citrus pectin) on murine melanoma cell properties related to galectin-3 functions. *Glycoconj J* 11, 527-532 (1994).
14. Camby, I., Le Mercier, M., Lefranc, F. & Kiss, R. Galectin-1: a small protein with major functions. *Glycobiology* 16, 137R-157R (2006).
15. Hirabayashi, J., et al. Oligosaccharide specificity of galectins: a search by frontal affinity chromatography. *Biochim Biophys Acta* 1572, 232-254 (2002).
16. Hennessy, B.T., Smith, D.L., Ram, P.T., Lu, Y. & Mills, G.B. Exploiting the PI3K/AKT pathway for cancer drug discovery. *Nat Rev Drug Discov* 4, 988-1004 (2005).
17. Yin, Y. & Shen, W.H. PTEN: a new guardian of the genome. *Oncogene* 27, 5443-5453 (2008).
18. Gunning, A.P., Bongaerts, R.J. & Morris, V.J. Recognition of galactan components of pectin by galectin-3. *Faseb J* (2008).
19. Singer, C.F., Kostler, W.J. & Hudelist, G. Predicting the efficacy of trastuzumab-based therapy in breast cancer: Current standards and future strategies. *Biochim Biophys Acta* (2008).
20. Fishman, M.L., Chau, H.K., Hoagland, P. & Ayyad, K. Characterization of pectin, flash-extracted from orange albedo by microwave heating, under pressure. *Carbohydr Res* 323, 126-138 (2000).
21. Garna, H., Mabon, N., Wathelet, B. & Paquot, M. New method for a two-step hydrolysis and chromatographic analysis of pectin neutral sugar chains. *J Agric Food Chem* 52, 4652-4659 (2004).
22. Fraysse, N., Verollet, C., Couderc, F. & Poinso, V. Capillary electrophoresis as a simple and sensitive method to study polysaccharides of *Sinorhizobium* sp. NGR234. *Electrophoresis* 24, 3364-3370 (2003).

23. Bedouet, L., Courtois, B. & Courtois, J. Rapid quantification of O-acetyl and O-methyl residues in pectin extracts. *Carbohydr Res* 338, 379-383 (2003).
24. Rosenbohm, C., Lundt, I., Christensen, T.I. & Young, N.G. Chemically methylated and reduced pectins: preparation, characterisation by <sup>1</sup>H NMR spectroscopy, enzymatic degradation, and gelling properties. *Carbohydr Res* 338, 637-649 (2003).
25. Albini, A., et al. A rapid in vitro assay for quantitating the invasive potential of tumor cells. *Cancer Res* 47, 3239-3245 (1987).
26. Irish, J.M., et al. Single cell profiling of potentiated phospho-protein networks in cancer cells. *Cell* 118, 217-228 (2004).
27. Krutzik, P.O. & Nolan, G.P. Fluorescent cell barcoding in flow cytometry allows high-throughput drug screening and signaling profiling. *Nat Methods* 3, 361-368 (2006).



### **3. Conclusions and Future Directions**

#### **3.1. Conclusions**

The specific objectives of this thesis were as follows:

1. To exploit the pathophysiology of solid tumors and enhance combination chemotherapy regimens by engineering novel nanoscale delivery vehicles termed 'nanocells.' (Chapter 2.1 and 2.2)
  - a. To assess the therapeutic benefit of this delivery platform.
  - b. To demonstrate that any increased therapeutic benefit is due to both the controlled spatial and temporal release of the encapsulated agents, as indicated by the tumor pathophysiology.
2. To develop new tools and strategies for optimizing nanocell formulations. (Chapter 2.3 and 2.4)
  - a. To develop a new computational model for drug release from nanoscale delivery systems. A better understanding of nanoscale drug release will facilitate the future optimization of nanocell spatio-temporal release profiles.
  - b. To generate and characterize a new set of carbohydrate-based anti-tumor agents with low systemic toxicity. Anti-tumor carbohydrates may be used in nanocells as reduced toxicity alternatives to traditional chemotherapeutic agents.

Objective 1 was met in chapter 2.1 and 2.2. Chapter 2.1 reported the disease-driven engineering of a drug delivery system, a 'nanocell', which overcomes these barriers unique to solid tumors. The nanocell comprises a nuclear nanoparticle within an extranuclear pegylated-lipid envelope, and is preferentially taken up by the tumor. Several components of the nanocell approach can facilitate future therapy in humans. First, the nuclear arrangement of cytotoxic

agent-conjugated nanoparticle and the encapsulation of the anti-angiogenesis agent in the surrounding phospholipid block-copolymer envelope enables temporal targeting of the tumor vasculature, resulting in the intra-tumoral trapping of the nanoparticles. Second, the resultant slow release and focal build-up of the cytotoxic agent within the tumor allows a prolonged exposure and an increase in the apoptotic potential, which can overcome hypoxia-induced reactive resistance. Third, although we show here a selective tumor uptake, we recognize that these vehicles can be further specifically targeted to tumor vasculature by using probes that recognize specific molecular signatures on the vasculature. Thus, the nanocell concept enables a significant advance in cancer therapy over current approaches. This platform technology supports the paradigm shift from a 'reductive' to an 'integrative' approach in cancer therapy. Chapter 2.2 extended the application of nanoscale delivery systems and reported the first study demonstrating the use of sterically stabilized lipid-encapsulated fluorescent quantum dots for distinguishing normal and neoplastic vasculature. The delineation between the spatial distribution of these formulations between tumor and normal vasculature creates the opportunity to harness this approach in detection of solid tumors.

Objective 2 was met in Chapter 2.3 and 2.4. Chapter 2.3 reported a new computational model for drug release from nanoscale delivery vehicles. Because all processes that influence drug release are not yet quantitatively understood, there is value to the use of semi-empirical computational models able to simulate multi-phase drug release profiles. Use of the model presented here does not require knowledge of physical parameters such as polymer porosity, drug solubility, and drug diffusivity which are often not available or can be difficult to measure. Voxelation of the entire nanoparticle facilitates the extension of this platform to non-symmetrical vehicle formulations as well as non-uniform drug and polymer distributions. Variation of the

parameter  $\kappa$  demonstrates the versatility of this model for simulating release of hydrophilic, hydrophobic, and polymer-conjugated drugs. This model was intended as a proof of principle, however in the future emerging mechanistic understandings of phenomenon influencing nanoparticle drug release may be incorporated to further increase accuracy and strengthen predictive power. Chapter 2.4 reported the generation and characterization of new anti-tumor pectin epitopes. We provided an integrative approach to link pectin structure with anti-tumor efficacy and intracellular mechanism of action. We demonstrated the first structure-function link that Gal-1 and Gal-3 binding promotes an anti-tumor intracellular signaling cascade mediated by the dephosphorylation of AKT. The identification of PTEN as an essential mediator of ACP's effect on this pathway has direct implications for the potential translation of pectin as a clinical therapy. The reduced toxicity and polymeric nature of ACP make it a good alternative to traditional chemotherapeutic agents in future nanocell formulations.

### **3.2. Future Directions**

The spatio-temporal delivery platform of the nanocell and the techniques for the development and analysis of carbohydrate-based chemotherapeutic agents have ready extension to a number of therapeutic applications. We conclude by discussing two that are currently under exploration as future directions of this work.

#### **3.2.1. Extending the nanocell platform**

Solid tumors are suitable targets for nanocell therapy due to their pathophysiology as discussed in detail in this work. In the future, the nanocell delivery strategy could also be applied to any disease with an angiogenic or multi-compartmental basis. For proof of principle,

we present asthma as a model pathology for future nanocell treatment strategies. The National Heart, Lung, and Blood Institute includes the following features as integral to the definition of asthma: recurrent episodes of respiratory symptoms, variable airflow obstruction that may be reversible, airway hyperreactivity, and chronic airway inflammation<sup>1</sup>. Asthma is well suited for treatment by a nanocell-like therapy due to the multicompartamental nature of this disease, especially as these components act on significantly different time scales.

Asthma occurs after initial sensitization to inhaled antigens which stimulate induction of Th2-type T cells which release cytokines including IL-4 and IL-52. These released cytokines stimulate B cells to produce IgE, mast cells to grow, and eosinophils to grow and activate. The IgE-mediated reaction to these inhaled allergens results in an acute and late-phase response. During the acute response, crosslinking of IgE on the mucosal surface results in the release of chemical mediators which open the mucosal tight-junctions and enhance penetration of antigen. Further, direct stimulation of subepithelial vagal receptors provokes bronchoconstriction through central and local reflexes. This acute or immediate phase response occurs within minutes of stimulation and consists of bronchoconstriction, edema, mucus secretion, and potentially hypotension.

The same mediators involved in the acute phase response also recruit other leukocytes including neutrophils and monocytes, lymphocytes, basophils, and eosinophils. The major basic protein of eosinophils in turn causes epithelial damage and airway constriction. This late phase response starts 4 to 8 hours after stimulation and may persist for 12 to 24 hours or more. In fact, inflammatory cells chronically present in asthmatics may release further mediators which enhance the severity of the late phase response. Long-term inflammatory remodeling and fibrosis remains one of the most severe symptoms of chronic asthmatics.

Currently the acute and long-term phases are treated with B2 agonists and corticosteroids respectively, however controversy still surrounds the proper use of both. Prior to the recognition of asthma as an inflammatory disease, B2 agonists were often the sole therapy for asthmatics. Recent reports have however raised concern regarding mortality and desensitization with this treatment<sup>3</sup>. There is conflicting evidence, however, whether excessive or regular use of  $\beta$ -adrenergic bronchodilators can actually worsen asthma, perhaps contributing to morbidity and mortality<sup>4,5</sup>. Corticosteroids have now become the first line defense in almost all patients with persistent asthma, though there is continued debate regarding the dosing regimens of inhaled steroids. Several studies with long term follow-up indicate that corticosteroids do not cure asthma, and cessation of therapy often results in swift relapse. Some studies suggest that in stable asthmatics less-frequent dosing may be equally effective<sup>6</sup>. Data also supports the often recommended combination therapy of corticosteroids and long-acting B2 agonists. These patients still require a separate short acting B2 agonist for acute asthmatic attacks. Currently treatment for asthma is directed by a series of expert practice guidelines and widespread dissemination. However, the Cleveland Clinic points out that most of these guidelines are not truly evidence based and represent an expert opinion. As asthma research is a rapidly evolving area and new therapeutics are anticipated, these guidelines are expected to be revised periodically. The hope is that as controlled studies become available, expert dogma will be replaced by data<sup>6</sup>.

Towards this goal, we are exploring a pathophysiology-driven approach to asthma therapy. This therapy would utilize a nanocell-like delivery vehicle capable of delivering a short acting B2 agonist quickly to a patient in acute distress with the subsequent sustained release of a corticosteroid. This nanocell formulation would have the benefits of less frequent dosing and

better patient compliance. Less frequent dosing would decrease the likelihood of steroid desensitization, and patient compliance is an issue in asthma therapy due to “steroid phobia.” The sustained release platform would allow smaller corticosteroid drug concentrations, and the delivery of this agent directly after B2 agonist action may allow greater penetration within the lung tissue. The cost of production of this dual-release vehicle may also be balanced by the reduced cost of smaller drug amounts.

### **3.2.2. Extending structure-function analysis of carbohydrate-based therapies**

We have developed in this study tools and strategies for the elucidation of complex structure-function relationships for pectin-based chemotherapeutics. These techniques are readily extendable to other complex carbohydrate-based chemotherapeutic agents which would greatly benefit from similar analysis. We present heparan sulfate glycosaminoglycans (HSGAGs) as a model system for future exploration. HSGAGs are linear polysaccharides with a great deal of structural complexity found both on the cell surface and within the extracellular matrix (ECM). Recent progress in understanding the biosynthetic regulation of these molecules combined with powerful new tools for their structural and functional characterization has led to a virtual explosion in the number of biological processes in which HSGAGs have been implicated. Some major processes in which HSGAGs appear to play a key regulatory role include development<sup>7</sup>, growth factor signaling<sup>8</sup>, viral and bacterial invasion<sup>9</sup>, wound healing<sup>10</sup>, and tumor progression<sup>11</sup>.

Exploration into the structure/function relationship of HSGAGs for modulating biological processes has long been hindered by difficulties in their structural characterization and sequencing. The basic disaccharide repeat of the HSGAG polysaccharide chain consists of a

hexuronic acid linked 1,4 to a hexosamine with four potential sites of chemical modification. Together the four different modifications combined with the potential for either the iduronic or glucuronic acid isomer give rise to 32 different plausible disaccharide units<sup>12</sup>. This can be contrasted with the 20 amino acids for proteins and the 4 bases for DNA. In a single octasaccharide, there are theoretically more than a million potential structures. Also, unlike the biosynthesis of DNA and protein, the biosynthesis of glycosaminoglycans is not template-based, and so the sequencing and amplification of HSGAGs is not amenable to the same technologies used with these biopolymers.

The information rich carbohydrate backbone of heparan sulfate consists of alternating hexuronic acid (D-glucuronic acid (GlcA) or L-iduronic acid (IdoA)) linked 1,4 to D-glucosamine (GlcN) units. These polysaccharides are attached to their core protein via tetrasaccharide linkage regions consisting of –GlcA-Gal-Gal-Xyl-Ser residues(for review see13). After the initial formation of this tetrasaccharide, the alternating addition of GlcA and GlcNAc from their UDP-sugar nucleotide precursors forms a repeating 1,4-linked disaccharide chain. The disaccharide chain is further modified either concomitantly or independently and sequentially by a series of sulfotransferases<sup>11</sup>, of which N-deacetylase-N-sulfotransferase (NDST), the 2-O (HS2ST), 3-O (HS3ST), and 6-O (HS6ST) heparan sulfate sulfotransferases are key players (Figure 1-1). Several tissue and substrate specific isoforms of each of these sulfotransferases have been discovered, signifying a further level of complexity in the biosynthesis of heparan sulfate(for review see<sup>14</sup>).

One recent study from our laboratory has demonstrated an effective methodology for sequencing heparin oligosaccharides utilizing a combined capillary electrophoresis-mass spectrometry approach<sup>12</sup>. In this study, exhaustive digestion of heparin oligosaccharides with

heparinases decomposes heparin into its disaccharide building blocks which are then amenable to analysis by capillary electrophoresis (CE). Matrix assisted laser desorption/ionization mass spectrometry (MALDI-MS) further supplies information on the molecular mass and possible combinations of the disaccharide units. Partial digestion using the different substrate specificities of heparinase I, II, and III, with subsequent MALDI-MS analysis gives further structural information that may be used in a stepwise fashion to determine the overall oligosaccharide sequence.

The ability to isolate and characterize HSGAG fragments combined with our now extensive understanding of the biosynthesis of HSGAGs has for the first time provided the tools to begin to elucidate the mechanisms of HSGAG regulation in important biological processes and pathologies. Recent developments in HSGAG regulation of cancer progression provide an urgent application for these technologies.

Many of the events associated with tumor growth and metastasis are directly influenced by interactions between malignant cells and their ECM. Due to the key regulatory roles of HSGAGs in processes that occur at the cell surface-ECM interface, it is not surprising that a large body of evidence has been found implicating HSGAG involvement at almost all levels of cancer development and progression (for recent reviews<sup>11, 15, 16</sup>). A recent study from our lab has for the first time, however, demonstrated a direct link between the composition of a tumor's cell surface HSGAG coat and its potential for malignancy<sup>17</sup>. This study made use of the heparan sulfate cleaving enzymes heparinase I and heparinase III, which have distinct and opposing heparan sulfate substrate specificities, as tools for analyzing tumor cells with different cell surface compositions of HSGAGs. It was discovered that tumor cells treated with heparinase III (with cleavage at undersulfated HS regions) showed significantly less ability to colonize to lungs



than cells treated with heparinase I (with cleavage at highly sulfated HS regions) or control cells. Further, fragments from tumor cells exposed to heparinase III inhibited the growth of primary tumor in vivo, while fragments from tumor cells exposed to heparinase I had the opposite effect. While this study links HSGAG sulfation with tumor progression, it is not clear how tumor cells biosynthetically regulate their HSGAG sulfation in vivo, or what heparan sulfate differential sulfation patterning is most relevant in tumor progression.

The contribution of HSGAG biosynthetic enzymes to tumorigenesis has already been demonstrated with the discovery of the tumor suppressor genes EXT1 and EXT218. These genes have been implicated in the formation of chondrosarcomas and other sporadic cancers, and encode the enzyme GlcA/GlcNAc transferase which is required for heparan sulfate chain elongation and synthesis<sup>19</sup>. The contribution of other enzymes involved in HSGAG biosynthesis to tumor progression has not yet been elucidated. We propose here an approach to further elucidate the role of HSGAG differential sulfation in tumor development by altering the expression of three biosynthetic sulfotransferases, HS2ST, HS6ST, and HS3ST, via the use of mRNA and siRNA knockdown constructs.

Modulation of a target gene's activity may be accomplished both at the DNA and mRNA levels. The most commonly used DNA-level approach for gene targeting is gene knockout by homologous recombination. Homologous recombination involves the "knock-out" of a gene through physical disruption of the targeted gene resulting from crossover events occurring during cell division between the targeting vector and the selected gene.<sup>20</sup> While effective, this technique is hampered by its inefficiency, expense, and limited use in animal models for embryonic lethal knockouts. Other gene-level disruption techniques include the use of synthetic oligodeoxynucleotides (ODNs) capable of hybridizing double-stranded DNA

forming a triple-stranded helix and preventing subsequent transcription events<sup>21</sup>, as well as the use of specific nucleic acid sequences to act as decoys for transcription factors<sup>22</sup>. The former is limited by access to DNA compacted within the chromosome structure, and the latter by the lack of single-gene transcription factors.

mRNA-level gene silencing approaches involve the destabilization of target mRNA, thereby preventing synthesis of the target protein. While anti-gene targeting approaches are in theory more advantageous from a stoichiometric point of view, mRNA itself is more accessible and mRNA disruption allows for greater control over the degree of gene disruption, as well as for temporal regulation. A recently developed method for mRNA disruption involves the use of RNA interference (RNAi) or post-transcriptional gene silencing<sup>23</sup>. RNAi involves the use of double-stranded RNA transcripts which lead to diminished levels of complementary endogenous mRNA after introduction into the cell. RNAi has been well demonstrated in *C. elegans* and *Drosophila*, and there is currently a great deal of study into understanding the mechanism of action and achieving a similar effect in mammalian systems<sup>24,25</sup>.

A well established technique for regulating gene expression at the mRNA level is the use of antisense RNA or DNA. Antisense RNA involves the introduction of vector-generated mRNA complementary to regions of the target mRNA strand. These complementary mRNA strands form a double helix within the cell resulting in disruption of subsequent translation. Naturally occurring antisense RNA in higher eukaryotes has been well documented (for review see<sup>26</sup>). Antisense transcripts are usually transcribed from the same locus as the sense RNA, but in the opposite direction with overlap over the region of sense transcription. Studies of bFGF during embryogenesis have demonstrated a reciprocal relationship between sense and antisense

transcripts<sup>27</sup>, and the natural expression of an antisense transcript to eIF-2 $\alpha$  in peripheral blood T cells is thought to play a role in regulating gene expression<sup>28</sup>.

The mechanism of antisense inhibition is not well understood in the case of both naturally occurring and artificially introduced antisense mRNA, and it appears to be different for each case involved. In general, antisense mRNA is thought to block gene expression by hybridizing to the target mRNA resulting in the formation of a double helix. This process may occur at any point after transcription and before the initiation of translation. Therefore possible mechanisms range from disruption of post-transcriptional splicing, inhibition of nuclear transport, destabilization of the transcript, and disruption of translation (for review see<sup>29</sup>). As such, difficulties arise in rationally designing synthetic antisense mRNA to achieve a significant gene knockdown. We propose to design antisense mRNA to regions of the target sulfotransferase mRNA with the goal of obtaining multiple levels of gene knockdown. The 5'UTR and two regions of the 3' UTR could be targeted as these segments have long been naturally implicated for playing a significant role in translation initiation and termination, transcript stability, and nuclear transport. mRNA knockdown of specific sulfotransferase enzyme transcripts would result in tumor HSGAGs with controlled sulfation profiles suitable for assessing relationships between fine structure and tumorigenicity using the tools and techniques developed in this work for pectin-based therapies. HSGAGs, like pectin, represent a potential source for natural, readily available, cost-effective, and low toxicity carbohydrate-based chemotherapeutic alternatives.

### 3.3. References

1. Guidelines for the diagnosis and management of asthma. National Heart, Lung, and Blood Institute. National Asthma Education Program. Expert Panel Report. *J Allergy Clin Immunol* 88, 425-534 (1991).

2. Cotran, R. S. e. a. Robbins Pathologic Basis of Disease (1999).
3. Larj, M. J. & Bleecker, E. R. Effects of beta2-agonists on airway tone and bronchial responsiveness. *J Allergy Clin Immunol* 110, S304-12 (2002).
4. Silverman, E. K. et al. Family-based association analysis of beta2-adrenergic receptor polymorphisms in the childhood asthma management program. *J Allergy Clin Immunol* 112, 870-6 (2003).
5. McGraw, D. W., Almoosa, K. F., Paul, R. J., Kobilka, B. K. & Liggett, S. B. Antithetic regulation by beta-adrenergic receptors of Gq receptor signaling via phospholipase C underlies the airway beta-agonist paradox. *J Clin Invest* 112, 619-26 (2003).
6. Kavuru M.S., L. D. M., Erzurum S.C. (Cleveland Clinic Foundation, 2005).
7. Perrimon, N. & Bernfield, M. Specificities of heparan sulphate proteoglycans in developmental processes. *Nature* 404, 725-8. (2000).
8. Herr, A. B., Ornitz, D. M., Sasisekharan, R., Venkataraman, G. & Waksman, G. Heparin-induced self-association of fibroblast growth factor-2. Evidence for two oligomerization processes. *J Biol Chem* 272, 16382-9. (1997).
9. Shukla, D. et al. A novel role for 3-O-sulfated heparan sulfate in herpes simplex virus 1 entry. *Cell* 99, 13-22. (1999).
10. Petitou, M. et al. Synthesis of thrombin-inhibiting heparin mimetics without side effects. *Nature* 398, 417-22. (1999).
11. Sengupta, S. et al. Temporal targeting of tumour cells and neovasculature with a nanoscale delivery system. *Nature* 436, 568-72 (2005).
12. Venkataraman, G., Shriver, Z., Raman, R. & Sasisekharan, R. Sequencing complex polysaccharides. *Science* 286, 537-42. (1999).
13. Lindahl, U., Kusche-Gullberg, M. & Kjellen, L. Regulated diversity of heparan sulfate. *J Biol Chem* 273, 24979-82. (1998).
14. Habuchi, O. Diversity and functions of glycosaminoglycan sulfotransferases. *Biochim Biophys Acta* 1474, 115-27. (2000).
15. Blackhall, F. H., Merry, C. L., Davies, E. J. & Jayson, G. C. Heparan sulfate proteoglycans and cancer. *Br J Cancer* 85, 1094-8. (2001).

16. Liu, D., Shriver, Z., Qi, Y., Venkataraman, G. & Sasisekharan, R. Dynamic regulation of tumor growth and metastasis by heparan sulfate glycosaminoglycans. *Semin Thromb Hemost* 28, 67-78. (2002).
17. Liu, D., Shriver, Z., Venkataraman, G., El Shabrawi, Y. & Sasisekharan, R. Tumor cell surface heparan sulfate as cryptic promoters or inhibitors of tumor growth and metastasis. *Proc Natl Acad Sci U S A* 99, 568-73. (2002).
18. McCormick, C. et al. The putative tumour suppressor EXT1 alters the expression of cell-surface heparan sulfate. *Nat Genet* 19, 158-61. (1998).
19. Lind, T., Tufaro, F., McCormick, C., Lindahl, U. & Lidholt, K. The putative tumor suppressors EXT1 and EXT2 are glycosyltransferases required for the biosynthesis of heparan sulfate. *J Biol Chem* 273, 26265-8. (1998).
20. Bronson, S. K. & Smithies, O. Altering mice by homologous recombination using embryonic stem cells. *J Biol Chem* 269, 27155-8. (1994).
21. Maher, L. J., 3rd. Prospects for the therapeutic use of antigene oligonucleotides. *Cancer Invest* 14, 66-82 (1996).
22. Sharma, H. W., Perez, J. R., Higgins-Sochaski, K., Hsiao, R. & Narayanan, R. Transcription factor decoy approach to decipher the role of NF-kappa B in oncogenesis. *Anticancer Res* 16, 61-9. (1996).
23. Sharp, P. A. RNAi and double-strand RNA. *Genes Dev* 13, 139-41. (1999).
24. Sharp, P. A. RNA interference--2001. *Genes Dev* 15, 485-90. (2001).
25. Sharp, P. A. & Zamore, P. D. Molecular biology. RNA interference. *Science* 287, 2431-3. (2000).
26. Jackson, C. L. et al. Pectin induces apoptosis in human prostate cancer cells: correlation of apoptotic function with pectin structure. *Glycobiology* 17, 805-19 (2007).
27. Zuniga Mejia Borja, A., Meijers, C. & Zeller, R. Expression of alternatively spliced bFGF first coding exons and antisense mRNAs during chicken embryogenesis. *Dev Biol* 157, 110-8. (1993).
28. Noguchi, M., Miyamoto, S., Silverman, T. A. & Safer, B. Characterization of an antisense Inr element in the eIF-2 alpha gene. *J Biol Chem* 269, 29161-7. (1994).
29. Jen, K. Y. & Gewirtz, A. M. Suppression of gene expression by targeted disruption of messenger RNA: available options and current strategies. *Stem Cells* 18, 307-19 (2000).

## List of Figures and Tables

### Chapter 2.1 Spatio-Temporal Targeting of Tumor Cells and Neovasculature: The Nanocell

|  |    |
|--|----|
| <b>Figure 1.</b> Diagram of nanocell therapy.....  | 35 |
| <b>Figure 2.</b> Synthesis and characterization of a combretastatin–doxorubicin nanocell.....                                      | 36 |
| <b>Figure 3.</b> Bioassay of the nanocell with a GFP-positive melanoma–endothelial cell three-dimensional co-culture system.....   | 38 |
| <b>Figure 4.</b> Nanocell therapy inhibits B16/F10 melanoma and Lewis lung carcinoma growth.....                                   | 40 |
| <b>Figure 5.</b> Effect of nanocell treatment on tumor vasculature and apoptosis.....  | 42 |
| <b>Supplementary Figure 1.</b> Effect of liposomal and nanocell combretastatin and long-term nanocell therapy on tumor growth..... | 45 |
| <b>Supplementary Figure 2.</b> Nanocell Biodistribution.....   | 46 |
| <b>Supplementary Figure 3.</b> Effect of nanocell therapy on metastasis of primary GFP+ melanoma to lungs and liver.....           | 47 |
| <b>Supplementary Figure 4.</b> Doxorubicin to PLGA 5050 conjugation schematic.....   | 48 |

### Chapter 2.2 Lipid-Encapsulated Quantum Dots Distinguish Tumor and Normal

#### Vasculature

|   |        |
|---|--------|
| <b>Figure 1.</b> Imaging of Angiogenic Vasculature..... | 65, 66 |
| <b>Figure 2.</b> 3-D Depth Coding.....                  | 67     |

## **Chapter 2.3 A voxel-based Monte Carlo Model of Drug Release From Bulk Eroding**

### **Nanoparticles**

|  |    |
|--|----|
| <b>Figure 1.</b> Geometric implications of pixel and voxel neighborhoods.....        | 75 |
| <b>Figure 2.</b> Flowchart and state diagram governing the voxel-based model.....    | 76 |
| <b>Figure 3.</b> Dexamethasone release from PLGA nanoparticles <i>in vitro</i> ..... | 77 |
| <b>Figure 4.</b> Simulation of drug release and nanoparticle fragmentation.....      | 78 |
| <b>Figure 5.</b> Influence of the model parameter $\kappa$ on drug release.....      | 79 |

## **Chapter 2.4 Structure-function Relationships of Novel Carbohydrate-Based Therapeutic**

### **Agents**

|   |    |
|---|----|
| <b>Figure 1.</b> Capillary electrophoresis and NMR analysis.....              | 92 |
| <b>Figure 2.</b> Anti-tumor efficacy <i>in vivo</i> and <i>in vitro</i> ..... | 94 |
| <b>Figure 3.</b> Pathway analysis of anti-tumor activity.....                 | 96 |

## List of Abbreviations

|       |  |
|-------|--|
| ACP   | Activated Citrus Pectin                              |
| APTS  | 8-aminopyrene-1,3,6-trisulfonic acid trisodium salt  |
| Ara   | Arabinose  |
| bFGF  | Basic Fibroblast Growth Factor                       |
| C     | Combretastatin A4                                    |
| CHOL  | Cholesterol  |
| D     | Doxorubicin  |
| dGalA | 4,5-Dehydro-galacturonic Acid                        |
| DSPC  | 1,2-Distearoyl-sn-Glycero-3-Phosphocholine           |
| DSPE  | 1,2-Distearoyl-sn-Glycero-3-Phosphatidylethanolamine |
| ECM   | Extracellular Matrix                                 |
| EPR   | Enhanced Permeability and Retention                  |
| FBS   | Fetal Bovine Serum                                   |
| Gal   | Galactose  |
| Gal-1 | Galectin-1   |
| Gal-3 | Galectin-3   |
| GalA  | Galacturonic Acid                                    |
| GFP   | Green Fluorescent Protein                            |
| Glc   | Glucose  |
| HGA   | Homogalacturonan                                     |



|       |  |
|-------|--|
| HGF   | Hepatocyte Growth Factor                   |
| HIF   | Hypoxia Inducible Factor                   |
| HPLC  | High Performance Liquid Chromatography     |
| HSGAG | Heparan Sulfate Glycosaminoglycans         |
| L     | Liposome                                   |
| Man   | Mannose                                    |
| MMP   | Matrix Metalloproteinase                   |
| NC    | Nanocell                                   |
| NCP   | Native Citrus Pectin                       |
| PBS   | Phosphate Buffered Saline                  |
| PDGF  | Platelet-Derived Endothelial Growth Factor |
| PEG   | Poly(ethylene glycol)                      |
| PLGA  | Poly(lactic-co-glycolic acid)              |
| QD    | Quantum Dot                                |
| RG-I  | Rhamnogalacturonan Type 1                  |
| RG-II | Rhamnogalacturonan Type 2                  |
| Rha   | Rhamnose                                   |
| VEGF  | Vascular Endothelial Growth Factor         |
| vWF   | von Willebrand Factor                      |
| WBC   | White Blood Cell                           |
| Xyl   | Xylose                                     |